

# **Ultrasonic Locating and Tracking of Small Particles for Biomedical Applications**

by

**Qiyang Chen**

Bachelor of Science in Physics, Nanjing University, China, 2015

Master of Science in Mechanical Engineering, George Washington University, USA, 2017

Submitted to the Graduate Faculty of the  
Swanson School of Engineering in partial fulfillment  
of the requirements for the degree of  
Doctor of Philosophy

University of Pittsburgh

2021

UNIVERSITY OF PITTSBURGH

SWANSON SCHOOL OF ENGINEERING

This dissertation was presented

by

**Qiyang Chen**

It was defended on

April 22, 2021

and approved by

Sung Kwon Cho, PhD, Professor, Department of Mechanical Engineering & Materials Science

George Stetten, PhD, MD, Professor, Department of Bioengineering

Alberto Vazquez, PhD, Associate Professor, Department of Bioengineering

Roderick J. Tan, MD, PhD, Assistant Professor, Department of Medicine

Dissertation Director: Kang Kim, PhD, Associate Professor, Department of Bioengineering and  
Department of Medicine

Copyright © by Qiyang Chen

2021

# **Ultrasonic Locating and Tracking of Small Particles for Biomedical Applications**

Qiyang Chen, Ph.D.

University of Pittsburgh, 2021

This dissertation focuses on the development of two novel ultrasound technologies with the idea of tracking and locating small particles: 1) Ultrasound tracking of the acoustically actuated microswimmers, 2) Super-resolution ultrasound (SRU) imaging by locating the microbubbles.

Artificial microswimmers that navigate in hard-to-reach spaces and microfluidic environments inside human bodies hold a great potential for various biomedical applications. For eventual translation of the microswimmer technology, a capability of tracking the microswimmers in 3-D through tissues is particularly required for reliable navigation. In this work, after first proposing and demonstrating the proof-of-concept of ultrasound tracking of the microswimmer in a 2-D setup in vitro, we built a 3-D ultrasound tracking system using two clinical ultrasound probes. A reliable performance for tracking the arbitrary 3-D motions of the newly designed 3-D microswimmers in real-time was demonstrated in vitro. The developed 3-D ultrasound tracking strategy could be a strong motivation and foundation for the future clinical translation of the novel microswimmer technology.

SRU that can identify microvessels with unprecedented spatial resolution is promising for diagnosing the diseases associated with abnormal microvascular changes. One of the potential applications is to assess the changes in renal microvasculature during the progressive kidney disease. In this work, we applied the developed deconvolution-based SRU imaging on the mouse acute kidney injury (AKI) model to show the capability of SRU for noninvasive assessment of renal microvasculature changes during the progression from AKI to chronic kidney disease (CKD).

The technology was then adapted to a clinical curved linear array probe and evaluated on both healthy human subjects and CKD patients. We also applied the SRU technology for identifying the vasa vasorum near rabbit femoral arteries that is a key biomarker for atherosclerosis plaque development. Overall, the study demonstrates a great potential of SRU as a diagnostic tool for these diseases and would promote the eventual clinical translations.

Future endeavors for integrating SRU locating technology with a reliable tracking capability of microparticles will provide a unique tool for various biomedical applications of the novel microdrones for diagnosis and drug delivery.

## Table of Contents

Preface .....	xix
<b>1.0 Introduction.....</b>	<b>1</b>
<b>1.1 Background and Motivations.....</b>	<b>1</b>
1.1.1 Ultrasound Tracking of the Acoustically Actuated Microswimmers .....	1
1.1.2 SRU Imaging .....	3
1.2 Objectives .....	5
1.3 Organization of Dissertation.....	6
<b>2.0 Two-dimensional Ultrasound Tracking of the Acoustically Actuated</b>	
<b>Microswimmers .....</b>	<b>8</b>
<b>2.1 Introduction.....</b>	<b>8</b>
2.1.1 Propulsion Mechanism of the Acoustically Actuated Microswimmer .....	8
2.1.2 Tracking of the Acoustically Actuate Microswimmer .....	11
2.2 Materials and Methods .....	12
2.2.1 Fabrication and Design of the Microswimmers .....	12
2.2.2 Experiment Setup.....	14
2.2.3 Tracking Algorithm for Camera and Ultrasound.....	17
2.3 Results and Discussion .....	18
2.4 Conclusions.....	24
<b>3.0 3-D ultrasound Tracking of the Acoustically Actuated Microswimmers .....</b>	<b>25</b>
<b>3.1 Introduction.....</b>	<b>25</b>
<b>3.2 Materials and Methods .....</b>	<b>26</b>

3.2.1 Design of the 3-D Microswimmer .....	26
3.2.2 3-D Ultrasound Tracking System .....	27
3.2.3 Control Algorithm.....	29
3.3 Results and Discussion .....	30
3.4 Conclusions.....	34
<b>4.0 SRU Imaging: In Vitro Validation of the Spatial Resolution .....</b>	<b>35</b>
4.1 Introduction.....	35
4.2 Materials and Methods .....	37
4.2.1 Design of the Microfluidic Chip.....	37
4.2.2 SRU Imaging Protocol .....	38
4.2.3 SRU Signal Processing Procedure .....	39
4.3 Results and Discussion .....	40
4.4 Conclusions.....	42
<b>5.0 SRU Imaging for Noninvasive Assessment of Renal Microvasculature Changes in</b>	
<b>Mouse AKI Model .....</b>	<b>43</b>
5.1 Introduction.....	43
5.2 Materials and Methods .....	46
5.2.1 Mouse Kidney Injury Model.....	46
5.2.2 Experiment Protocol .....	46
5.2.3 Histology and Immunohistochemistry .....	49
5.2.4 SRU Imaging Signal Processing Procedure.....	50
5.2.5 Rigid Body Motion Estimation and Compensation .....	52

5.2.6	SRU Image Analysis and Quantitative Assessment of the Microvasculature .....	55
5.2.7	Statistical Analysis.....	56
5.3	Results.....	56
5.3.1	IRI Leads to the Development of Renal Fibrosis .....	56
5.3.2	In Vivo SRU Imaging Enables a Qualitative Assessment of the Overall Changes of the Mouse Kidney with IRI .....	59
5.3.3	In Vivo SRU Imaging Enables a Quantitative Assessment of the Changes in Overall Morphology and Renal Perfusion of the Mouse Kidney with IRI .....	61
5.3.4	In Vivo SRU Imaging Correlates with Histology in Vessel Density Estimation .....	64
5.3.5	In Vivo SRU Imaging Enables a Quantitative Assessment of the Tortuosity Changes in the Cortical Vasculature.....	65
5.4	Discussion .....	67
5.5	Conclusions.....	71
6.0	SRU Imaging of Human Kidney Imaging Using Clinical Curved Linear Array Probe .....	73
6.1	Introduction.....	73
6.2	Material and Methods.....	74
6.2.1	Study Approval and Human Subject Recruitment .....	74
6.2.2	Imaging Protocol .....	74
6.2.3	Adaptation to Curved Linear Array .....	75
6.2.3.1	Imaging Sequence.....	75

6.2.3.2 Mechanical Index Limit for Safety .....	77
6.2.3.3 PSF Measurement and Coordinate Transform.....	77
6.2.4 Results.....	79
6.2.5 Discussion .....	82
6.2.6 Conclusions.....	84
<b>7.0 SRU Imaging of Vasa Vasorum in Rabbit Atherosclerotic Plaques.....</b>	<b>85</b>
7.1 Introduction.....	85
7.2 Material and Methods.....	87
7.2.1 Rabbit Atherosclerotic Plaque Model .....	87
7.2.2 SRU Imaging and Validation Protocol .....	88
7.2.3 SRU Signal Processing Procedure .....	89
7.3 Results and Discussion .....	90
7.4 Conclusions.....	96
<b>8.0 Conclusions and Future Directions.....</b>	<b>97</b>
<b>Bibliography .....</b>	<b>100</b>

**List of Tables**

**Table 1 Quantitative measurement of the sizes of the healthy and CKD kidneys.....82**

**Table 2 Quantitative measurement of the vessel densities of the healthy and CKD kidneys**  
**.....82**

## List of Figures

- Figure 1** Flow field of the designed one-channel microswimmer by particle tracking velocimetry measurement. (Reprinted with permission from ref. [33]. Copyright 2006 IOP Publishing Ltd) .....9
- Figure 2** Illustration of the parameters of the microtube in the microswimmer. (Reprinted with permission from ref. [33]. Copyright 2006 IOP Publishing Ltd).....10
- Figure 3** (a) Microswimmer design 1 with a single microtube (100  $\mu\text{m}$  in diameter and 760  $\mu\text{m}$  in length). (b) Microswimmer design 2 with center (860  $\mu\text{m}$  in length) and side (370  $\mu\text{m}$  in length) microtubes. (Courtesy of Dr. Sung Kwon Cho Lab).....14
- Figure 4** (a) Experiment schematic. The microswimmer in the water tank is activated by the acoustic actuator glued on the water tank with CW electrical signals transmitted by function generator 1 through the amplifier. Two ultrasound linear array probes (L7-4) and a high speed camera (Phantom v9.1) are utilized to record the movement of the microswimmer simultaneously. Probe 1 and Probe 2 are connected to two separate programmable ultrasound scanners (Verasonic V1 and Verasonic Vantage, respectively). The two ultrasound probes are immersed in water at 30 degrees to the water surface. Function generator 2 is utilized to transmit TTL signals to synchronize the Phantom v9.1 camera, Probe 1 and Probe 2. (b) Experimental setup picture. ...16
- Figure 5** Imaging field of view. The imaging field of view of each ultrasound probes is 7.11mm (elevation direction) X 36.2mm (lateral direction). The imaging field of view of the camera is 6.16 X 6.16mm with 656 X 656 pixels. The resulting imaging field of view overlaps at a 6.16 X 6.16mm area of interest.....17

**Figure 6 Superimposed time-lapse images from three different events of the microswimmers acquired by both camera and ultrasound probes. Figure. 6a, 6b, 6c are the superimposed time-lapse images for a straight type motion of the single-tube microswimmer acquired by camera, ultrasound probe 1 and probe 2 respectively. Figure. 6d, 6e, 6f show the microswimmer motion with a sharp turn. Figure. 6g, 6h, 6i show the circular movement of the second microswimmer by camera and two ultrasound probes. The yellow dashed rectangles in Figure. 6b, 6c, 6e, 6f, 6h, 6i denote to the camera images. ....20**

**Figure 7 Reconstructed trajectory and error analysis of ultrasound tracking for the three different events. Figure 7a, 7d, g show the 2-D reconstructed trajectory of the microswimmer from camera and ultrasound imaging. Figure 7b, 7e, 7h demonstrates the error (E) of ultrasound tracking compared to camera tracking (discrepancy between ultrasound and camera trajectory) at each frame. Figure 7b, 7e, 7h show the error (E) of ultrasound tracking normalized to moving distance ( $s = 0t(\Delta x)^2 + (\Delta y)^2$ ) at each frame. ....23**

**Figure 8 The design of 3-D microswimmer with the overall view (left) and the front view (right). (Courtesy of Dr. Sung Kwon Cho Lab).....27**

**Figure 9 (a) Schematic and (b) picture of the experimental set up. ....28**

**Figure 10 Two scenarios in the control algorithm. ....30**

**Figure 11 Superimposed time-lapse images of the microswimmers acquired by the camera and ultrasound probes.....31**

**Figure 12 (a) Reconstructed trajectories in y-z plane by camera and ultrasound. (b) Step-motor displacement in elevational direction. (c) Error (E) of ultrasound tracking**

compared to camera tracking (discrepancy between ultrasound and camera trajectory) at each frame. (d) Error (E) of ultrasound tracking normalized to moving distance ( $s = \sqrt{(\Delta x)^2 + (\Delta y)^2}$ ) at each frame. ....33

**Figure 13** An illustration of the concept of the SRU imaging technique. (Reprinted with permission from ref. [63]. Copyright 2015 Springer Nature) .....36

**Figure 14** Design of the microfluidic chip in top view(a) and longitudinal view (b). (c) Photo for the chip in top view. (d) Microscopy image of the microchannels around the bifurcation that marked in the dotted rectangle in (a).....38

**Figure 15** SRU signal processing pipeline. ....40

**Figure 16** (a) B-mode image of the microfluidic channels. (b) Reconstructed SRU image of the microfluidic channels.....40

**Figure 17** Axial signal magnitude profile averaged over 200  $\mu\text{m}$  along the channel in the area marked in white dotted box in Figure 16(b). ....41

**Figure 18** Experimental design for in vivo ultrasound super-resolution imaging on mouse acute kidney injury model. (a) Timeline of the experiment (b) Ischemia-reperfusion injury (IRI) is performed on the right kidney to induce the acute kidney injury (AKI). The sham, contralateral, and injured kidneys at 21-days and injured kidneys at 42-days post injury (n=5 for each group) were scanned by ultrasound in long axis for ultrasound super-resolution (USR) images. The kidneys were excised immediately after the scan for fibrosis analysis and immunohistochemistry with CD31 staining focusing on renal vasculature around the corticomedullary junction. (c) From the reconstructed USR images of the kidneys, kidney changes including area, vessel density, and microvasculature tortuosity were assessed. ....48

**Figure 19 SRU signal processing and image reconstruction procedure. (a) Signal processing block diagram. The raw radio frequency channel data was acquired by multi-angle ultrasound plane wave imaging and went through B-mode processing with delay-and-sum beamforming algorithm and quadrature demodulator. After estimating and compensating the rigid body motion of the kidney caused by respiration, a spatio-temporal eigen-based decomposition clutter filter was applied to suppress the signals from tissues and extract the signals from the microbubbles. RL deconvolution method was used to localize the center of each microbubble. Final SRU image was reconstructed by summing up 300 frames of the localized images. (b) Representative image of mouse kidney after B-mode processing. (c) Representative image after applying tissue suppressor. (d) Representative SRU image after microbubble center localization and frame summation. (e) Final image by overlaying the B-mode and SRU images of the mouse kidney. ....51**

**Figure 20 The schematic diagram of the motion artifacts due to respiration. ....53**

**Figure 21 Signal processing pipeline of the rigid body motion compensation. ....55**

**Figure 22 IRI leads to renal fibrosis. Mice were subjected to unilateral IRI and both the affected and contralateral kidneys were recovered at either 21 or 42 days after injury. (a) Fibrosis was detected with Masson’s Trichrome stain (blue staining) as well as picrosirius red stain (dark red). When the picrosirius slides were viewed under polarized light, birefringence denotes specific staining for collagens. (b) Fibrosis scoring of kidneys. (c-d) mRNA levels of collagen (Col3) are dramatically elevated in all injured kidneys compared to the contralateral kidneys. mRNA levels of VEGF are dramatically decreased in all injured kidneys. Data are expressed as mean  $\pm$  standard**

error. \*  $P < 0.0001$  compared to contralateral kidneys, no differences were found between the 21 and 42 day injured kidneys. ....59

**Figure 23** Overlaid B-mode and super-resolution ultrasound (B-SRU) images for sham kidneys, contralateral kidneys, injured kidneys at 21-days post injury, and injured kidneys at 42-days post injury. Column (a) shows the SRU images of the five sham kidneys. Column (b) shows the contralateral kidneys. Column (c) and column D show the SRU images of injured kidney scanned at 21 days and 42 days after injury, respectively. To provide an anatomical landmark, the major renal vessel branches, aorta, cortex, medulla, and dorsal skin were marked by white arrows in the image of the injured kidney from the mouse number 6. Overall decrease in size and increase in vasculature rarefaction were observed over time. ....61

**Figure 24** Quantitative assessment of the changes in overall morphology and renal blood volume of sham, contralateral, and IRI kidneys. (a) Kidney cross-sectional area measured from the long-axis US B-mode images. Cross-sectional areas of the sham, contralateral, 21 days post injury and 42 days post injury kidneys were  $49.20 \pm 1.58 \text{ mm}^2$ ,  $51.61 \pm 3.57 \text{ mm}^2$ ,  $37.54 \pm 1.55 \text{ mm}^2$ ,  $35.67 \pm 2.414 \text{ mm}^2$ . A significant decrease in kidney area after IRI was observed by ultrasound measurement. (b) Weight of the sham ( $160.50 \pm 4.83 \text{ g}$ ), contralateral ( $197.70 \pm 8.08 \text{ g}$ ), and injured kidneys (21 days:  $96.94 \pm 6.22 \text{ g}$ , 42days:  $80.70 \pm 6.14 \text{ g}$ ). Significant reduction in weight was found, which supports the size decrease measured by US. (c) Cortex thickness of the kidneys measured from the US images. Significant decrease of the cortex thickness of the injured kidneys (21days:  $1.23 \pm 0.04 \text{ mm}$ , 42 days:  $1.10 \pm 0.08 \text{ mm}$ ) compared to sham ( $1.76 \pm 0.03 \text{ mm}$ ) and contralateral ( $1.88 \pm 0.08 \text{ mm}$ ) was found. (d) US estimation of

relative blood volume (rBV). The average rBV of the sham kidneys, contralateral kidneys, and IRI kidneys at 21 days and 42 days were  $34.66\% \pm 1.99\%$ ,  $35.85\% \pm 1.88\%$ ,  $22.35\% \pm 1.38\%$ , and  $26.30\% \pm 1.92\%$ , respectively. Significant decrease of rBV on IRI kidney was observed. (e) Vessel density in the cortex measured by US. A significant reduction in 21 days ( $39.77 \pm 2.69\%$ ) and 42 days ( $46.47 \pm 2.47\%$ ) post-injury kidneys compared to sham ( $64.44 \pm 1.80\%$ ) and contralateral ( $66.96 \pm 2.66\%$ ) kidneys was found. (f) Vessel density in the corticomedullary junction measured by US. A significant decrease in 21 days ( $26.17 \pm 1.28\%$ ) and 42 days ( $27.60 \pm 1.37\%$ ) compared to sham ( $47.14 \pm 2.41\%$ ) and contralateral ( $49.59 \pm 2.42\%$ ) was found. (n=5, ANOVA with post-hoc Tukey HSD test, \*P<0.05; \*\*P<0.01; \*\*\*P<0.001.).....63

**Figure 25 Vessel density in the corticomedullary junction by histology and correlation with US imaging. (a) Representative CD31 staining of the sham, contralateral, and IRI kidneys. (b) Vessel density measured as positively stained area fraction of the vessels in corticomedullary junction. (Sham:  $12.14 \pm 0.75\%$ , contralateral:  $15.02 \pm 0.47\%$ , 21 days:  $7.56 \pm 0.22\%$ , 42 days:  $8.82 \pm 0.73\%$ ) Injured kidneys exhibited a decrease of vessel density in the ROI compared either sham or contralateral kidney. (n=5, ANOVA with post-hoc Tukey HSD test, \*P<0.05; \*\*P<0.01; \*\*\*P<0.001.) (c) Significant correlation between the histology and SRU measurement of the vessel density in the corticomedullary junction was found (P value < 0.001, correlation coefficient: 0.77). (n=20, Pearson's correlation analysis) .....65**

**Figure 26 Tortuosity of the control kidney and IRI kidney. (a) Representative SRU images of the cortical vessels from control and 42-days post-injury kidneys are shown. White arrows indicate the curved and clamped vessels from 42-days post-injury kidney. (b)**

Significant increase of cortical microvasculature tortuosity is shown in the kidney at 42-days post injury. (n=5, ANOVA with post-hoc Tukey HSD test, \*P<0.05.) .....66

Figure 27 UI of the custom-designed sequence for human kidney imaging.....76

Figure 28 SRU signal processing pipeline for human kidney imaging with representative images for each step.....78

Figure 29 (a) B-mode image of the human kidney. (b) Overlaid SRU and B-mode images of the kidney. (c) Zoomed in SRU image of the ROI indicated by white dashed rectangle in (b), with detectable smallest vessel marked by white arrow. (d) Spatial profile of the selected vessel. FWHM is estimated at 0.14 mm ( $<\lambda/3$ ).....80

Figure 30 Overlaid B-SRU images of the kidneys from the total of two healthy human subjects and five CKD patients. ....81

Figure 31 (a) Study timeline. (b) Signal processing procedure of SRU imaging.....88

Figure 32 B-mode, SRU overlaid on B-mode images, H&E, and CD31 stain of the contralateral uninjured side (A) and injured side (B) of the femoral arteries from rabbit #1. Two image slices separated by ~ 0.5mm were taken by ultrasound on each side. Column 1 and 2 depict the B-mode and SRU images of area that were suspected for plaque and VV development. The white dotted lines represent vessel wall and white arrows indicate VV. Significant plaque development was evidenced in the injured side (B5) and verified by H&E stain (column 3). A significantly increased VV population in the adventitia area and VV infiltrated into the plaque were identified from SRU images (column 2) and validated by CD31 stain (column 4, 5). ....91

Figure 33 B-mode, SRU overlaid on B-mode, and  $\mu$ CT images of the uninjured side (A) and injured side (B) of the femoral arteries from rabbit #2. Column 3 shows the 3D  $\mu$ CT

images of the harvested arteries. Column 4 displays ROI marked in yellow box in column 3, with higher magnification at 0° and 270° view. Increase of VV population was observed in injured side compared to uninjured side by SRU, and evidenced by corresponding  $\mu$ CT images. ....93

Figure 34 (a) Full view of femoral artery in the imaging plane of B4 in Figure 33. White dashed rectangle marks the area where excessive VV development around the plaque is identified. (b) Zoomed-in SRU image of the area. (c) The matching  $\mu$ CT image of the same area. ....94

## **Preface**

Thank to my advisor Dr. Kang Kim,

All the committee members,

All my colleagues and friends,

And my family.

## **1.0 Introduction**

This work focuses on the two topics with the idea of tracking and locating small particles:  
1) Ultrasound tracking of the acoustically actuated microswimmers, 2) Super-resolution ultrasound (SRU) imaging by locating the microbubbles. Novel ultrasound signal and image processing algorithms have been developed and applied to locate and track small particles for biomedical applications.

In this section, the motivations and the specific objectives of the studies will be summarized. The overview of the organization of this dissertation will also be presented.

### **1.1 Background and Motivations**

#### **1.1.1 Ultrasound Tracking of the Acoustically Actuated Microswimmers**

Artificial microswimmers that navigate in hard-to-reach spaces and microfluidic environments inside human bodies have drawn increasing research interest over the past decades [1]–[4]. The microswimmers hold a great potential in various biomedical applications, including targeted drug delivery [5]–[8], microsurgery [8]–[11], particle separation and assembly [12]–[14], bio-sensing [8], and further promote a revolution in medicine in the future [4], [15], [16]. Whereas there has been continued progress in designing and fabricating novel microswimmers for different applications, the major challenges still remain especially when considering practical propulsion, tracking, and control of the microswimmers in real biomedical environments [4], [17].

Concerning the propulsion of the microswimmers, a variety of approaches have been investigated, such as harness of biological [18], [19], chemical fuels [20]–[24], magnetic actuation [25]–[29]. However, they all have some limitations in practical applications. Harness of biological requires controlled environment for the bacteria to survive, which is challenging for in vivo applications. Chemical fuels are commonly not biocompatible and may do harm to the human body. Magnetic actuation attracted more interest among these mechanisms. However, the actuation in general requires a set of several bulky external coils to generate a strong magnetic field and the magnetic field is not compatible with some implanted devices. Acoustic actuation is promising and appealing in real biomedical environments, since it is noninvasive and biocompatible [30]–[32]. Acoustic waves can travel through biological tissues to perform wireless actuations on microswimmers. Moreover, it would be a convenient and economic approach if translating into clinical practice. The microswimmers with air-filled cavity that are propelled by acoustic actuation have already been proposed[33]. The device contains a periodically oscillating gaseous bubble that is externally excited by acoustic waves. The propulsion mechanism is based on the fact that if the oscillating Reynolds number is not too small (typically around 100 for a good performance), the intake and discharge flow in the cavity is asymmetric, which propels the main body of the microswimmer. In earlier studies, the proof-of-concept has been successfully demonstrated using micro-fabricated microswimmers for selective and bi-directional propulsion [17], [33]–[36].

Although acoustic actuation is promising, there is still a long way towards eventual translation of the microswimmer technology into practical in situ biomedical applications. One of the challenges is to track the microswimmers while they are actuated and navigate inside human bodies. A robust tracking strategy available for in situ applications is particularly required in order to locate the microswimmers in real-time and provide feedback for accurate control and

navigation. There has been a limited number of studies that focus on developing appropriate tracking strategies for biomedical applications of the microswimmers. Most of the studies use a camera to record the motion of microswimmers [17], [35], [36]. However, optical imaging is not accessible when the microswimmers are injected into the human body due to its short imaging depth in tissues. Thus, in order to translate the strategy of acoustic actuated microswimmer into clinical applications, a robust tracking strategy for microswimmers available for in vivo applications needs to be established.

### **1.1.2 SRU Imaging**

The idea of locating and tracking ultrasound contrast agents like microbubbles also contributes to the development of the SRU imaging. SRU imaging [37]–[46], is an emerging technology that achieves a high spatial resolution of microvasculature imaging that breaks the acoustic diffraction limit [37]. The technology was inspired by the optical super-resolution imaging that was awarded the Noble Prize in Chemistry in 2014. The basic idea of optical super-resolution technique, including fluorescence photoactivated localization microscopy [47], photoactivated localization microscopy (PALM) [48], and stochastic optical reconstruction microscopy (STORM) [49], is to localize the centroid of each randomly blinking fluorescence sources based on the system point spread function (PSF). The location information of each blinking fluorophore is stacked up over a substantial sequential dataset that was captured by fast camera to form an image spatially resolved with sub-wavelength resolution. By this approach, the spatial resolution down to tens of nanometers was achieved. In SRU imaging, ultrasound contrast agents that travel through vascular network were utilized to replace the role of fluorophore in optical super-resolution, to implement the noninvasive imaging of microvasculature [38]. While the

spatial resolution that can be achieved by ultrasonic super-resolution was not comparable to that by optical super-resolution due to the much longer wavelength of the operating ultrasound compared to the light wavelength, the ultrasound approach achieved a much larger imaging depth. The technology components of SRU imaging mainly consists of ultrafast ultrasound imaging [50], clutter filter [51] that extracts microbubble signals, and the novel microbubble localization algorithms [38], [42], [43], [48], [49] that pinpoint the locations of the microbubbles. With these state-of-art technical components, the vascular structure and the blood flow can be reconstructed with unmatched spatial resolution up to one third of the wavelength of the ultrasound waves [37], significantly outperforming conventional contrast-enhanced ultrasound (CEU) approaches.

In previous studies, the proof-of-concept of SRU imaging technology has been successfully tested in vivo to reconstruct the microvascular network and blood flow inside the organs of some small animals at very high resolution [38], [41], [42], [52], [53]. As an important next step towards translating this technology to clinical applications in future, a preclinical validation study in a specific disease model is particularly required. In this dissertation, the developed SRU technology was applied to two animal disease models. The mouse acute kidney injury (AKI) model was used for investigating the capability of SRU for assessing the abnormal microvascular changes during the injury progression. The technology was subsequently implemented into a clinical mid-frequency probe for the human subject study with chronic kidney disease (CKD). For another important disease associated with atherosclerosis, the rabbit atherosclerotic plaque (AP) model was used for evaluating SRU technology capability in assessing vasa vasorum changes during the atherosclerotic plaque progress.

## 1.2 Objectives

This work mainly consists of two projects, which include the ultrasound tracking of the microswimmers, and the SRU imaging of the microvasculature by locating the flowing microbubbles.

The main objective of the microswimmer study is to:

- 1) Demonstrate the proof-of-concept of ultrasound tracking using two clinical ultrasound array probes in 2-D setup using 2-D maneuverable microswimmers.
- 2) Develop the 3-D ultrasound tracking strategy using two clinical ultrasound array probes fixed to a motor-controlled translational stage and evaluated the performance for tracking the arbitrary 3-D motion of a 3-D microswimmer in benchtop experiments.

The main objective of the SRU project is to:

- 1) develop the SRU imaging algorithm that can identify the microvasculature in vivo within a short scan time and evaluate the most achievable spatial resolution beyond the acoustic diffraction limit given operating ultrasound frequency through the benchtop experiments using uniquely designed microfluidic channels.
- 2) demonstrate the in vivo capability of SRU technology for noninvasive assessment of the microvascular changes by imaging the renal microvasculature in the mouse AKI model, and by imaging the VV in the rabbit AP model.
- 3) Adapt the SRU technology to a clinical curved array ultrasound probe for human kidney imaging and evaluate the performance on healthy human subject and CKD patients for demonstrating the translatability of the technology.

### 1.3 Organization of Dissertation

Chapter 2 introduces the propulsion mechanism and the designs of the acoustically actuated microswimmer and demonstrates the proof-of-concept and accuracy of the ultrasound tracking using the 2D microswimmer that travels two-dimensionally in benchtop experiments. In the experiment, the ultrasound tracking results were compared with the synchronously operated camera tracking. A few typical moving trajectories including straight, instantaneous change in direction, and continuous change in direction like a circular motion, were realized by two different microswimmer designs to evaluate the tracking performance. A laboratory developed tracking algorithm was used to estimate the moving trajectories of the microswimmer captured by both camera and ultrasound.

After demonstrating the proof-of-concept of ultrasound tracking of the microswimmers, we worked on the design and development of the 3-D ultrasound tracking system that hold potential for practical usefulness in situ in biomedical applications. In Chapter 3, the 3-D tracking system, including equipment and the imaging and tracking sequences, is presented. The performance of the 3-D tracking of the microswimmers that is designed to travel three-dimensionally under acoustic actuation was evaluated by comparing with the camera tracking.

Chapter 4 introduces the SRU imaging technology. The developed algorithm was tested through benchtop experiments using microfluidic channels, which mimic microvessels. The most achievable spatial resolution was evaluated in the experiment.

In Chapter 5, the *in vivo* SRU imaging on the mouse AKI model is presented in which the capability of noninvasive quantification of renal vasculature changes associated with AKI-to-CKD progression in mice is shown. In the study, ultrasound scan was performed *in vivo* on mouse kidneys at 21 and 42 days after AKI, uninjured contralateral kidneys, as well as sham kidneys. The

changes in size, relative blood volume (rBV), vessel density, and vessel tortuosity, based on the reconstructed SRU kidney images were quantitatively assessed. The correlation between ultrasound and histological assessment on the vessel density was calculated.

After validating the feasibility of SRU technology for assessing the renal microvessels in the mouse model, we further worked on the adaptation of the algorithm into a clinical ultrasound curved array probe for the application on human kidney imaging. The performance of SRU imaging on the kidneys from both healthy human subjects and patients with CKD is shown in Chapter 6.

In Chapter 7, we applied SRU technology for imaging the VV in the rabbit AP and validated the imaging results by histology and  $\mu$ CT imaging. A study protocol including imaging and validation process is introduced for further extended studies using larger group of animals in the future.

In Chapter 8, we summarize the outcome of the studies presented in this dissertation and discuss the future directions.

## **2.0 Two-dimensional Ultrasound Tracking of the Acoustically Actuated Microswimmers**

*The work presented in this chapter was reprinted from Q. Chen, F.-W. F.-W. Liu, Z. Xiao, N. Sharma, S. K. S. K. Cho, and K. Kim, "Ultrasound Tracking of the Acoustically Actuated Microswimmer," IEEE Trans. Biomed. Eng., vol. 66, no. 11, pp. 1–1, 2019, doi: 10.1109/TBME.2019.2902523, with the permission of IEEE Publishing. © 2019 AIP.*

### **2.1 Introduction**

#### **2.1.1 Propulsion Mechanism of the Acoustically Actuated Microswimmer**

Among variety of the microswimmer propulsion principles, acoustic propulsion is a promising and appealing approach, because it is noninvasive and biocompatible, and largely medium independent [30]–[32]. Acoustic waves can travel through biological tissues to perform wireless actuations on microswimmers. Moreover, it would be a convenient and economic approach if translating into clinical practice.

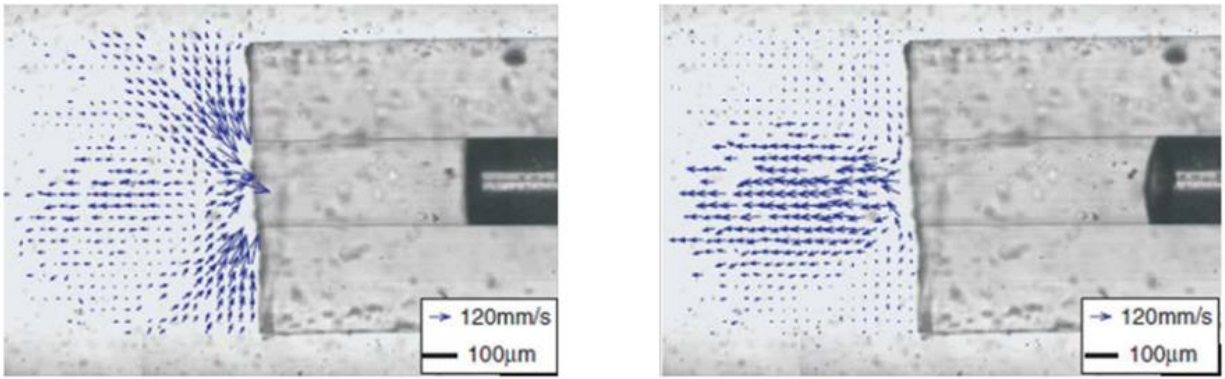


**Figure 1 Flow field of the designed one-channel microswimmer by particle tracking velocimetry measurement. (Reprinted with permission from ref. [33]. Copyright 2006 IOP Publishing Ltd)**

The principle of acoustic propulsion is first introduced by Dijkink et al, based on the fluid mechanical fact that if the Reynolds number is not too small, the fluid intake and discharge from the small tube is asymmetric [33]. The asymmetric flow creates a jet that propels the main body of the microswimmer in the direction opposite to the outgoing direction of the opening of microtubes. Figure 1 shows the flow field of the designed one-channel microswimmer, obtained from particle tracking velocimetry data, during the fluid intake and discharge [33]. When a microswimmer is immersed into water, a gaseous bubble can be trapped in the cavity due to hydrophobicity of the cavity surface. Acoustic wave induces periodical oscillation of a gaseous bubble and this oscillating motion in fluid generates force when the bubble is confined in a one-end-open tube. The oscillation of the gas-liquid interface draws the surrounding liquid from the sides and ejects it in the outgoing direction as shown in Figure 1 [33]. The back-and-forth motion of the gas-liquid interface results in a non-zero time-averaged flow field around the outlet of the tube, by which the miroswimmer is propelled. According to the literature, propulsion force from the bubble oscillation has the following formula [36].

$$F = 0.8\rho A(af)^2 \quad (2-1)$$

In the equation (1),  $F$  is the propulsion force.  $A$  is the cross-sectional area of the tube opening.  $\rho$  is the density of fluid.  $f$  and  $a$  represent oscillating frequency and amplitude. Oscillating amplitude increases as the acoustic pressure on the drone increases. Note that, the oscillating amplitude is maximized when the frequency reaches the resonant frequency of bubbles. The resonant frequency of the cavity in the tube is calculated as

$$f_0 = \frac{1}{2\pi} \sqrt{\frac{\kappa P_0}{\rho L_0 L_B}} \quad (2-2)$$

It reveals that in the same condition, resonant frequency is related to the length of water column between the bubble interface and the channel opening ( $L_0$ ), and the length of the bubble ( $L_B$ ) (Figure 2) [33]. Based on this theory, the oscillation of the gas bubble, therefore the propulsion of the microswimmer can be maneuvered by adjusting the actuation frequency and amplitude.

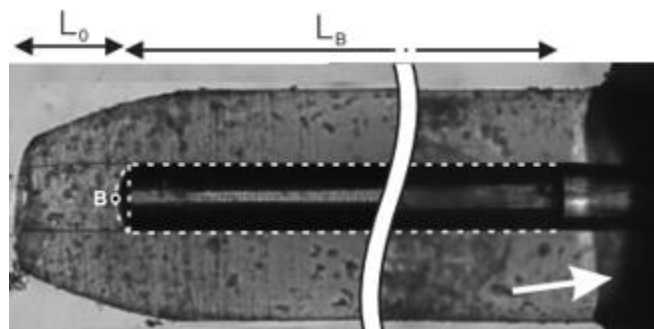


**Figure 2 Illustration of the parameters of the microtube in the microswimmer. (Reprinted with permission from ref. [33]. Copyright 2006 IOP Publishing Ltd)**

In earlier studies, the proof-of-concept of the acoustically actuated microswimmer has been successfully demonstrated using micro-fabricating by several groups [17], [33], [34]. Subsequently, it has been shown that the bubble-based microswimmer can be selectively activated by tuning the applied acoustic wave frequencies to the resonant frequencies of individual cavities and travel in viscous fluid under acoustic actuation[35]. Two dimensional steering and propulsion was also realized by adding multiple orthogonally aligned microtubes with different lengths on the body of microswimmer [36]. Moreover, a microswimmer with armored microbubbles that showed a delayed dissolution and a longer operating life was designed and fabricated[30]. Based on the bubble oscillation principle, a miniaturized endoscope with arrays of cavities, which can adjust the imaging angles under remote acoustic actuation, has been designed and tested in vivo[54].

### **2.1.2 Tracking of the Acoustically Actuate Microswimmer**

Although acoustic actuation is promising, there is still a long way towards eventual translation of the microswimmer technology into biomedical applications. One of the challenges is to track the microswimmers while they are actuated to perform tasks inside human bodies. A robust tracking strategy available for in situ applications is particularly required in order to locate the microswimmers in real-time and provide feedback for accurate control. There has been a lack of studies that focus on developing appropriate tracking strategies for biomedical applications of the microswimmers. Most of the studies use a camera to record the motion of microswimmers[17], [35], [36]. However, optical imaging is not accessible when the microswimmers are injected into the human body due to its short imaging depth in tissues. Ultrasound imaging is an adequate candidate for tracking the miroswimmers in the biomedical environments. Ultrasound imaging can provide larger imaging depth which overcomes the drawbacks of optical imaging. Based on the

design of the microswimmer, high ultrasound contrast can be provided, especially from the cavity with gaseous bubbles encapsulated. Thus, the location of the microswimmer can be identified with high sensitivity, which contributes to the robustness of the tracking. Overall, ultrasound imaging is advantageous with a reasonable spatial and temporal resolution, deep accessibility, as well as safety and low cost [3]. Moreover, ultrasound tracking is compatible with the acoustic actuation method, which is appealing for combining the propulsion and tracking sequence using the same acoustic sensor in the future.

In this chapter, we demonstrate the proof-of-concept of ultrasound tracking of the acoustically actuated microswimmer, for the first time to the best of our knowledge, by comparing with the synchronously operated camera tracking in the two-dimensional (2-D) setup in benchtop experiments. A laboratory developed tracking algorithm is used to estimate the moving trajectory of the microswimmer captured by both imaging approaches of ultrasound and camera for comparison. The tracking performance is evaluated on a few typical moving trajectories including straight, instantaneous change in direction, and continuous change in direction like a circular motion that are realized by two different microswimmer designs.

## **2.2 Materials and Methods**

### **2.2.1 Fabrication and Design of the Microswimmers**

The microswimmers are fabricated by Nanoscribe Photonic Professional system (GT, Germany), a 3D laser printer utilizing two-photon polymerization. By creating hollow microtubes in the microswimmer, the tubes will automatically entrap air inside themselves due to the

hydrophobicity of the material when the microswimmer is being submerged in fluid. Further, tubes with different lengths can be selectively activated at their own resonance frequencies, thus manipulating the direction of the propulsion.

The following two designs of microswimmer are applied in the experiment, which perform (1) linear and (2) bi-directional motion respectively. The first one (Figure 3a) has single microtube passing through its geometric center, thus propelling the microswimmer straight along its axis. The microtube has a diameter of 100  $\mu\text{m}$  and a length of 760  $\mu\text{m}$ . In the opening section, the diameter is suddenly reduced to 80  $\mu\text{m}$  over the length of 60  $\mu\text{m}$  in order to lock the position of the air-water interface via surface tension. This ensures the consistent and desired bubble length through the whole experiment. A continuous waveform (CW) electrical signal of 13Vpp at 9.4 kHz is applied to the piezo-ceramic actuator for an optimal propulsion of this microswimmer. The second microswimmer (Figure 3b) has an additional microtube on each short side of the microswimmer, which is orthogonal to the one at the center. This side microtubes provide propulsion in the orthogonal direction, which enables turning the microswimmer. The bi-directional microswimmer has an 860  $\mu\text{m}$  long center microtube with an 80  $\mu\text{m}$  long neck and the 370  $\mu\text{m}$  long side tube with 30  $\mu\text{m}$  neck. A CW burst signal of 8.3 kHz, 18 Vpp is applied to the actuator to propel both two types of tubes. Due to the difference in length of the tubes, the air cavities inside oscillate with different amplitude in response to the same acoustic signal, resulting in different propulsion forces in each direction that are orthogonal to each other. As a result, the microswimmer travels in a circular trajectory.

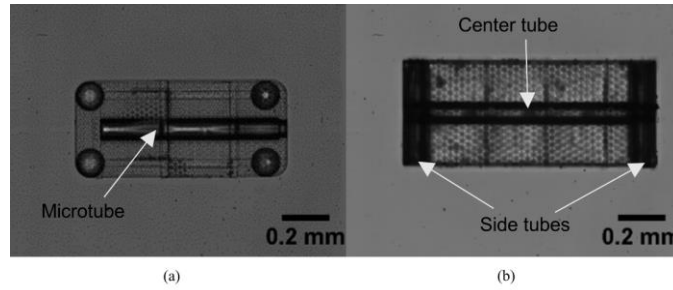


**Figure 3 (a) Microswimmer design 1 with a single microtube (100  $\mu\text{m}$  in diameter and 760  $\mu\text{m}$  in length). (b) Microswimmer design 2 with center (860  $\mu\text{m}$  in length) and side (370  $\mu\text{m}$  in length) microtubes. (Courtesy of Dr. Sung Kwon Cho Lab)**

### 2.2.2 Experiment Setup

The experimental setup is shown in Figure 4. The microswimmer is placed at the bottom of the acrylic water tank. A piezo-ceramic actuator glued to the outer surface of the water tank is utilized to generate the acoustic field that oscillates the air cavity, therefore propels the microswimmer. A CW electrical signal is generated by the function generator 1 (Agilent 33250A) through an amplifier (Trek PZD700A) to the actuator. A camera (Phantom V9.1) and two commercial ultrasound linear array transducers (L7-4, ATL) connected to a programmable ultrasound system (V1 and Vantage, Verasonics, Redmond, WA) are synchronized by the external trigger from function generator 2 (Agilent 33250A) to concurrently record the moving trajectory of the microswimmer both optically and ultrasonically. Since one-dimensional (1-D) ultrasound array transducer from the top of the water surface captures only a cross-sectional image along the ultrasound beam direction (axial-lateral coordinates), two ultrasound probes are used to complement each other for capturing the full two-dimensional motion of the microswimmer that

moves along the bottom surface of the tank (x-y coordinates, see Figure 5). Each ultrasound probe is responsible for tracking the motion along the direction of its lateral axis. Two ultrasound probes are immersed in water at 30 degrees with respect to the water surface on each side of the camera (see Figure 4) and are positioned orthogonal to each other to provide each component of 2-D trajectory (x-y coordinates) respectively. The intention of this unconventional placement is to avoid blocking the light source for optical imaging, and more importantly, to extend the ultrasound elevational field of view for microswimmers (see Figure 5). The reflecting objects located within the beamwidth of the probe can be identified and reconstructed at the center line of the elevation beam by the ultrasound device [55]–[58]. By tilting the probe in elevational direction, the elevation beam area is extended so that the microswimmer moving two dimensionally at the bottom of the water tank can be tracked in a large field of view. Only the motion information along lateral axis is used because of the potential artifact along elevation axis that is attributed to the varied intensity along the elevation axis from the beam center line [55]. The elevation beamwidth projected on the motion plane of the microswimmer is measured to be 7.11mm. To align the camera field of view with the ultrasound imaging planes, a microswimmer is first placed at the center of the camera field of view. Then, the relative position of the two ultrasound probes is adjusted until ultrasound echo from the microswimmer becomes maximum. As a result, the imaging field of view of the camera and ultrasound probes are set to overlap at a  $6.16 \times 6.16 \text{ mm}^2$  area of interest (Figure 5). The frame rate of recording is set to 30 frames per second for both tracking methods.

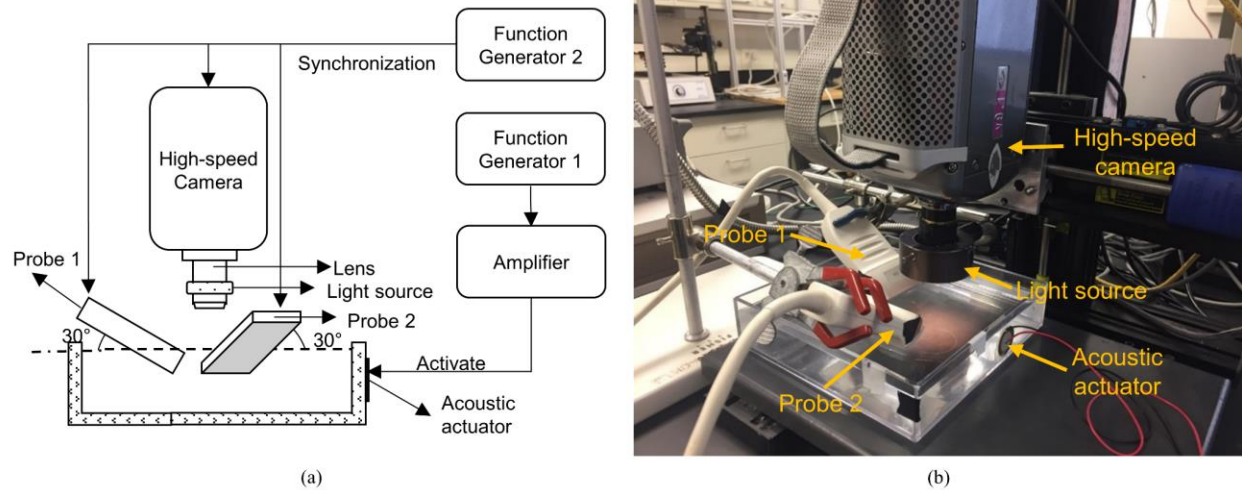


**Figure 4 (a) Experiment schematic. The microswimmer in the water tank is activated by the acoustic actuator glued on the water tank with CW electrical signals transmitted by function generator 1 through the amplifier. Two ultrasound linear array probes (L7-4) and a high speed camera (Phantom v9.1) are utilized to record the movement of the microswimmer simultaneously. Probe 1 and Probe 2 are connected to two separate programmable ultrasound scanners (Verasonic V1 and Verasonic Vantage, respectively). The two ultrasound probes are immersed in water at 30 degrees to the water surface. Function generator 2 is utilized to transmit TTL signals to synchronize the Phantom v9.1 camera, Probe 1 and Probe 2. (b) Experimental setup picture.**

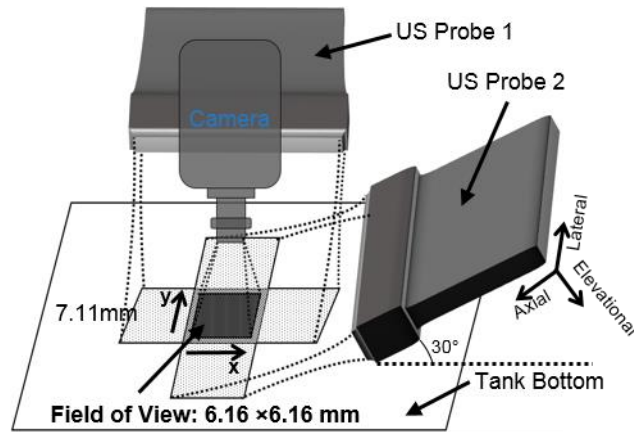


**Figure 5 Imaging field of view. The imaging field of view of each ultrasound probes is 7.11mm (elevation direction) X 36.2mm (lateral direction). The imaging field of view of the camera is 6.16 X 6.16mm with 656 X 656 pixels. The resulting imaging field of view overlaps at a 6.16 X 6.16mm area of interest.**

### 2.2.3 Tracking Algorithm for Camera and Ultrasound

A tracking algorithm is developed for assessing the motion information of the microswimmer, such as displacement and direction, from which the trajectory is reconstructed. The program is written in Matlab (Mathworks, Natick, MA) and applied to both ultrasound and camera video and the reconstructed trajectories from each imaging method are compared to each other. In the preconditioning procedure of the tracking algorithm, median filter is first applied to the images of all frames to minimize any salt-and-pepper noise. Then, the video frames are converted to the binary images by applying a threshold. Afterwards, the microswimmer surface area is identified in the binary image and the geometrical center of the area is determined to represent the position of the microswimmer in each frame. For camera tracking, in each frame the displacement in x-y coordinates is calculated by comparing the geometrical center with that in the first frame. For ultrasound tracking, the tracking algorithm described above is applied to each

ultrasound video acquired by each ultrasound probe to estimate the geometrical center in lateral direction. The displacements in x coordinate (lateral direction of probe 1) and y coordinate (lateral direction of probe 2) are determined by comparing the geometrical centers in lateral direction with those in the first frames in two videos respectively and are then reconstructed into a complete 2-D x-y trajectory.

### 2.3 Results and Discussion

Due to strong acoustic back scattering from the microswimmer body surface and the gaseous microtube, a relatively clear image of the microswimmer with high contrast was shown by ultrasound imaging.

In Figure 6, each row depicts the superimposed time-lapse image from each event of the microswimmer acquired by both camera and ultrasound. Event 1 and Event 2 present the movement of the single-tube microswimmer (linear motion). The single-tube microswimmer (Figure 3a) is designed to move in a straight line under the acoustic actuation at the resonance frequency (9.4 kHz). However, due to the uneven friction at the bottom of the tank surface, the trajectory of the microswimmer slightly deviates at some location. Event 1 in Figure 6 shows that the first microswimmer (single microtube) travels straight from the lower-left corner to the upper-right corner. Event 2 in Figure 6 shows the first microswimmer (single microtube) making a sharp turn when experiencing strong uneven friction from the bottom surface of the water tank. Event 3 in Figure 6 demonstrates the second microswimmer (bi-directional motion) making a circular movement. The yellow dashed rectangles in the ultrasound images denote the region of interest corresponding to camera images.

As shown in Figure 6, a very high contrast of the microswimmer in ultrasound image allows for accurate and robust tracking. However, the appearance of the microswimmer in shape and brightness varies in the ultrasound image as the orientation of the microswimmer to the ultrasound probe changes. This is mainly attributed to the rectangular shape and nonuniform ultrasound contrast over the body of microswimmer. In one occasion, the microswimmer appears to be a single bright spot because of the strong reflection of the air cavity inside the microtube when the microtube is parallel to the lateral axis of the ultrasound probe. In other occasion when the microswimmer rotates, the single bright spot splits into two, most likely when the echoes from the two short edges of the microswimmer dominate. Thus, all the bright spots nearby within the size of microswimmer in ultrasound image are taken and the geometrical center of them is determined as the reference point in the tracking algorithm. In this way, any potential error in locating the microswimmer caused by microswimmer body rotation can be avoided. Note that while the displacement in axial direction from the ultrasound probe can also be used to reconstruct the travel trajectory, because variation of beam intensity over the elevation axis of the ultrasound probe can be significant [55], the motion information along the axial displacement is less reliable. Thus, the lateral displacements acquire by two ultrasound probes are used to track the motion of microswimmers in this study. In Figure 6, the lateral direction of ultrasound probes 1 and 2 are labeled in red and blue respectively, which refers to y and x coordinates in the moving plane of the microswimmer and are in accordance with the coordinates marked in the camera image.

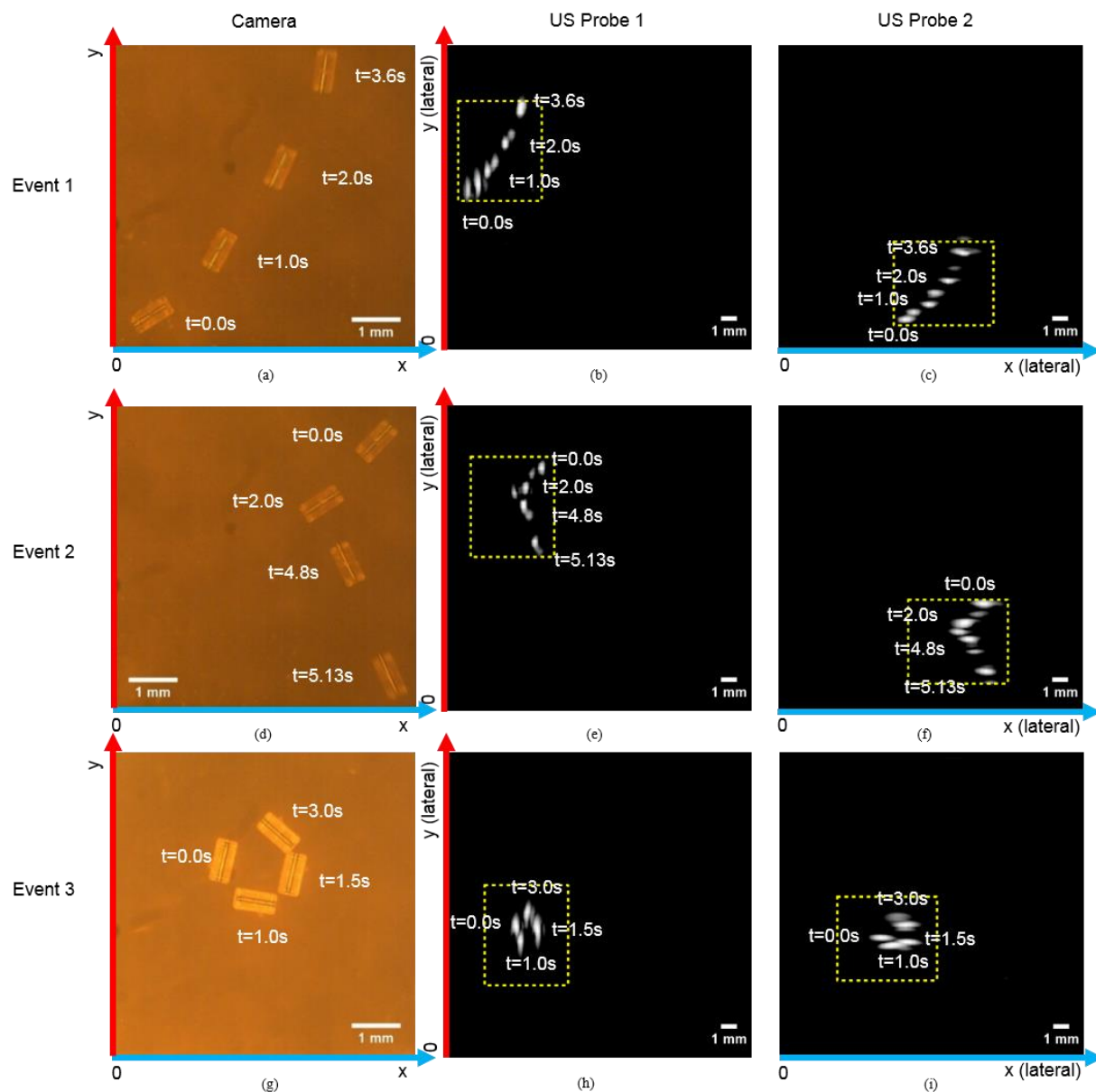


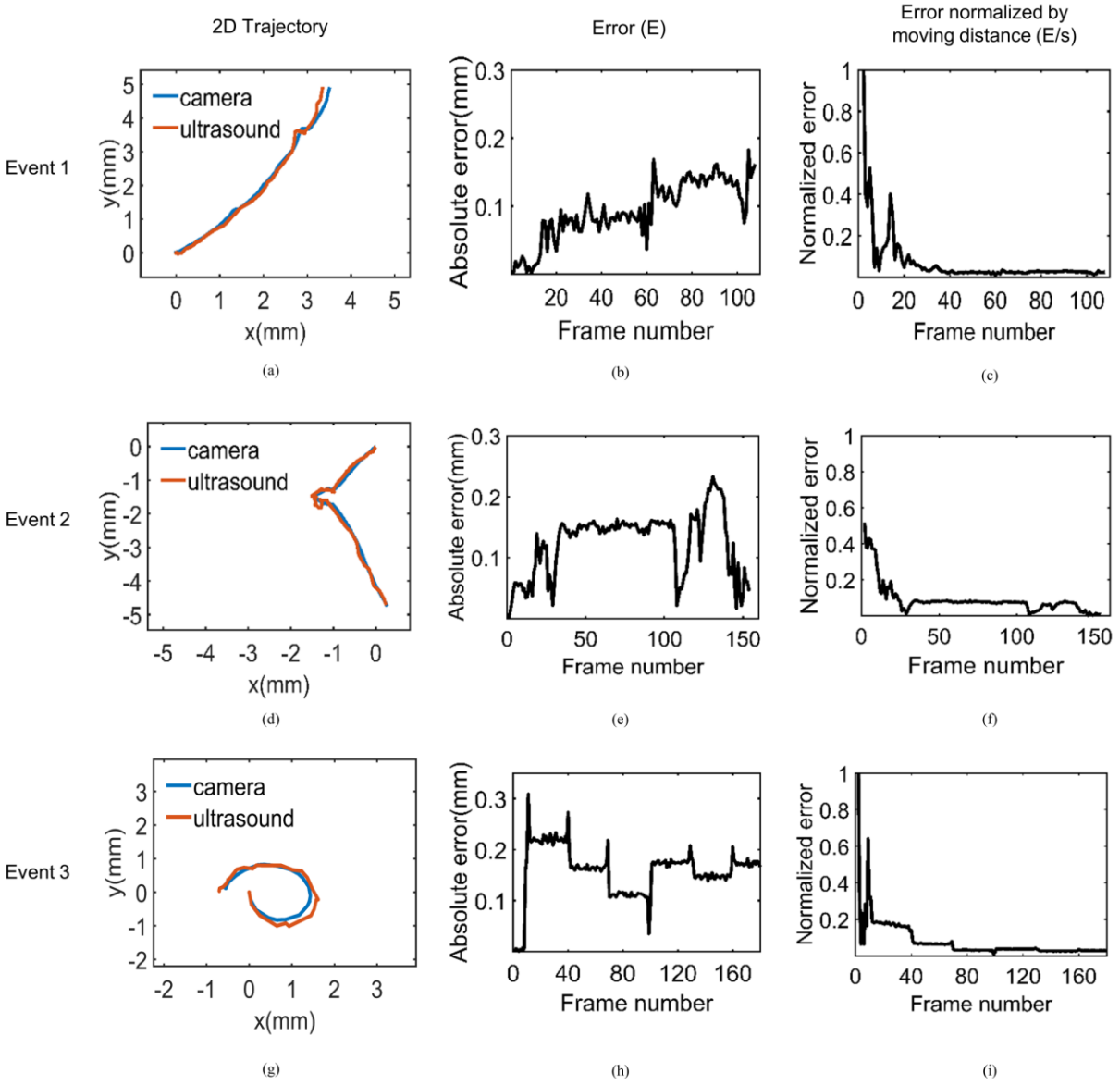
Figure 6 Superimposed time-lapse images from three different events of the microswimmers acquired by both camera and ultrasound probes. Figure. 6a, 6b, 6c are the superimposed time-lapse images for a straight type motion of the single-tube microswimmer acquired by camera, ultrasound probe 1 and probe 2 respectively.

Figure. 6d, 6e, 6f show the microswimmer motion with a sharp turn. Figure. 6g, 6h, 6i show the circular movement of the second microswimmer by camera and two ultrasound probes. The yellow dashed rectangles in Figure. 6b, 6c, 6e, 6f, 6h, 6i denote to the camera images.

In Figure 7, in each row the reconstructed trajectory and the error of each event are shown. The trajectory by ultrasound tracking shown in the first column is reconstructed by the lateral displacement from each ultrasound image: lateral displacement from probe 1 corresponds to y axis; lateral displacement from probe 2 corresponds to x axis. For all three events, the trajectory by ultrasound tracking is in good agreement with the trajectory by the camera. The second column shows the error (E) of ultrasound tracking, which is defined by the discrepancy in the positions between ultrasound and camera trajectory at each frame. The error remains within ultrasound lateral resolution ( $\sim 0.3$  mm) except one frame in Figure 7h, which assures that the method is reasonable and acceptable. Overall, the error of ultrasound tracking is considered mainly to be attributed to the relatively low spatial resolution of operating ultrasound frequency. Moreover, it is noted that the error becomes larger as the microswimmer rotates. This must be due to the fact that the shape of the ultrasound image of the microswimmer changes as its orientation to the ultrasound probe changes. In Figure 7h, a few peaks indicate transiently increased errors when the microswimmer undergoes rotational motions. Due to the limited spatial resolution, ultrasound tracking is not able to identify the rotational information of the microswimmers. In addition, the tracking error can also be attributed to the relatively low signal to noise ratio especially when the microswimmer is located off the imaging center plane in the elevational direction. Column 3 shows the error (E) at each frame normalized to the total moving distance ( $s = \sqrt{\sum_0^t (\Delta x)^2 + (\Delta y)^2}$ ) by that frame. It is noted that the error between ultrasound and camera tracking does not accumulate as the microswimmer travels. It therefore can be expected that when the microswimmer travels a quite long distance, the error of this ultrasound tracking approach stays low over the entire course of travel. In summary, the ultrasound tracking method demonstrates a good accuracy and robustness for three different types of moving trajectories in the benchtop experiments. Taking full

advantage of ultrasound in general such as noninvasiveness and capability of imaging through tissues, real-time ultrasound tracking and control of the microswimmer in biomedical applications in vivo holds a promise.

There is still room to further improve the ultrasound tracking for the acoustically-actuated microswimmers. According to the experiment results, the main limitation of this ultrasound tracking approach includes that the error can be relatively large when the microswimmer rotates, and this approach is not able to detect the angular change of the microswimmer, which is an essential information required for developing a control system for future biomedical application of the microswimmer. Applying a state estimator can be a potential approach to improve the ultrasound tracking results. The estimator corrects the ultrasound tracking results by using predictions from a dynamic model of the microswimmer. Using this estimator, accuracy of the ultrasound tracking can be improved to match the true trajectory [59]. In addition, the rotational information can be distinguished by means of optimizing the design of microswimmer. Some structures with high ultrasound contrast could be incorporated into the microswimmer to label its orientation. In the meantime, the tracking algorithm is required to be further revised and improved. As the feasibility of ultrasound tracking was validated in this study, future steps will be further extending the tracking strategy in a three-dimensional (3-D) setup, which fit more for the real clinical applications that the microswimmer travels three-dimensionally inside the human body.



**Figure 7 Reconstructed trajectory and error analysis of ultrasound tracking for the three different events.**

Figure 7a, 7d, g show the 2-D reconstructed trajectory of the microswimmer from camera and ultrasound imaging. Figure 7b, 7e, 7h demonstrates the error (E) of ultrasound tracking compared to camera tracking (discrepancy between ultrasound and camera trajectory) at each frame. Figure 7b, 7e, 7h show the error (E) of ultrasound tracking normalized to moving distance ( $s = \sqrt{\sum_0^t (\Delta x)^2 + (\Delta y)^2}$ ) at each frame.

## 2.4 Conclusions

In this chapter, we present the ultrasound tracking strategy for the acoustically actuated bubble-based microswimmers. A benchtop experiment was conducted to compare the tracking results on three typical 2-D motion patterns acquired by synchronized camera and ultrasound tracking. The results overall indicate that ultrasound tracking is accurate and reliable to track the motion of the microswimmer. Thus, ultrasound tracking can be considered as a promising approach to track the motion of the microswimmer in biomedical applications. As the first step, this proof-of-concept study built a foundation for the development of a complete tracking system for 3-D motion that will work for practical biomedical environments, and the future clinical translations of this technology.

### **3.0 3-D ultrasound Tracking of the Acoustically Actuated Microswimmers**

#### **3.1 Introduction**

A robust tracking ability is indispensable for the in vivo applications and clinical translation of the microswimmers. In Chapter two, the proof-of concept of ultrasound tracking of acoustically activated swimmers was validated by assessing the accuracy and reliability of ultrasound tracking through in vitro experiments using the microswimmer that travels in various 2-D trajectories. However, it should be considered that in future biomedical applications the microswimmer will travel three-dimensionally inside the human body to perform tasks. Therefore, the system that is able to track the microswimmer in 3-D is particularly required. In this chapter, we present our further developed ultrasound tracking system that can track the arbitrary 3-D motion of the 3-D microswimmers, which was designed and fabricated by our collaborating group [60], in real-time. The tracking accuracy was evaluated in an in vitro experiment by comparing the results to the trajectory recorded by the camera.

## 3.2 Materials and Methods

### 3.2.1 Design of the 3-D Microswimmer

Figure 8 shows the design of the microswimmer that is able to move in three dimensions [60]. To navigate in 3-D space, three types of microtubes, “Lateral 1” (890  $\mu\text{m}$  long  $\times$  2), “Lateral 2” (590  $\mu\text{m}$  long  $\times$  3), and “Vertical” (470  $\mu\text{m}$  long  $\times$  6), are placed in different orientations and positions inside the microswimmer body. The individual resonant frequencies of the microtubes were 5.9 kHz, 7.9 kHz, and 11.7 kHz, respectively. A decrease in diameter near the tube opening introduces a physical barrier to fix the interface of the bubble and thus maintains its length during bubble trapping and operation [61]. As the propulsion direction is opposite to the outgoing direction of the opening of microtubes, 3-D propulsion can be achieved by solely or jointly actuating the microtubes: (1) propelling upward by Vertical, (2) yawing clockwise or counterclockwise by Lateral 1 or 2 respectively, (3) moving forward by Lateral 1 and 2 simultaneously at 6.3 kHz and (4) downward by gravity. The opening of Vertical tubes is placed above the bottom of the microswimmer to have a room to develop microstreaming flow for stable taking off/landing on the bottom surface. In addition, a dummy empty tube with both ends open in the top corner is intentionally added to reduce the mass in the upper part of the microswimmer.

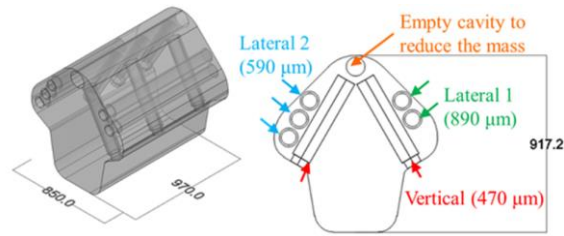


**Figure 8** The design of 3-D microswimmer with the overall view (left) and the front view (right). (Courtesy of Dr. Sung Kwon Cho Lab)

### 3.2.2 3-D Ultrasound Tracking System

The Figure 9 presents the schematic of the system designed (a) and the experiment setup picture (b) for 3-D ultrasound tracking of the microswimmer. The 3-D microswimmer is placed in water-glycerin solution (1:10) in the water tank, actuated by the acoustic actuator. The density of the solution is close to the density of the 3-D microswimmer, which creates a neutral buoyancy, so that the microswimmer can be actuated easier in the vertical direction. For the moving trajectory presented in this work, the microswimmer was activated by the piezo-ceramic actuator with continuous waveform signal of 99 V<sub>pp</sub> at 10.7 kHz. Two ultrasound probes were operated by a programmable ultrasound system (Vantage256, Verasonics, Redmond, WA) simultaneously to image the microswimmer through the acrylic wall of the water tank. At the beginning of the experiment, the microswimmer was placed in the overlaps of the elevation beams of the two probes to assure it is seen by both probes. Ultrasound plane wave imaging is utilized to capture the locations of the microswimmer. Any motion in axial and lateral directions within the field of view can be tracked by the two probes from their initial positions. When the microswimmer moves along the elevational direction, the probes are driven by the step motor along the elevational axis together with the microswimmer to keep the microswimmer inside the ultrasound field of view at

all time. The ultrasound images of each frame from the two probes are transferred real-time to a Matlab external function with the control algorithm. The control algorithm senses the elevational motion of the microswimmer and sends the control commands to the step motor controller. The high-speed camera (PL-D732CU-T, Pixelink, Rochester, NY) is also held at the certain location on the step motor, by which the focus overlaps with the ultrasound imaging plane, and is driven by the motor with the same command along the elevational axis to track the microswimmer simultaneously. The trajectories of the microswimmer are reconstructed from the videos recorded by both ultrasound and camera acquisition using the algorithm described in Chapter 2 to evaluate the tracking accuracy. The whole system including ultrasound and camera system will be synchronized by the external trigger from a function generator (Agilent 33250A). The frame rate of the image acquisition is 20Hz. The image data transfer, calculation in the control algorithm, and the motor motion are executed within the time between every two ultrasound image frames (0.05 s) to ensure the real-time availability.

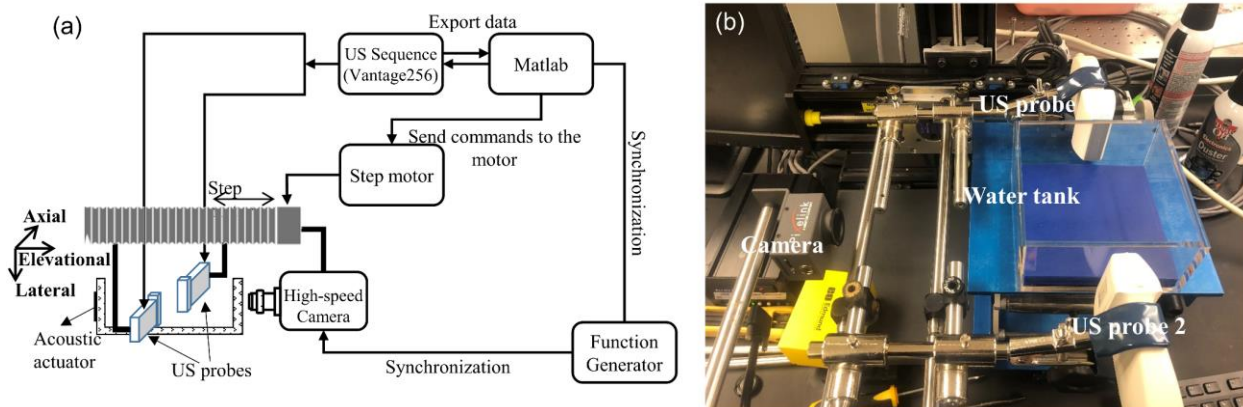
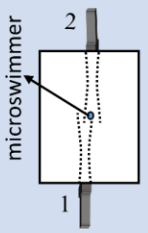
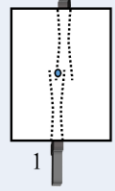


Figure 9 (a) Schematic and (b) picture of the experimental set up.

### 3.2.3 Control Algorithm

The control algorithm is meant to keep the microswimmer in the intersection area of the elevation beams of the two probes all the time during the tracking. The microswimmer is identified as a bright spot in the ultrasound image, which contains the pixel with peak intensity. During the tracking, two ultrasound images from each probe are transferred to the control algorithm, which is embedded in the external function. In the control algorithm, the relative peak pixel intensities of the two images, which is the peak intensity of the ultrasound image normalized to the summation of the intensity of all pixels, are compared to determine the elevational direction of the swimmer motion. Two scenarios (Figure 10) are considered in the control algorithm for operating the step motor accordingly. The motor speed is tuned to 2.5 mm/s, based on the typical microswimmer moving speed, to ensure that the microswimmer will not be lost outside the overlapped beams between two frames.

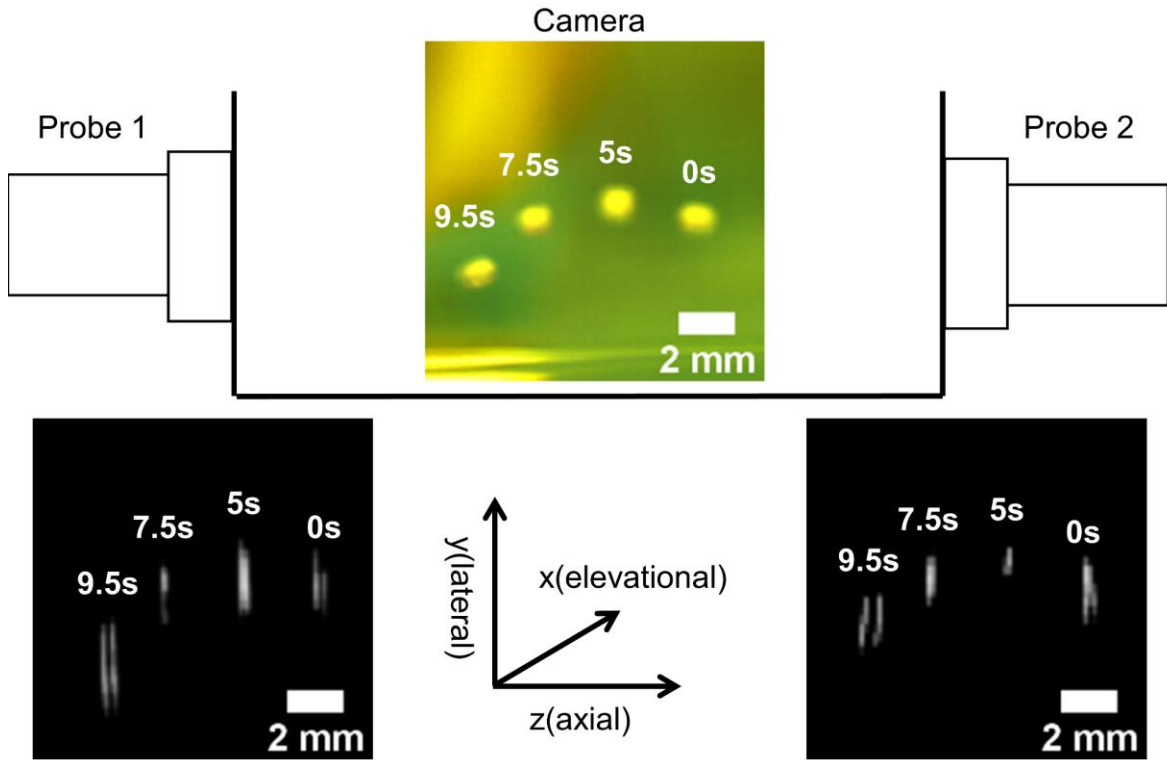
Scenario	Conditions	Command
Top view 	The signal intensity of the microswimmer is larger in probe 2	Move right
Top view 	The signal intensity of the microswimmer is larger in probe 1	Move left

**Figure 10 Two scenarios in the control algorithm.**

### 3.3 Results and Discussion

In this 3-D tracking system, the microswimmer motion in the lateral-axial (y-z plane as noted in Figure 11) coordinate of the ultrasound probe can be captured by ultrasound imaging. As the microswimmer moves in elevational (x) direction, the control algorithm determines the moving direction and drives the motor that holds the two probes and the camera to follow the microswimmer in the elevational direction. Therefore, the motion in y-z plane was captured by both camera and ultrasound, while the x-direction motion was roughly represented by the motion of the motor. Figure 11 presents the superimposed time-lapse images of the microswimmer in the y-z plane acquired by camera and ultrasound. Due to the friction in the fluid, the motion of the 3-D swimmer can be considered as an arbitrary undetermined motion in response to the acoustic

actuation. During the motion, the swimmer was successfully tracked and therefore kept in the field of view of both ultrasound probes and the camera at all time, while the probes were being driven by the motor to follow the microswimmer motion in the x direction.



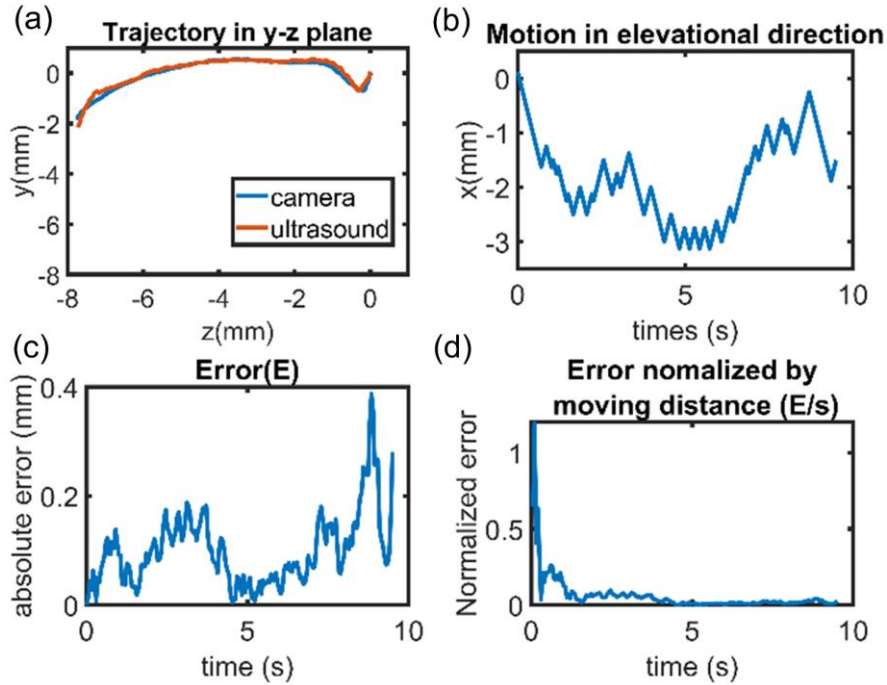
**Figure 11 Superimposed time-lapse images of the microswimmers acquired by the camera and ultrasound probes.**

Figure 12 (a) presents the reconstructed trajectory in the y-z plane from the camera and ultrasound tracking using the tracking algorithm described in 2.2.3. It should be noted that both the displacement in axial and lateral directions of the ultrasound images acquired by each probe can be used to reconstruct the trajectory. Therefore, the trajectories by ultrasound can be derived from the frames acquired by either of the probes. In this work, we calculated the displacements by

averaging the results from the two probes to minimize the error. It can be found in Figure 12 (a) that the trajectory by ultrasound tracking is in good agreement with the trajectory by the camera. The step-motor displacement during the tracking is shown in Figure 12 (b), which corresponds roughly to the elevational motion of the microswimmer. The tracking error at each frame, which is defined by the discrepancy in the positions between ultrasound and camera trajectory, is shown in Figure 12 (c). The tracking errors remain mostly within the ultrasound lateral resolution ( $\sim 0.3$  mm), which indicate the reliability of the ultrasound tracking. Generally, the tracking error by ultrasound is mainly attributed to the relatively low spatial resolution compared to camera. Plane wave ultrasound imaging, which can provide a high frame rate with a compromised spatial resolution, was used in the tracking sequence in order to ensure the real-time operation. Moreover, the tracking accuracy is also sensitive to the orientation of the ultrasound probes. The ultrasound imaging planes of the two probes are design to be perpendicular to the x-direction that step motor moves. Any angle deviation from the normal will add to the errors in the tracking results. The error (E) at each frame normalized to moving distance by that frame remains relatively low as shown by Figure 12 (d), which indicates the error does not significantly accumulate as the microswimmer travels. In summary, our lab-designed 3-D ultrasound tracking system can accurately track the arbitrary motion of the 3-D microswimmer under acoustic actuation. The tracking system is readily available for the ex-vivo tissue experiment as the future step towards further translation.

However, there is still room for further improvement of the 3-D tracking system. Firstly, as mentioned above, ultrasound plane wave imaging was used to capture the motion at very high frame rate, which compromises the imaging spatial resolution. Compounded plane wave imaging with a certain number of transmit angles, which is determined by carefully balancing the trade-off between spatial resolution and the frame rate, can be used to reduce the tracking error. As for the

orientation of the probes that may affect tracking accuracy, a custom-designed probe holder that fix the relative location of the two probes and the step motor is suggested for future ex-vivo and in vivo experiments. For potential improvement of the lateral tracking accuracy, an ultrasound probe with finer pitch in lateral direction would be appealing.



**Figure 12 (a) Reconstructed trajectories in y-z plane by camera and ultrasound. (b) Step-motor displacement in elevational direction. (c) Error (E) of ultrasound tracking compared to camera tracking (discrepancy between ultrasound and camera trajectory) at each frame. (d) Error (E) of ultrasound tracking normalized to moving distance ( $s = \sqrt{\sum_0^t (\Delta x)^2 + (\Delta y)^2}$ ) at each frame.**

Regarding the future directions, evaluating the 3-D ultrasound tracking of the microswimmer motion in ex-vivo animal tissues, such as porcine eyeball cavity, is expected. This would be a preliminary test for one of the potential applications of the microswimmer that

navigates through the eyeball cavity towards the retina to deliver drugs. In this work, to provide an arbitrary moving trajectory, the trajectory of the 3-D microswimmer is not pre-designed and controlled. In the future, a feedback control algorithm would be added when it is ready to maneuver the motion of the microswimmer in the desired trajectory by adjusting the actuation frequency and amplitude based on the feedback from the ultrasound tracking. Therefore, the experiment with more controlled 3-D propulsion and tracking can be envisioned.

### **3.4 Conclusions**

In the work presented in this chapter, we propose the 3-D ultrasound tracking system using two clinical ultrasound probes that were translated by the step motors. The performance of the 3-D tracking system was evaluated in a benchtop experiment by tracking the arbitrary motion of the newly designed 3-D microswimmer. The results demonstrate that the ultrasound tracking system is able to capture the arbitrary 3-D motion of the microswimmer at all time and exhibits a relatively high accuracy when compared to the trajectory recorded by the camera. Thus, our designed tracking system could be a potential approach for tracking the 3-D microswimmer motion in practical biomedical applications and may promote the future clinical translation of the microswimmer technology.

## 4.0 SRU Imaging: In Vitro Validation of the Spatial Resolution

### 4.1 Introduction

The spatial resolution of conventional ultrasound imaging methods is inherently limited by the acoustic diffraction limit of half of the pulse length, which means that two targets located closer than the acoustic diffraction limit cannot be differentiated by ultrasound imaging. Inspired by the optical super-resolution imaging techniques [47]–[49], SRU imaging was introduced [38]–[41], [62] for noninvasive imaging of microvasculature with the spatial resolution beyond the acoustic diffraction limit. Figure 13 illustrates the overall block diagram of the SRU imaging technique [63]. The basic idea of the SRU imaging is to locate the centroid of each spatially isolated microbubbles that are injected and travel through the vascular network over stacks of acquired frames. Then the location information of the microbubbles from all the frames are summed up to form the complete vascular network with sub-wavelength precision. By this approach, spatial resolution can theoretically be improved up to one tenth of the wavelength [38]. In general, the key technical component for implement the SRU imaging consists several state-of-art techniques, including ultrasound contrast agents that enhance hyperechoic contrast, ultrafast frame rate imaging [50], advanced clutter filtering technique that can extracts signals only from microbubbles circulating in the vessels with low flow rate and moderate tissue motion[51], and novel microbubble center localization techniques that pinpoint the center of each microbubble from the extracted signals [38], [42], [43], [48], [49].

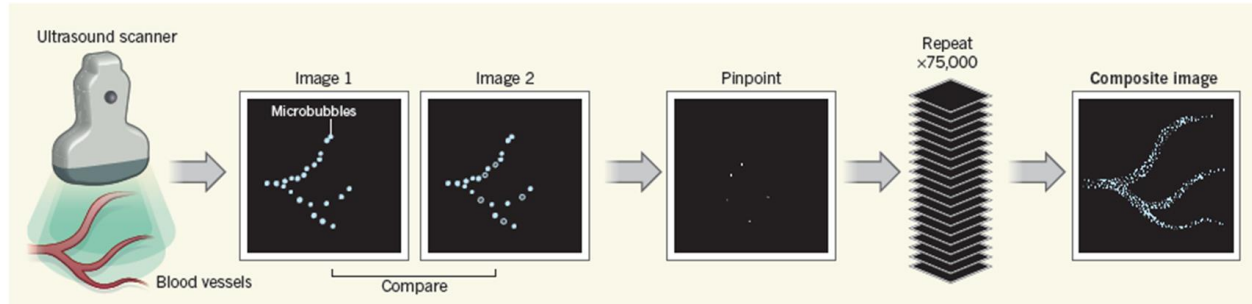


**Figure 13** An illustration of the concept of the SRU imaging technique. (Reprinted with permission from ref. [63]. Copyright 2015 Springer Nature)

However, one drawback of the conventional SRU imaging approaches that utilizes microbubble center localization algorithm is the requirement of huge number of frames, since the algorithm only locate the centroid of spatially isolated microbubbles, rejecting the signals from overcrowded MBs in the process. Typically, tens of thousands of frames corresponding to a scan time of several minutes is required to reconstruct one final SRU image. The long scan time hinders the clinical applications, especially under conditions in which the tissue motion is pronounced. To shorten the scan time, super-resolution optical fluctuation imaging (SOFI) technique for SRU was introduced [44], while the spatial resolution achieved is relatively low compared to center localization algorithm. Our group introduced a deconvolution-based SRU imaging technology to significantly improve the temporal resolution to  $<1$  second while preserving the spatial resolution at the same time [42]. The Richardson-Lucy (RL) deconvolution algorithm used in our SRU technique is a non-linear iterative deconvolution method which has been widely used for deblurring image with the presence of Poisson distributed noise in astronomy and biomedical applications [64]–[67]. By this method, each microbubble location from the clumped microbubble signals can be located with predetermined PSF, thus making full use of all the frames and shorten

the scan time. In the previous study, our group applied the developed deconvolution-based SRU imaging technology for imaging the vasa vasorum in the rabbit atherosclerotic plaque in vivo. The temporal resolution of 0.6 seconds was achieved, and the vessel as small as 41  $\mu\text{m}$  was identified using a 7.7 MHz linear array transducer in this preliminary test [42]. However, one problem of this preliminary study is that there was no proof of the true diameter of the identified smallest vessel, which means that the spatial resolution of the proposed technology cannot be concluded. Since now, few studies have been performed to validate the spatial resolution of SRU imaging in the experiments with ground truth. Therefore, the study to validate the imaging capability especially spatial resolution in a rigorous manner is particularly required before proceeding to the systematic in vivo animal studies.

In this chapter, we tested our deconvolution-based SRU imaging algorithm on the custom-designed microfluidic channels with flowing microbubbles in vitro. The spatial resolution of SRU imaging was validated by identifying the two closely located microchannels.

## **4.2 Materials and Methods**

### **4.2.1 Design of the Microfluidic Chip**

The spatial resolution of the deconvolution-based SRU imaging was tested in vitro by imaging the vessel mimicking microchannels molded in polydimethylsiloxane (PDMS). The design of the custom-made PDMS microfluidic chip (uFluidix Inc., Canada) is shown in Figure 14 in top (a) and longitudinal view (b). Figure 14(c) is the photo of the chip in top view. A single microchannel of 60 x 30  $\mu\text{m}$  from the inlet is separated into two microchannels of 30 x 30  $\mu\text{m}$

toward the outlet with the closest wall-to-wall distance of  $30\ \mu\text{m}$ . The size of the chip is  $25 \times 8 \times 6$  mm. Such design was to mimic the microvessels that are located closely within the acoustic diffraction limit of one-half wavelength ( $50\ \mu\text{m}$  at  $15.6\ \text{MHz}$ ). Figure 14(d) shows the microscopy image of the microchannels around the bifurcation that is marked by the dotted rectangle in Figure 14(a).

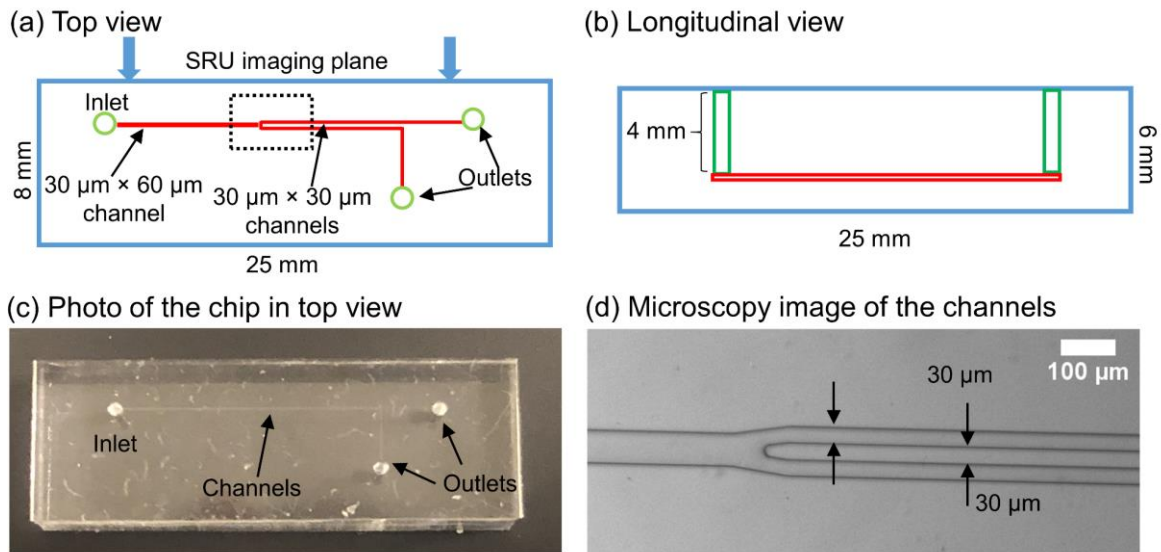


**Figure 14** Design of the microfluidic chip in top view(a) and longitudinal view (b). (c) Photo fo the chip in top view. (d) Microscopy image of the microchannels around the bifurcation that marked in the dotted rectangle in (a).

#### 4.2.2 SRU Imaging Protocol

Lab-made microbubbles (MP1950,  $3\text{-}5\ \mu\text{m}$ ) [68]–[70] at the concentration of  $3 \times 10^7$  MBs/mL were injected into the microchannels from the inlet at a constant flow rate of  $0.6\ \mu\text{L/h}$  using a syringe pump (KDS120, KD Scientific). A  $15.6\ \text{MHz}$  linear array probe (L22-14v,

Verasonics, Kirkland, WI) connected to ultrasound system (Vantage 128, Verasonics, Remond, WI) was used to image the microchannels from the side of the chip while placed in the water tank to access the imaging plane as shown in Figure 14(a). When the microbubbles flow through the microchannels steadily, multi-angle US plane wave imaging with five steer angles ( $-3^\circ$ ,  $-1.5^\circ$ ,  $0^\circ$ ,  $1.5^\circ$ ,  $3^\circ$ ) was implemented to collect the radiofrequency (RF) data of 500 frames at an effective frame rate of 500 Hz. The acquired raw RF data were processed offline to reconstruct the final SRU image.

#### **4.2.3 SRU Signal Processing Procedure**

The SRU signal processing after ultrasound data acquisition was implemented offline in MATLAB (Mathworks, Natick, MA). Figure 15 shows the pipeline of the SRU signal processing procedure. The acquired raw RF channel data were beamformed using the delay-and-sum algorithm and envelope detected for B-mode processing. The echo signals from microbubbles were extracted from envelope-detected B-mode data by a spatio-temporal eigen-based decomposition clutter filter (SVD filter) [51]. To determine the optimized higher and lower cutoff of the filter, the turning points where the singular value curve appeared to be approximately linear were first roughly estimated. Several values around the turning points were chosen as the cutoff to test the clutter rejection performance. The cutoff points with best filtering performance were then manually selected as the final thresholds. The images containing only microbubble signals were then interpolated to an increased pixel precision of  $10\ \mu\text{m} \times 10\ \mu\text{m}$  and deconvolved using RL deconvolution algorithm [64]–[66] with the pre-estimated PSF to localize the center of each microbubble. The final super-resolution image was achieved by summing up 300 frames of the deconvolved data that is corresponding to 0.6 seconds.

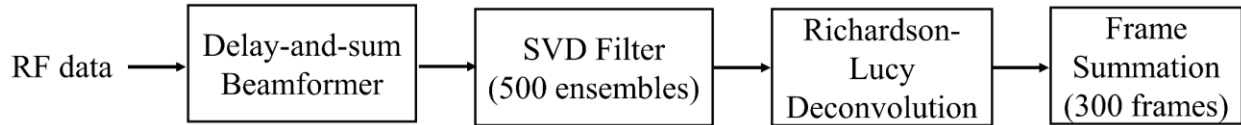


**Figure 15 SRU signal processing pipeline.**

### 4.3 Results and Discussion

The conventional B-mode image of the microfluidic channels with flowing microbubbles is shown in Figure 16(a). Since the distance between the two separated channels ( $30\ \mu\text{m}$ ) is smaller than the acoustic diffraction limit of the operating ultrasound frequency ( $50\ \mu\text{m}$ : half wavelength at 15.6 MHz), the two channels cannot be differentiated and therefore were shown as one thick channel. In the reconstructed SRU image, the two channels were successfully separated as two microchannels (Figure 16b).

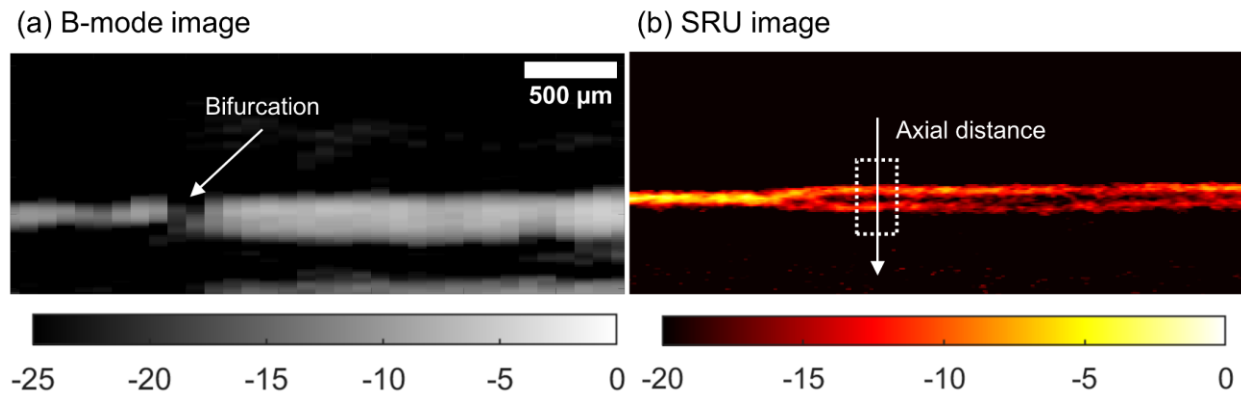


**Figure 16 (a) B-mode image of the microfluidic channels. (b) Reconstructed SRU image of the microfluidic channels.**

To examine the capability of separating two closely located microchannels, the (closest) wall-to-wall distance between the two channels was estimated by averaging the estimated distance between the two channels in the 200  $\mu\text{m}$  long area marked in the white dotted box. Figure 17 shows the signal magnitude profile of the two channels in axial direction averaged over 200  $\mu\text{m}$  along the channel. At the -6 dB point, the wall-to-wall distance measured  $30 \pm 7 \mu\text{m}$ , which is close to the real wall-to-wall distance between the two channels according to the design of the microfluidic chip.

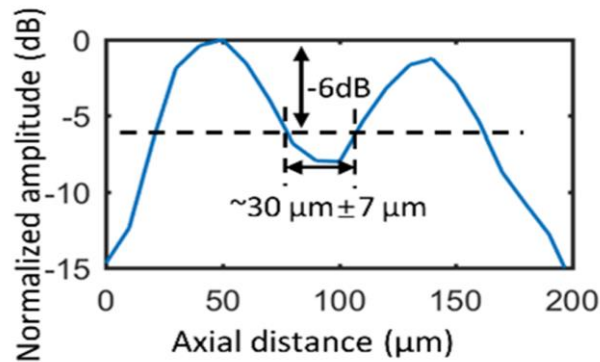


**Figure 17 Axial signal magnitude profile averaged over 200  $\mu\text{m}$  along the channel in the area marked in white dotted box in Figure 16(b).**

Overall, it is demonstrated that the developed deconvolution-based SRU imaging technology can separate and identify the objects located as close as 30  $\mu\text{m}$  using 15.6MHz ultrasound. Following the in vitro validation, further in vivo animal studies using SRU imaging were undertaken in the next chapter. The microfluidic chip proposed in this study can be used as a practical tool for systematically validating the spatial resolution and evaluating the performance

of different SRU algorithms. As a next step, a well-designed microfluidic chip with various channel sizes and wall-to-wall separation distances is suggested for further systematic evaluation of the spatial resolution of different SRU algorithm under different operating frequencies. It should be noted that some area of the channels in the SRU image appears to be thicker than the real size. This could be due to the localization error of the deconvolution algorithm when the microbubble density is too high. A finer control of the perfusion is needed for evenly distributed microbubbles in the channels. Since the focus of this study is to demonstrate the capability of SRU for differentiate two closely located objects, which is defined as spatial resolution, the discrepancy in size would not affect the major finding of this study.

#### **4.4 Conclusions**

By using the custom-designed microfluidic chip as ground truth, the expected spatial resolution of 30  $\mu\text{m}$  of the deconvolution-based SRU imaging was validated in this in vitro experiment. This evaluation assured the subsequent in vivo animal studies of SRU. Moreover, the use of the microfluidic chip can be a practical approach for the systematic evaluation of the imaging capabilities of different SRU algorithms.

## 5.0 SRU Imaging for Noninvasive Assessment of Renal Microvasculature Changes in Mouse AKI Model

*The work presented in this chapter was reprinted from Q. Chen, J. Yu, B. M. Rush, S. D. Stocker, R. J. Tan, and K. Kim, "Ultrasound super-resolution imaging provides a noninvasive assessment of renal microvasculature changes during mouse acute kidney injury," Kidney Int., vol. 98, no. 2, pp. 355–365, Aug. 2020, doi: 10.1016/j.kint.2020.02.011, with the permission of Elsevier Publishing. © 2020 Elsevier.*

### 5.1 Introduction

AKI is a rapid loss of renal function occurring in up to 20% of hospitalized patients [71]. The presence of AKI is associated with both increased immediate hospital mortality and the long-term development of permanent or CKD and eventually end-stage renal disease. It is well accepted that AKI can lead to CKD and this risk is affected by AKI severity, duration, and frequency as well as age and presence of CKD or other comorbid conditions [72]–[76]. One proposed mechanism for AKI-to-CKD progression is the deterioration of the renal microvasculature after initial injury, a process known as microvascular rarefaction. Loss of microvascular density, particularly in the peritubular capillaries, has been described in a variety of studies of ischemic AKI [77]–[81], as well as in human kidneys that undergo ischemia in the process of transplantation [82]. The mechanisms of microvascular rarefaction are still under investigation, but studies have implicated endothelial dysfunction and/or apoptosis, as well as altered vascular endothelial growth factor (VEGF) secretion [78]. The loss of the microvasculature would lead to the impairment of

renal perfusion and therefore a predisposition for acute and chronic ischemic injury [77], [83]–[85]. However, the diagnostic tools that enable noninvasive and quantitative monitoring of renal microvascular changes during AKI-to-CKD progression are still lacking.

Several diagnostic imaging technologies, including magnetic resonance imaging (MRI) [86], [87], micro-computed tomography imaging ( $\mu$ CT) [88], [89], and ultrasound imaging [90]–[92], have been employed in pre-clinical studies to noninvasively and quantitatively evaluate the changes of renal microvasculature and renal perfusion for predicting and monitoring progressive kidney disease. However, MRI and CT scans have important limitations when used in humans. MRI requires long imaging times and the gadolinium-based contrast has been associated with development of nephrogenic systemic fibrosis, a debilitating disease [93]. Meanwhile, the risk of contrast-induced nephropathy and exposure to radiation limits the widespread or repeated use of enhanced CT scans in patients with kidney disease [94]–[97]. In addition, these imaging systems are bulky and costly, especially when used for serial imaging.

Ultrasound imaging has the advantage of safety, noninvasiveness, portability, affordability and ease of use. Several approaches, such as Doppler ultrasound imaging [92] and CEU imaging [90], [91], have been explored to diagnose AKI-to-CKD progression in animals and humans. However, neither technique provides spatial resolution high enough for assessing microvessels, especially in the cortex. This is mainly because of the insufficient sensitivity and the acoustic diffraction limit of the operating ultrasound frequency. SRU imaging [37]–[46], is an emerging technology that can achieve a high spatial resolution of vasculature beyond the acoustic diffraction limit [37]. As demonstrated in Chapter 4, the emerging SRU imaging technology can identify the microvessels with spatial resolution up to  $30\ \mu\text{m}$  ( $< \lambda/3$ ), significantly outperforming conventional US approaches. SRU imaging technology has already been tested in vivo on animals for imaging

microvessels in different organs, such as brain [38], [98], kidney [43], [44], [52], [99]–[101], mouse ear [41], rabbit lymph node [53] and tumor cells [44]–[46], [102], [103], by different group for purpose of demonstrating the technical capability. Unlike iodinated CT contrast, ultrasound contrast agents (microbubbles) are not nephrotoxic and are generally safe when given systemically [104]–[107]. They are already widely used clinically for left ventricular opacification in cardiac echocardiography [106]. In combining high spatial resolution with the benefits of traditional ultrasound, SRU has the potential to accurately assess changes of kidney vasculature during the progressive kidney disease without harming the subject.

In this study, we applied SRU imaging technology with high spatio-temporal resolution in a mouse ischemia-reperfusion (IRI) kidney injury model to demonstrate its ability to quantitatively evaluate the microvasculature during AKI-to-CKD progression. US scan was performed in vivo on kidneys at 21 and 42 days after IRI, uninjured contralateral kidneys, as well as sham kidneys. We quantitatively assessed the kidneys for changes in size, relative blood volume (rBV), vessel density, and vessel tortuosity, based on the reconstructed SRU kidney images. The results from US assessment on vessel density was correlated with histological analysis as a gold standard for validation.

## **5.2 Materials and Methods**

### **5.2.1 Mouse Kidney Injury Model**

C57BL/6 mice (Jackson Laboratory cat# 000664, Bar Harbor, ME) were subjected to unilateral IRI as previously described [108]. Briefly, mice were anesthetized and placed on a heating pad to maintain a 37°C body temperature which was confirmed with continuous rectal measurements. Using a ventral incision, the right kidney and its pedicle was isolated and clamped with atraumatic surgical clips (#RS-5459, Roboz, Gaithersburg, MD) for 30 minutes. The clip was removed and incision closed. The contralateral (left) kidney was not injured and served as an internal control. CD31 and all US analysis were performed on contralateral, 21 days post-injury and 42 days post-injury kidneys, as well as the sham kidneys from mice that did not undergo surgery (n = 5 for each group).

### **5.2.2 Experiment Protocol**

SRU imaging was performed on the sham kidneys, contralateral kidneys, injured kidneys at 21 days post-injury and 42 days post-injury (n = 5 each group) (Figure 18c). Mice were anesthetized with isoflurane (2% in 100% O<sub>2</sub>) for the placement of a microrenathane catheter (MR-025, Braintree Scientific) in the jugular vein for contrast agent injection. Longer term anesthesia was achieved with ketamine (100 mg/kg) / xylazine (10 mg/kg) for the ultrasound procedure. Paraspinal fur was shaved for US access (Figure 18b). The SRU imaging sequence was operated

by a programmable US system (Vantage 128, Verasonics, Remond, WI) equipped with a 15.6MHz linear array US probe (L22-14v, Verasonics, Kirkland, WI). Regular B-mode US imaging was used to locate the position and orientation of the US probe, so that the entire mouse kidney in the maximum longitudinal axis was viewed in the imaging plane. Then, the position and orientation of the US probe was fixed by a probe holder to ensure the stability of the probe throughout the data acquisition process. Commercial lipid-shelled microbubbles (Definity, diameter 1- 4  $\mu\text{m}$ , Lantheus Medical Imaging, N. Billerica, MA), served as US contrast agents, were diluted with phosphate-buffered saline (PBS) to concentration of 10% and intravenously injected with a bolus of 0.1 mL through the jugular catheter. About ten seconds post injection, imaging data of 1000 effective frames were acquired using multi-angle US plane wave imaging with five angles ( $-3^\circ$ ,  $-1.5^\circ$ ,  $0^\circ$ ,  $1.5^\circ$ ,  $3^\circ$ ) for spatial compounding at an effective frame rate of 250Hz for subsequent signal processing. The kidneys were imaged without the need for organ exteriorization or skin incision. After the US scan, the mouse was euthanized and kidneys harvested for weight measurement and histology staining.

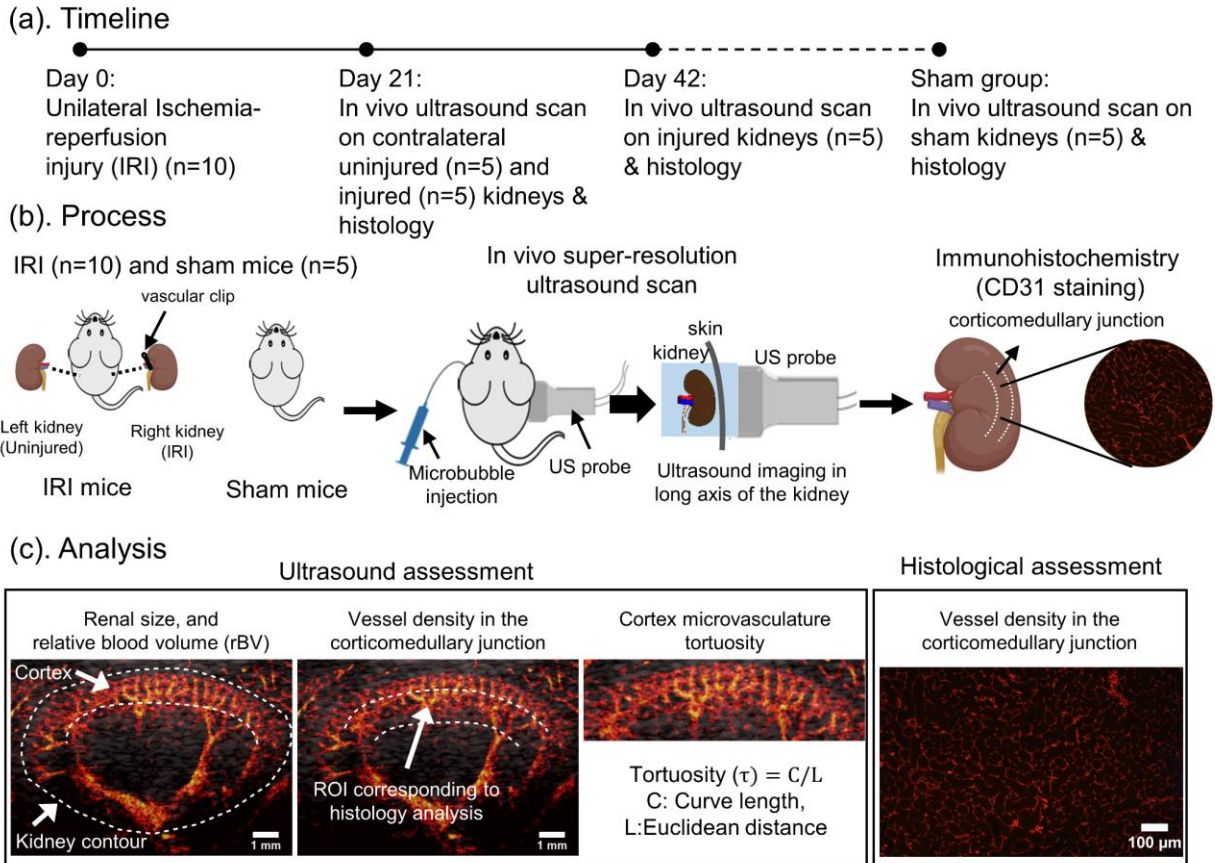


**Figure 18** Experimental design for in vivo ultrasound super-resolution imaging on mouse acute kidney injury model. (a) Timeline of the experiment (b) Ischemia-reperfusion injury (IRI) is performed on the right kidney to induce the acute kidney injury (AKI). The sham, contralateral, and injured kidneys at 21-days and injured kidneys at 42-days post injury (n=5 for each group) were scanned by ultrasound in long axis for ultrasound super-resolution (USR) images. The kidneys were excised immediately after the scan for fibrosis analysis and immunohistochemistry with CD31 staining focusing on renal vasculature around the corticomedullary junction. (c) From the reconstructed USR images of the kidneys, kidney changes including area, vessel density, and microvasculature tortuosity were assessed.

### 5.2.3 Histology and Immunohistochemistry

Formalin-fixed, paraffin-embedded kidney tissue was sectioned at 3  $\mu\text{m}$  thickness in the long axis of the kidney at the midsagittal plane, corresponding to the plane of SRU imaging. Staining with Masson's Trichrome and picrosirius red were performed according to manufacturer's instructions (Thermo Fisher, Pittsburgh, PA). For fibrosis quantification, at least 10 high powered (40X) images were taken in the corticomedullary junction for each slide after Masson's trichrome staining. Large vessels were avoided. A 10x13 grid was then overlaid upon each image and the grid intersections containing fibrosis were counted compared to total number of intersections. The counter was blinded to identifier and treatment group of the sample being viewed. For immunohistochemistry, sections were deparaffinized and hydrated before inactivation of endogenous peroxidases with 3% hydrogen peroxide in methanol. After blocking, slides were incubated in primary antibody against CD31 (#77699S, Cell Signaling Technology, Danvers, MA) overnight. Fluorescent anti-rabbit secondary antibody (Jackson ImmunoResearch, West Grove PA) was then added for 2 hours prior to imaging on an immunofluorescence microscope. For CD31 immunostaining, images were photographed in a blinded fashion for each mouse in the study. At least 5 low-power (10X) images were obtained which cumulatively covered the entirety of the corticomedullary junction on a mid-sagittal section of the kidney. Quantitation was performed using the percent area function of Image J (NIH, Bethesda MD) using a common threshold for all images.

After RNA isolation with TRIzol reagent (Thermo Fisher, Pittsburgh PA) and reverse transcriptase reaction, the cDNA was run in a qRT-PCR reaction with SYBR green in a CFX Connect (Biorad, Hercules CA). Forward and reverse primer sequences were CCACGTCAGAGAGCAACATCA and TCATCTCTCCTATGTGCTGGCTTT for *VEGF*, AGGCAACAGTGGTTCTCCTG and GACCTCGTGCTCCAGTTAGC for *collagen III*, and CAGCTGAGAGGGAAATCGTG and CGTTGCCAATAGTGATGACC for  $\beta$ -actin.

#### **5.2.4 SRU Imaging Signal Processing Procedure**

Figure 19 (a) shows the block diagram of the SRU signal processing procedure. The post-processing algorithm of SRU in this study is similar to that described in 4.2.3, except the rigid body motion compensation process that will be described in detail in the following section. The representative reconstructed images after the main signal processing steps are shown in Figure 19(b), 19(c), 19(d), and 14(e).

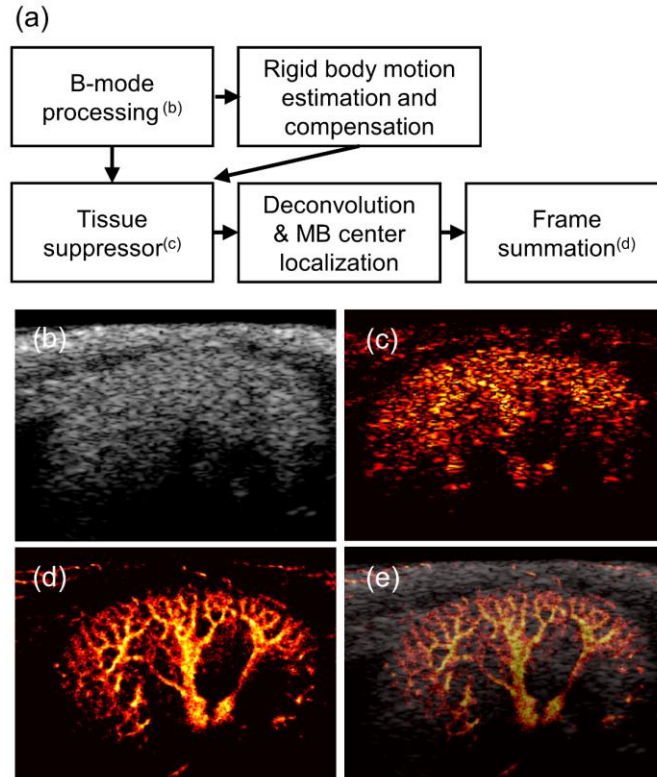


**Figure 19 SRU signal processing and image reconstruction procedure. (a) Signal processing block diagram. The raw radio frequency channel data was acquired by multi-angle ultrasound plane wave imaging and went through B-mode processing with delay-and-sum beamforming algorithm and quadrature demodulator. After estimating and compensating the rigid body motion of the kidney caused by respiration, a spatio-temporal eigen-based decomposition clutter filter was applied to suppress the signals from tissues and extract the signals from the microbubbles. RL deconvolution method was used to localize the center of each microbubble. Final SRU image was reconstructed by summing up 300 frames of the localized images. (b) Representative image of mouse kidney after B-mode processing. (c) Representative image after applying tissue suppressor. (d) Representative SRU image after microbubble center localization and frame summation. (e) Final image by overlaying the B-mode and SRU images of the mouse kidney.**

### **5.2.5 Rigid Body Motion Estimation and Compensation**

The central concept of super-resolution ultrasound imaging technique is to localize the center of the flowing microbubbles based on the system PSF in each image frame after suppressing the stationary signals coming from tissues. Then the final microvasculature image is reconstructed by summation of the localized microbubbles from these frames. Therefore, the vessel size and shape are mainly determined by the temporal distribution of the flowing microbubbles within the blood vessels. If the respiratory motion occurs, the distribution of the microbubbles will change as the vessels displace with the respiratory motion, which will lead to the blurriness of the images and, therefore, the overestimation of the vessel size. Figure 20 shows the conceptual schematic diagram of the blurred vessel image due to the respiratory motion artifact and its correction during the inhalation phase. Thus, it is expected that the spatial resolution and the signal-to-noise ratio (SNR) can be improved by correcting the locations of microbubbles over the data set with the breathing motion.

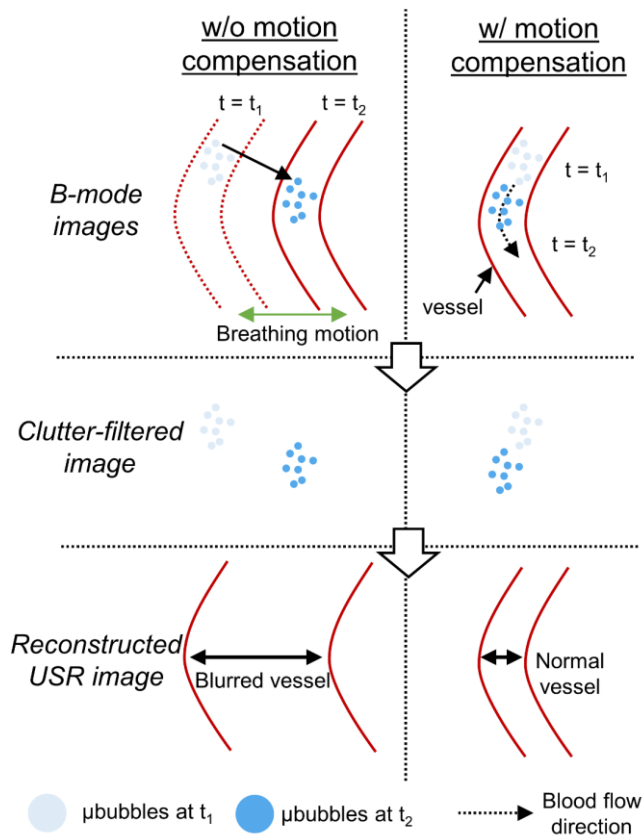


**Figure 20** The schematic diagram of the motion artifacts due to respiration.

Figure 21 depicts the details of signal processing procedure of the rigid body motion compensation algorithm, which was included in the SRU algorithm as shown in Figure 19. First, Pearson's correlation coefficient between the first frame, as the reference frame, and the current frame was calculated to determine if any motion was involved. Based on our observations, it is determined that the motion can be ignored if the correlation coefficient is larger than or equal to 0.9975. The respiratory motion compensation technique was applied only to the frames that were determined to be decorrelated with the correlation coefficient smaller than 0.9975. Then, the static tissues in the images were detected and masked to exclude from the subsequent motion estimation process for optimizing the motion estimation performance. The images were divided into the small

blocks of 2 mm by 2 mm, and the correlation coefficients of the blocks between each frame and the reference frame were calculated. The blocks with the correlation coefficient larger than 0.9975 were considered as static tissues. Finally, the rigid body motion of the moving organ can be estimated by using a 2-D correlation or any traditional block matching algorithms. We arguably assumed that the respiratory motion is translational motion with no significant tissue deformation. Therefore the resulting displacement is globally estimated, allowing for the phase information of I/Q signal unchanged. Here, we chose the three-step search algorithm, which is one of the most traditional fast block matching algorithms. This algorithm may not provide the best accuracy but still shows a near-optimal performance with the advantage of low computational complexity [109], [110]. In the first phase, it searches for the area having the least cost value at neighboring eight points with the step size S from the center of the searching block: (+S, +S), (+S, 0), (+S, -S), (0, -S), (-S, -S), (-S, 0), (-S, +S), (0, +S). Here, the step size S was chosen as 7 mm. The mean absolute difference was utilized as a cost function to find the best matching points,

$$\text{mean absolute difference} = \frac{1}{N} \sum_{i=1}^N \sum_{j=1}^N |C_{ij} - R_{ij}|, \quad (5-1)$$

where N is searching block size,  $C_{ij}$  is the IQ data of the current chosen block, and  $R_{ij}$  is the IQ data of the reference block. The chosen point was to set the new origin of the searching block, and then the iterative searching process continues with half of the step size in the previous phase until the current step size becomes 1 pixel. In this way, the motion in the current frame was estimated, and the moving organ was shifted back based on the estimated motion vector. Thus, the rigid body motion of the organ in each frame was compensated toward the reference frame.

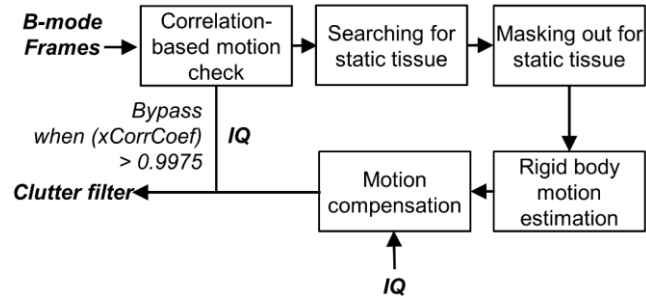


Figure 21 Signal processing pipeline of the rigid body motion compensation.

### 5.2.6 SRU Image Analysis and Quantitative Assessment of the Microvasculature

The reconstructed 2-D cross-sectional overlaid SRU and B-mode images of the long-axis mouse kidney was used for quantifying changes in kidney size, cortex thickness, rBV, vessel density at the corticomedullary junction, and tortuosity of the cortex microvasculature (Figure 18c). The contour of the kidney was manually selected according to the B-mode layer, by which the long axis area of the kidney was determined. In the SRU layer, the vessels were identified by threshold-based segmentation. The cortex thickness was determined by the average distance between the outer boundary of the kidney and the corticomedullary junction according to the vasculature structure depicted in the SRU layer. rBV was calculated as the ratio of vessel area inside the kidney to the area of the entire kidney. The vessel density in the area of corticomedullary junction was calculated as the ratio of vessel area inside the region of interest (ROI), which was selected manually according to the anatomical structure in the SRU image, to the total area of the ROI. The analysis above was performed in MATLAB (Mathworks, Natick, MA). The tortuosity of the cortical microvasculature was assessed using ImageJ (NIH, Bethesda, MD), with plugin Skeletonize3D [111] and AnalyzeSkeleton [112], [113].

### **5.2.7 Statistical Analysis**

All the quantitative results were presented as mean  $\pm$  standard error. To evaluate the statistical significance, all the data among the four groups (sham, contralateral, 21 days post-injury, 42 days post-injury, n = 5 each) were compared using one-way analysis of variance (ANOVA) with post-hoc Tukey's Honestly Significant Difference (HSD) Test. The correlation between US and histology quantification of the vessel density in ROI was performed using Pearson's correlation analysis. The value of  $P < 0.05$  was considered statistically significant. All the statistical analysis and plots are generated using GraphPad Prism 5.0 (San Diego, CA).

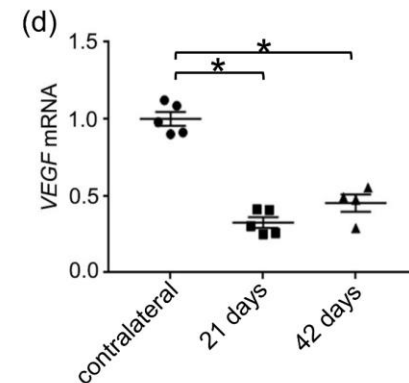
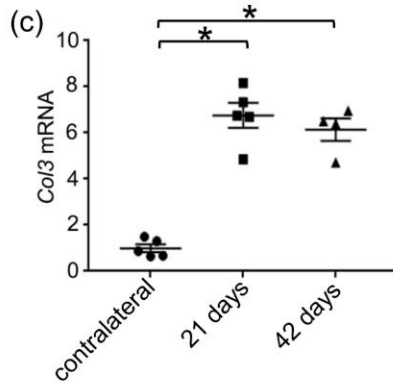
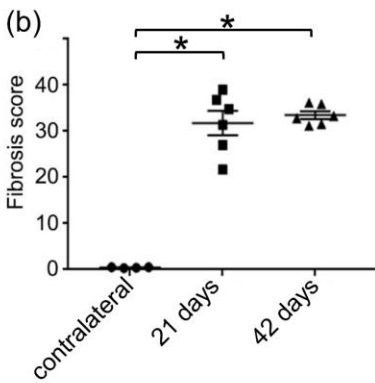
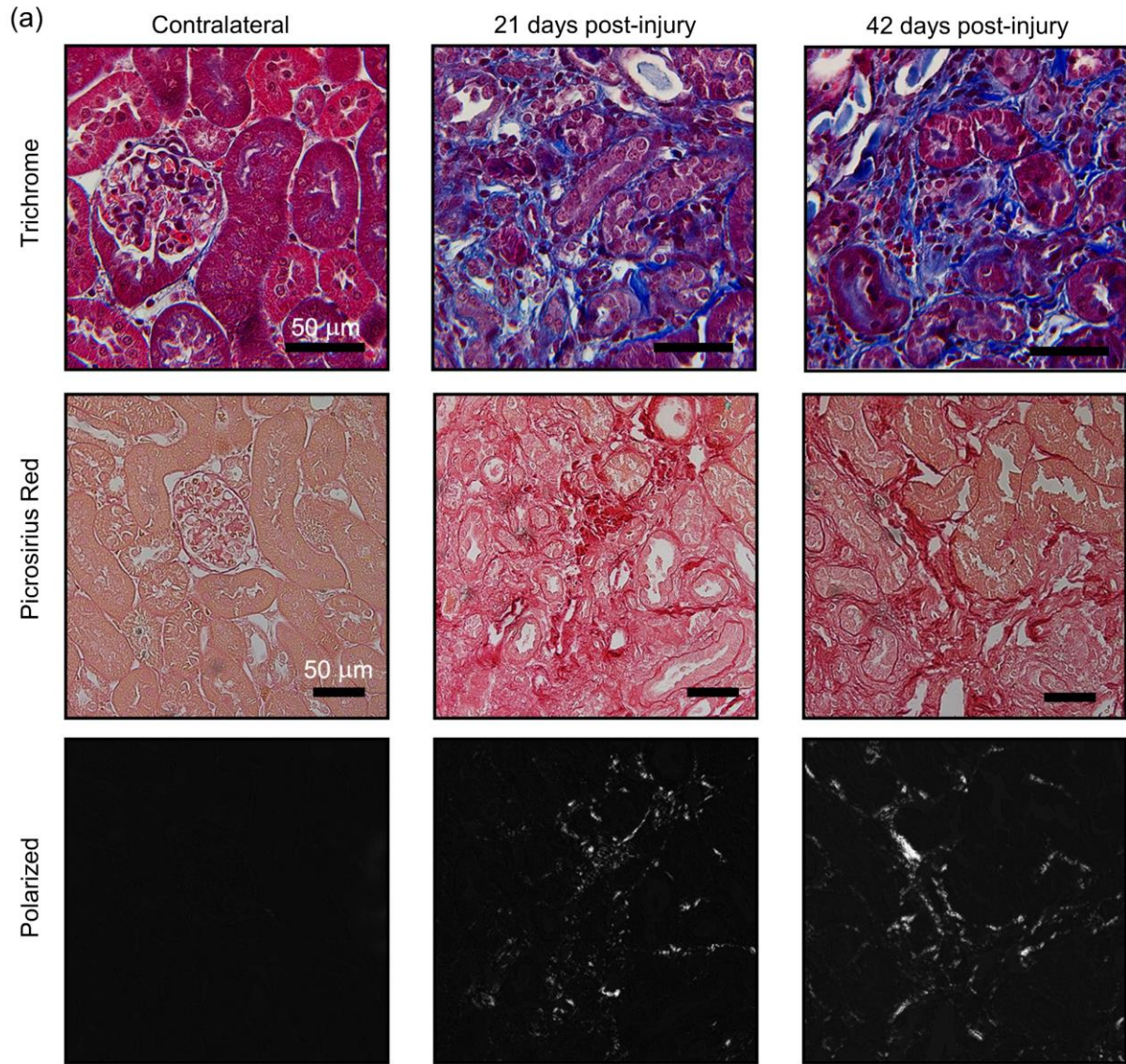
## **5.3 Results**

Figure 18 presents the experimental design of this study including groups, experimental protocol and analysis.

### **5.3.1 IRI Leads to the Development of Renal Fibrosis**

Kidneys subjected to IRI in our mouse model exhibited extensive interstitial fibrosis at both 21 and 42 days after injury. Masson's Trichrome stain demonstrated large areas of fibrosis only in affected kidneys. Picosirius red staining confirmed these results, and when these slides were viewed under polarized light, collagen fibers specifically exhibited birefringence, confirming deposition of extracellular matrix (Figure 22a). Although there was a significant increase in fibrosis in the IRI kidneys over contralateral kidneys, we did not find any differences between the

21 day and 42 day IRI kidneys (Figure 22b). This suggests that fibrotic development, as assessed by our methods, reaches a plateau in our injury model, with timing that is in agreement with previously published reports [88]. We confirmed these results with quantitative real-time PCR showing that collagen mRNA transcripts are enhanced to similar levels in the 21 and 42 day kidneys (Figure 22c). Consistent with previous reports [114], [115], we found that there was a decrease in vascular endothelial growth factor (VEGF) mRNA in all injured kidneys (Figure 22d).



**Figure 22 IRI leads to renal fibrosis. Mice were subjected to unilateral IRI and both the affected and contralateral kidneys were recovered at either 21 or 42 days after injury. (a) Fibrosis was detected with Masson's Trichrome stain (blue staining) as well as picrosirius red stain (dark red). When the picrosirius slides were viewed under polarized light, birefringence denotes specific staining for collagens. (b) Fibrosis scoring of kidneys. (c-d) mRNA levels of collagen (Col3) are dramatically elevated in all injured kidneys compared to the contralateral kidneys. mRNA levels of VEGF are dramatically decreased in all injured kidneys. Data are expressed as mean  $\pm$  standard error. \*  $P < 0.0001$  compared to contralateral kidneys, no differences were found between the 21 and 42 day injured kidneys.**

### **5.3.2 In Vivo SRU Imaging Enables a Qualitative Assessment of the Overall Changes of the Mouse Kidney with IRI**

Figure 23 depicts the overlaid B-mode and SRU images of sham kidneys (Column A, n = 5), contralateral uninjured kidneys (Column B, n=5), and the injured kidneys at 21 days (Column C, n = 5) and 42 days (Column D, n = 5) after IRI. The 2-D cross-sectional US scan was aimed at the center plane of the kidneys in the long axis. The anatomical contour of the kidneys was shown from the B-mode layer in gray-scale in the background, and the vascular tree was identified from the overlaid SRU images in hot color scale with high spatial resolution resolving microvessels down to 32  $\mu\text{m}$ . The major renal vessel branches, aorta, cortex, medulla, and dorsal skin were marked by white arrows in the image of the injured kidney from mouse number 6. Although there was some interanimal variability, an overall decrease in kidney size and cortical thickness after IRI was observed. Of note, obvious rarefaction of the renal vasculature was consistently identified in the injured kidneys, compared to sham and contralateral.

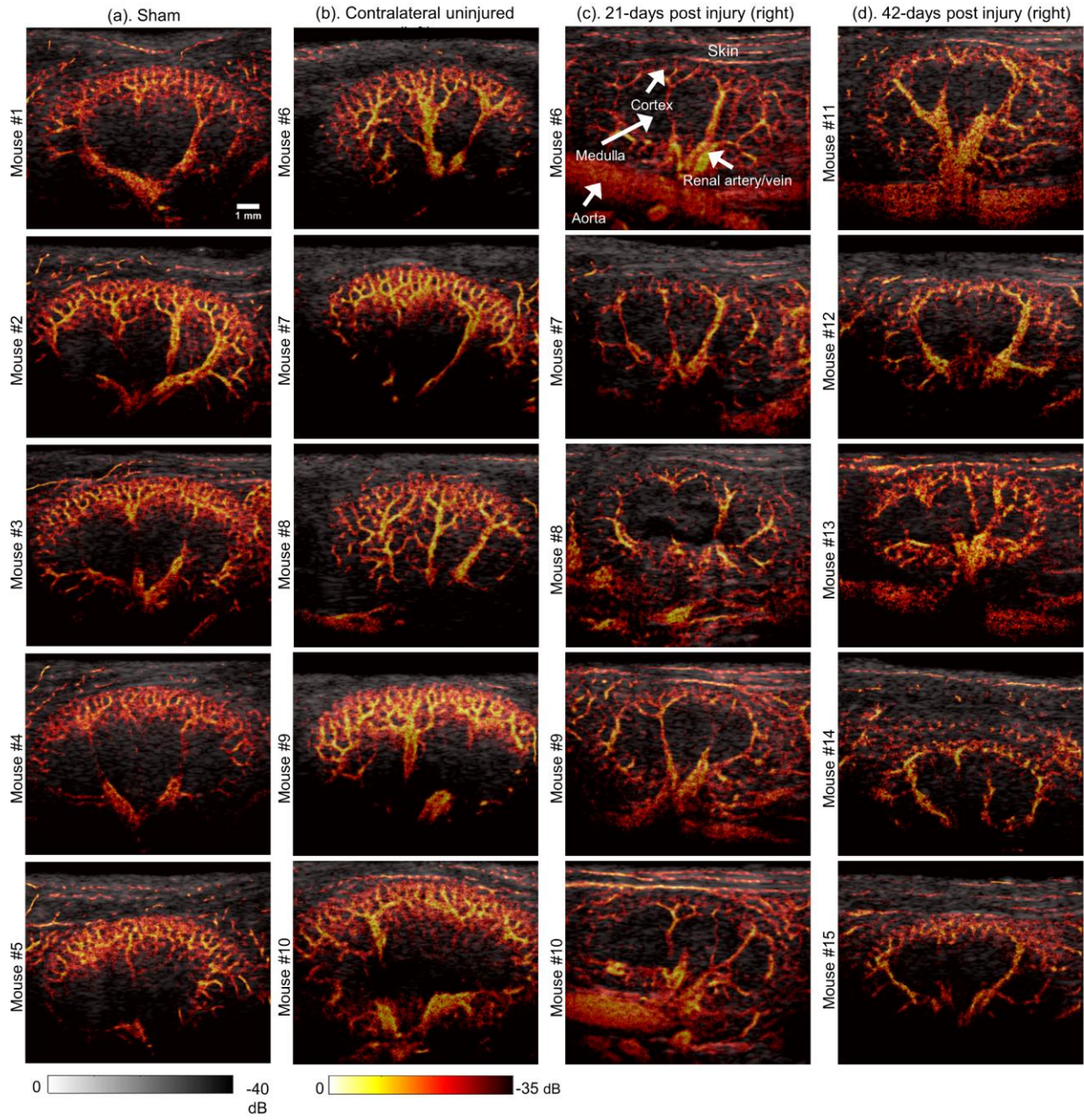


**Figure 23 Overlaid B-mode and super-resolution ultrasound (B-SRU) images for sham kidneys, contralateral kidneys, injured kidneys at 21-days post injury, and injured kidneys at 42-days post injury. Column (a) shows the SRU images of the five sham kidneys. Column (b) shows the contralateral kidneys. Column (c) and column D show the SRU images of injured kidney scanned at 21 days and 42 days after injury, respectively. To provide an anatomical landmark, the major renal vessel branches, aorta, cortex, medulla, and dorsal skin were marked by white arrows in the image of the injured kidney from the mouse number 6. Overall decrease in size and increase in vasculature rarefaction were observed over time.**

### **5.3.3 In Vivo SRU Imaging Enables a Quantitative Assessment of the Changes in Overall Morphology and Renal Perfusion of the Mouse Kidney with IRI**

Figure 24(a) plots the average of the cross-sectional area in the long axis of the kidney measured from US B-mode image, which demonstrated a significant decrease in size in injured kidneys of 21 days ( $37.54 \pm 1.55 \text{ mm}^2$ ) and 42 days ( $35.67 \pm 2.41 \text{ mm}^2$ ) compared to sham ( $49.20 \pm 1.58 \text{ mm}^2$ ). This agreed with the measured kidney weights (Figure 24b), which decreased from  $160.50 \pm 4.83 \text{ g}$  (sham) to  $96.94 \pm 6.22 \text{ g}$  (21 days) and  $80.70 \pm 6.14 \text{ g}$  (42 days). As expected, the weight of the contralateral kidney ( $197.70 \pm 8.08 \text{ g}$ ) was increased compared to sham, consistent with compensatory hypertrophy. However, this change was too subtle to observe in cross-sectional ultrasound imaging. The areas of the cortex and medulla were manually identified according to the structural B-mode and overlaid vasculature images. For sham, contralateral, 21 days and 42 days post-injury kidneys, the average thickness of the cortex was estimated to be  $1.76 \pm 0.03 \text{ mm}$ ,  $1.88 \pm 0.08 \text{ mm}$ ,  $1.23 \pm 0.04 \text{ mm}$  and  $1.10 \pm 0.08 \text{ mm}$  respectively (Figure 24c), supporting the trend of continuous reduction in the kidney size with the progression of kidney injury. There was significant decrease of the cortical thickness by comparing 21 days ( $P < 0.001$ ) and 42 days ( $P < 0.001$ ) post injury kidneys to either sham or contralateral. No significant difference was found

between 21 days and 42 days post injury. The vessel densities in different regions of interest, including the entire kidney, cortex and corticomedullary junction of the kidneys were quantified from the SRU images. The rBV, which is defined as the percentage of the blood volume to the total organ volume [88], [116], was estimated at  $34.66 \pm 1.99\%$  in sham,  $35.85 \pm 1.38\%$  in contralateral,  $22.35 \pm 1.38\%$  in 21 days post injury, and  $26.30 \pm 1.92\%$  in 42 days post injury (Figure 24d). By statistical analysis, a significant decrease between sham and 21 days ( $P < 0.001$ ), and between sham and 42 days ( $P < 0.05$ ) was demonstrated. The vessel density in the cortex was measured to be  $64.44 \pm 1.80\%$  in sham,  $66.96 \pm 2.69\%$  in contralateral,  $39.77 \pm 2.69\%$  in 21 days post injury, and  $46.47 \pm 2.47\%$  in 42 days post injury (Figure 24e). A significant decrease between sham and 21 days ( $P < 0.001$ ), and between sham and 42 days ( $P < 0.001$ ) were found. Compared to 21 days, a slight nonsignificant increase of rBV and vessel density in the cortex at 42 days post injury was noted. The vessel density in the corticomedullary junction of the sham, contralateral, and in the 21 and 42 days injured kidneys were estimated to be  $47.14 \pm 2.41\%$ ,  $49.59 \pm 2.42\%$ ,  $26.17 \pm 1.28\%$  and  $27.60 \pm 1.37\%$ , respectively (Figure 24f). These densities were obtained by calculating the area fraction of the segmented vessels in the region of interest in SRU images of the kidneys. The vessel density in the corticomedullary junction of 21 and 42 days post-injury kidneys were significantly decreased compared to sham ( $P < 0.001$ ) and contralateral ( $P < 0.001$ ), but a significant difference was not found between the two injury groups. SRU demonstrated a small nonsignificant increase in vessel density between the sham and contralateral groups. These quantitative assessments support prior findings of perfusion impairment chronically after a single episode of AKI [88], [90].

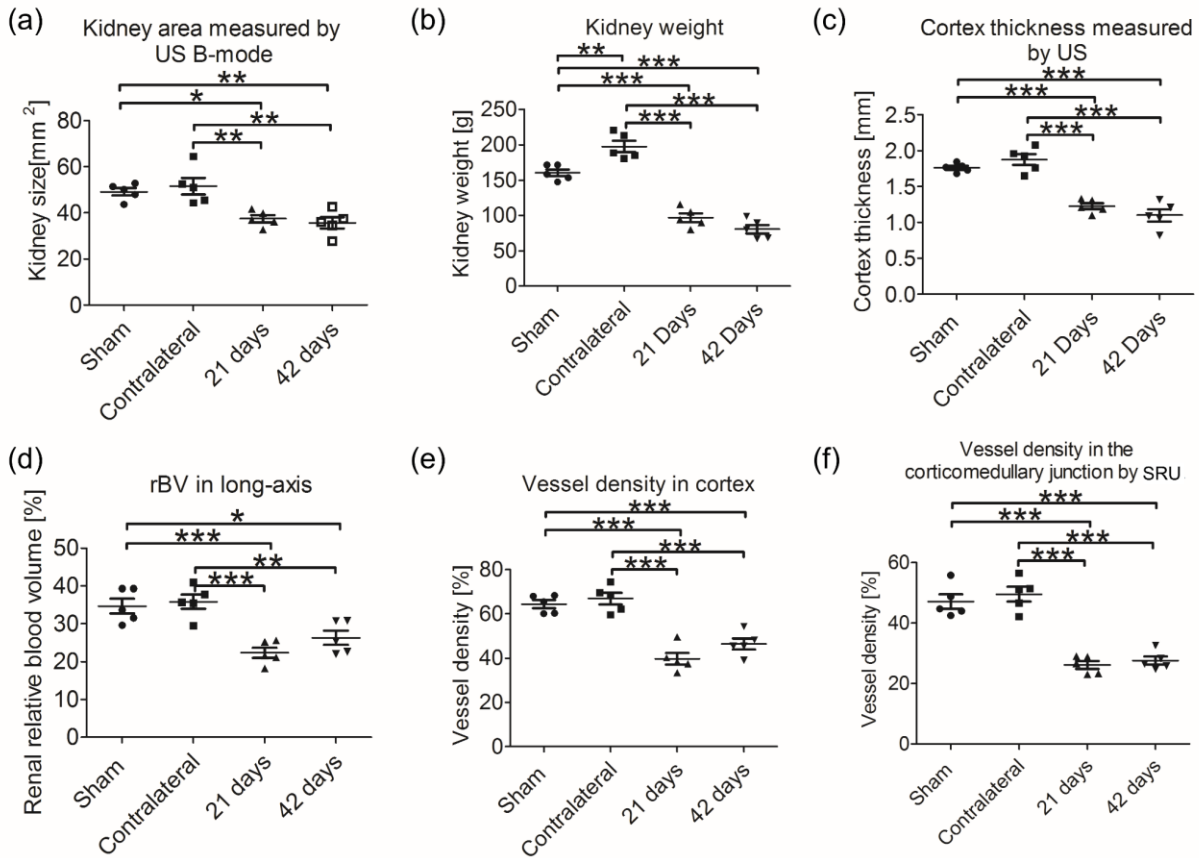


**Figure 24** Quantitative assessment of the changes in overall morphology and renal blood volume of sham, contralateral, and IRI kidneys. (a) Kidney cross-sectional area measured from the long-axis US B-mode images. Cross-sectional areas of the sham, contralateral, 21 days post injury and 42 days post injury kidneys were  $49.20 \pm 1.58 \text{ mm}^2$ ,  $51.61 \pm 3.57 \text{ mm}^2$ ,  $37.54 \pm 1.55 \text{ mm}^2$ ,  $35.67 \pm 2.414 \text{ mm}^2$ . A significant decrease in kidney area after IRI was observed by ultrasound measurement. (b) Weight of the sham ( $160.50 \pm 4.83 \text{ g}$ ), contralateral ( $197.70 \pm 8.08 \text{ g}$ ), and injured kidneys (21 days:  $96.94 \pm 6.22 \text{ g}$ , 42days:  $80.70 \pm 6.14 \text{ g}$ ). Significant reduction in weight was found, which supports the size decrease measured by US. (c) Cortex thickness of the kidneys measured from the US images. Significant decrease of the cortex thickness of the injured kidneys (21days:  $1.23 \pm 0.04 \text{ mm}$ , 42 days:  $1.10 \pm 0.08 \text{ mm}$ ) compared to sham ( $1.76 \pm 0.03 \text{ mm}$ ) and contralateral ( $1.88 \pm 0.08 \text{ mm}$ ) was found. (d) US estimation of relative blood volume (rBV). The average rBV of the sham kidneys, contralateral kidneys, and IRI kidneys at 21 days and 42 days were  $34.66\% \pm 1.99\%$ ,  $35.85\% \pm 1.88\%$ ,  $22.35\% \pm 1.38\%$ , and  $26.30\% \pm 1.92\%$ , respectively. Significant decrease of rBV on IRI kidney was observed. (e) Vessel density in the cortex measured by US. A significant reduction in 21 days

( $39.77 \pm 2.69\%$ ) and 42 days ( $46.47 \pm 2.47\%$ ) post-injury kidneys compared to sham ( $64.44 \pm 1.80\%$ ) and contralateral ( $66.96 \pm 2.66\%$ ) kidneys was found. (f) Vessel density in the corticomedullary junction measured by US. A significant decrease in 21 days ( $26.17 \pm 1.28\%$ ) and 42 days ( $27.60 \pm 1.37\%$ ) compared to sham ( $47.14 \pm 2.41\%$ ) and contralateral ( $49.59 \pm 2.42\%$ ) was found. (n=5, ANOVA with post-hoc Tukey HSD test, \*P<0.05; \*\*P<0.01; \*\*\*P<0.001.)

### 5.3.4 In Vivo SRU Imaging Correlates with Histology in Vessel Density Estimation

Figure 25(a) shows CD31 immunostaining of the corticomedullary junction area of the sham, contralateral, and IRI kidneys at 21 and 42 days, a region that is particularly susceptible to IRI 7. The mean vessel density in the corticomedullary junction from each group, determined as the fractional area of staining from a midsagittal slice of the kidney, was  $12.14 \pm 0.75\%$  for sham kidneys,  $15.02 \pm 0.47\%$  for contralateral,  $7.56 \pm 0.22\%$  for IRI kidneys 21 days post injury, and  $8.82 \pm 0.73\%$  for IRI kidneys 42 days post injury (Figure 25b). Significant reduction of vessel density through histologic assessment was demonstrated between sham and 21 days ( $P < 0.001$ ), and between sham and 42 days ( $P < 0.01$ ). The significant reduction was also found by comparing contralateral to 21 days ( $P < 0.001$ ) and 42 days ( $P < 0.001$ ). The statistical significance by comparing injury groups to sham or contralateral agrees with the US assessment in the same area shown in Figure 24(f). Moreover, the vessel density of contralateral was shown to be significantly higher than the sham group ( $P < 0.05$ ) by histology, which suggests the compensatory increase in blood flow or remodeling induced by the injury on the other side of the kidney. Figure 25(c) compares the histology with US assessment of the vessel density in the corticomedullary junction on a total of 20 kidneys over four different groups. There was a significant correlation between vessel density values determined by histology and SRU in the corticomedullary junction ( $P < 0.001$ ,  $R^2 = 0.77$ ), supporting the accuracy of the microvascular density assessment by SRU imaging.

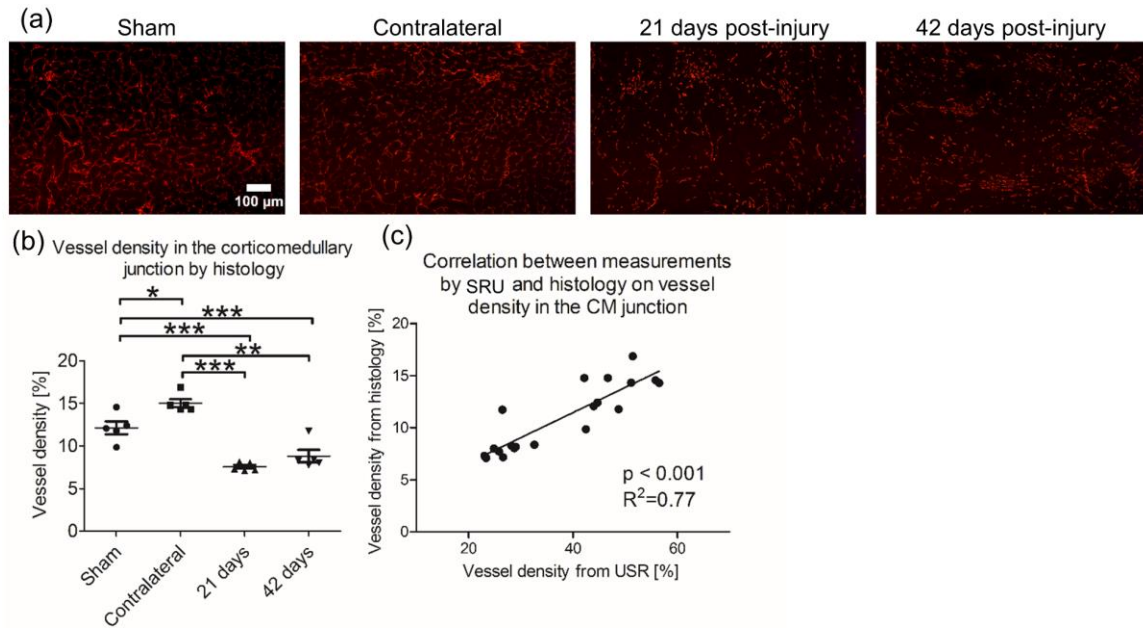


**Figure 25 Vessel density in the corticomedullary junction by histology and correlation with US imaging. (a) Representative CD31 staining of the sham, contralateral, and IRI kidneys. (b) Vessel density measured as positively stained area fraction of the vessels in corticomedullary junction. (Sham:  $12.14 \pm 0.75\%$ , contralateral:  $15.02 \pm 0.47\%$ , 21 days:  $7.56 \pm 0.22\%$ , 42 days:  $8.82 \pm 0.73\%$ ) Injured kidneys exhibited a decrease of vessel density in the ROI compared either sham or contralateral kidney. (n=5, ANOVA with post-hoc Tukey HSD test, \*P<0.05; \*\*P<0.01; \*\*\*P<0.001.) (c) Significant correlation between the histology and SRU measurement of the vessel density in the corticomedullary junction was found (P value < 0.001, correlation coefficient: 0.77). (n=20, Pearson's correlation analysis)**

### 5.3.5 In Vivo SRU Imaging Enables a Quantitative Assessment of the Tortuosity Changes in the Cortical Vasculature

The tortuosity of the cortical microvasculature, which is defined as a ratio of the vessel length between two nearby branching points and the linear distance between those, was also assessed for each kidney from the four groups. Figure 26(a) shows representative SRU images of

the cortical microvasculature from the sham kidney and the kidney at 42 days post-injury. It is observed that the more terminal vessels are overall more tortuous and aggregated at 42 days post-injury, while most vessels have straight branches in the sham group. Figure 26(b) plots the average vessel tortuosity of the sham kidneys ( $1.129 \pm 0.016$ ), contralateral kidneys ( $1.143 \pm 0.008$ ), 21 days post-injury kidneys ( $1.146 \pm 0.017$ ) and 42 days post-injury kidneys ( $1.194 \pm 0.012$ ). A significant increase of the tortuosity in 42 days post-injury kidneys was found compared to the sham group ( $P < 0.05$ ).

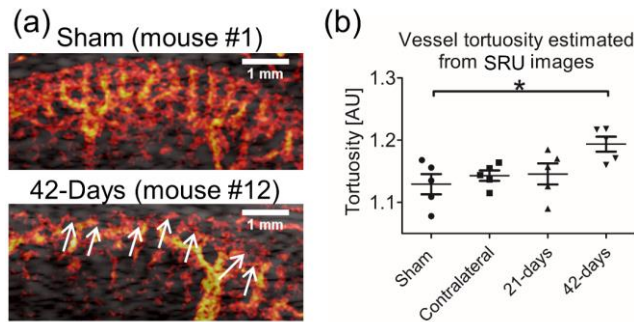


**Figure 26 Tortuosity of the control kidney and IRI kidney. (a) Representative SRU images of the cortical vessels from control and 42-days post-injury kidneys are shown. White arrows indicate the curved and clamped vessels from 42-days post-injury kidney. (b) Significant increase of cortical microvasculature tortuosity is shown in the kidney at 42-days post injury. (n=5, ANOVA with post-hoc Tukey HSD test, \*P<0.05.)**

## 5.4 Discussion

This study shows that SRU imaging is able to visualize renal microvessels with very high spatial resolution. The high quality SRU images enable a quantitative assessment of the kidney vascular structure in different aspects including rBV, microvascular density and tortuosity during AKI- to-CKD progression, all in a noninvasive manner. The results are in agreement with the known phenomenon of vascular rarefaction in established mouse kidney IRI models [71], [77], [79], [88]. The vessel density measured by SRU correlates well with the histologic measurements, demonstrating the robustness of this technology.

The unilateral IRI mouse model adopted for this study is a well-established model of AKI-to-CKD progression [108]. In this model, the kidney exhibits a reduction in size over time, along with perfusion impairment and microvascular rarefaction. As expected, we demonstrated that this is associated with the development of extensive renal fibrosis, as well as a reduction in VEGF which would contribute to vessel rarefaction [117]. During the US scan, in order to have consistent comparisons, all mouse kidneys were imaged at the center plane in the long axis with same settings of the US system, and vessel segmentation threshold was applied at -25dB for all the images. The results show that SRU imaging is able to visualize renal microvessels with very high spatial resolution. The changes in kidney size, cortex thickness, rBV, microvascular rarefaction, and tortuosity were successfully quantified from high quality SRU images and demonstrate progressive pathologic changes over time. The close correlation ( $R^2 = 0.77$ ) between the SRU and histology validates the feasibility and accuracy of SRU for renal vasculature assessment.

The absolute values of the rBV and vessel density from SRU were generally higher than those from the histology readings. The discrepancy could be mainly attributed to the finite transducer elevational beamwidth (or imaging slice thickness) that is around 1.6mm. The US echo signals that originate slightly off-center from the imaging plane but within the elevational beamwidth of the transducer will still be recognized by the imaging system and contribute to the signal intensity in the final reconstructed images [55]–[58]. Thus, the rBV and vessel density can be overestimated by dividing the volumetric vascular signals within the imaging slice thickness by the 2-D area. In addition, a relatively low SNR in some areas of the kidney may have affected the deconvolution process during image reconstruction [64]–[66], resulting in the overestimation of the vessel population. The relatively low SNR may also contribute to the lower sensitivity of SRU compared to histology, especially in the area with high vessel density that has already overcrowded microbubbles during imaging. Therefore, while kidney weight and vessel density measured with histology were significantly higher in the contralateral compared to sham kidneys (consistent with reactive changes during unilateral IRI), SRU could not detect this difference with significance. The microvessels inside the mouse renal cortex are reported to be as small as several microns. Although the spatial resolution of SRU is greatly improved compared to conventional US imaging, small arterioles and capillaries as well as venules below the spatial resolution of SRU imaging cannot be identified as individual vessels. Thus, the single vessel shown in the SRU images could actually represent one or several adjacent smaller vessels under 30 microns. This also might have contributed to the slight overestimation in rBV and vessel density measurement. Although these minor discrepancies exist, it does not affect our major findings in the correlation between SRU and CD31 stain, and the statistical difference between the injured and sham groups. Our overall immunohistochemical staining and measurements of vascularity show a similar trend to prior

published data [88]. While our sham kidneys have a different percentage area than the prior published report, this is likely due to differences in thresholding used in our study. However, the same threshold was utilized for every image for consistency in analysis.

According to our tortuosity analysis, the microvascular tortuosity was significantly increased at the late time point of 42 days after IRI, which is in concordance with *ex-vivo*  $\mu$ CT results in an earlier study [88]. This alteration could be a useful index for predicting disease progression. It should also be noted that microvessels with high tortuosity will aggregate together in a finite area of the kidney. These individual vessels will be more difficult to separate at the later stages of injury, which may result in the overestimation of vessel density. This could be the reason for the slight increase in cortical vessel density and rBV at 42 days compared to 21 days. It is also possible that increases in rBV and vessel density, as a ratio of percentage of blood volume to area, are due to the overall loss of kidney and cortical size at the late time point of our study. This trend of slight increase of vessel density at 42 days was also found by the histological assessment.

There are some limitations of this study. Since we aimed in this study to first validate the feasibility of SRU technology in this study, the kidneys were harvested for histology after each US scan. In the future, a longitudinal monitoring of the kidney by SRU would be helpful to minimize interanimal variations and investigate the effects of drug interventions during the disease. In addition, the accumulation of the dense microbubbles in cortical blood vessels would block ultrasound energy from deeper transmission into the medulla, leading to lower intensity of medullary blood vessels and discontinuity in the SRU images. This is especially prevalent in sham and contralateral kidneys that have higher cortical vessel density. A carefully selected microbubble concentration would be needed to compromise the image quality between the cortex and medulla. Moreover, there is still room for further improving the performance of SRU in the future, such as

3-D US scan to achieve volumetric information, using US probe with higher frequency to enhance the spatial resolution, and advanced signal processing techniques to enhance the SNR and sensitivity of SRU. Finally, the reduction in kidney size over time may have affected our quantification of vessel density and rBV, but this would have actually led to an overestimation since these measurements were adjusted to total tissue area.

In previous studies by other groups,  $\mu$ CT [88], [89] and CEU [90] were proposed as diagnostic methods for noninvasively evaluating progressive kidney disease. In the CEU study [90], renal perfusion impairment was detected and quantified noninvasively. The kidney from IRI mouse model was scanned in the long axis and the renal cortical perfusion was measured according to video intensity, similar to our study design. However, the precise microvascular structure within the kidney, especially in the area of the medulla and cortex, cannot be visualized clearly by CEU due to its limited spatial resolution and inability to identify ROI with accuracy and consistency. For the same reasons, CEU cannot provide detailed information on vessel tortuosity. In the  $\mu$ CT studies [88], [89], spatial resolution down to 20  $\mu$ m voxel size were achieved *in vivo* allowing the quantification of blood volume. However, the *in vivo*  $\mu$ CT approach still suffers from radiation and contrast toxicity issues, which hinders serial monitoring in practical applications. SRU for imaging renal microvascular changes has been studied before in a rat IRI model [52]. However, that study was performed on limited animal samples and without histological and statistical support. In this study, we used increased number of animals and groups in order to determine statistical significance. We have also validated our technology with histologic analysis. Compared to other previous imaging methods, SRU imaging provides competitive performance for noninvasive visualization and quantification of vessel characteristics. Since it is also safe and affordable, SRU is a promising technology to aid in the monitoring and potential prognostication

of kidney disease. For instance, in patients who sustain AKI, an assessment of the microvasculature could predict the future development of CKD. Microvascular assessment could also aid in the understanding of the vascular changes occurring over time in humans with AKI or CKD. Another potential application of SRU imaging would be evaluating renal transplants soon after implantation into recipients since all renal transplants experience a degree of AKI. The evaluation of their microvasculature might be able to predict which kidneys will do well long term and which will not. It should be noted that US microbubbles are widely used in clinics, and have a good safety profile [104]–[107]. Translating this technology for human use requires adaptation of the technique for the curved array ultrasound probe commonly used in clinical abdominal imaging which provides a deeper and wider field of view. While the algorithms used in this study are being continually optimized and adapted to the curved probe, it is notable that the technique described exactly as in this manuscript can be (and has been) applied with success in humans. In fact, kidney imaging in humans is in many ways easier since the size of the kidneys and their blood vessels are much larger than in mice. Studies on more human subjects including healthy volunteers and CKD patients are ongoing for translating this SRU technology to human clinical use.

## 5.5 Conclusions

In conclusion, we show that SRU imaging is able to identify renal microvessels with unprecedented high spatial resolution up to 32  $\mu\text{m}$  *in vivo* and allow for quantification of the changes in kidney morphology and vasculature, including size, rBV, vessel density and tortuosity. This was demonstrated in a clinically relevant rodent model of AKI-to-CKD progression. A relatively high correlation between SRU and traditional immunohistochemistry of vessel density

was found with  $R^2 = 0.76$  which validates the accuracy of the quantitative assessment by SRU. Therefore, SRU has a great potential to provide key clinical data to aid in the care of patients with progressive kidney disease.

## **6.0 SRU Imaging of Human Kidney Imaging Using Clinical Curved Linear Array Probe**

### **6.1 Introduction**

In the previous chapter, we demonstrated the capability of SRU imaging for noninvasive and quantitative evaluation of the microvascular changes after initial AKI using the mouse model. For translating the SRU technology into human use in clinics, the SRU algorithm that is adapted to human applications and validation of the algorithm on human subjects is required. In most of the previous studies, the feasibility of SRU for in vivo kidney vasculature imaging was demonstrated on small animals using high frequency linear array transducers. However, for imaging the human kidney, a larger imaging depth, as well as a larger imaging field of view is required. Therefore, a curved linear array ultrasound probe commonly used in clinical abdominal imaging needs to be used. Few studies have been conducted to develop and evaluate SRU techniques using a curved array transducer on human subjects.

In the study of this chapter, we configured the deconvolution-based SRU algorithm on a clinical curved linear array transducer and applied the technology on healthy human subjects and patients with CKD. The performance of SRU imaging including the image resolution, and the capability of identifying the vascular changes between patients and healthy subject, were evaluated.

## **6.2 Material and Methods**

### **6.2.1 Study Approval and Human Subject Recruitment**

This human subject study was approved by Institutional Review Board of University of Pittsburgh. All experimental procedures including human subject recruitment and the ultrasound scan were performed in accordance with all guidelines and regulations detailed in the protocol. In this study, two healthy human subjects and 5 patients with CKD were recruited and scanned at University of Pittsburgh Medical Center. Written informed consent was obtained from all participants for the ultrasound scan.

### **6.2.2 Imaging Protocol**

During the scan, the human subjects were lying in the left lateral recumbent position to allow the ultrasound access to the right kidney. A clinical curved linear array probe (C5-2, ATL, centered at 3.125 MHz) connected to a programmable ultrasound system (Vantage 128, Verasonics, Remond, WI) was used for imaging the entire right kidney in long axis. The scan process is implemented by the custom-developed imaging and data acquisition sequence for human kidney SRU imaging. Firstly, the live mode multi-angle ( $-3^\circ$ ,  $-1.5^\circ$ ,  $0^\circ$ ,  $1.5^\circ$ ,  $3^\circ$ ) ultrasound plane wave imaging was used to locate the optimal long axis imaging section of the kidney. A bolus of 2mL microbubbles (Definity) at concentration of 13% was intravenously injected over 10 seconds to the healthy human subject followed by a 10mL saline flush, while the ultrasound probe was held at the imaging site. About thirty seconds after injection, the sequence was switched to data acquisition mode to collect a total of 2000 consecutive frames (500 frames/s) by the multi-

angle ultrasound plane wave imaging, while the subject held their breath during this period. The acquired raw RF data were post processed to reconstruct the final SRU image in Matlab (Mathworks, Natick, MA).

### **6.2.3 Adaptation to Curved Linear Array**

#### **6.2.3.1 Imaging Sequence**

During the ultrasound scan on the human subjects, two separate imaging modes are needed:

- 1) finding the optimized imaging section of long axis kidney with regular B-mode imaging, and
- 2) raw RF data acquisition at a high frame rate plane wave mode. However, breathing motion during human imaging, which affects the locations of the kidney in the abdomen significantly, can be more critical compared to the experiments on anesthetized animals that the pace of the breath is quite consistent. Therefore, we developed a customized imaging sequence for the ultrasound platform that combines the two imaging modes into one sequence, so that the time for switching the different imaging scripts can be saved and therefore the data acquisition can start as soon as the optimized imaging plane is located. The two modes use the same excitation waveform but have different frame rate and total number of acquisition frames. Figure 27 shows the user interface of the custom-designed sequence by adding the “SRU” button for initiating the data acquisition. The imaging sequence started with the regular live B-mode scan for locating the mid-section of long axis kidney. Then the probe was held still at the location and the microbubbles were injected, during which the subjects were allowed to breathe freely. After about thirty seconds of injection, the data acquisition started by turning the start button on, while the subject was asked to hold a breath during the time of data acquisition of about 3 seconds.

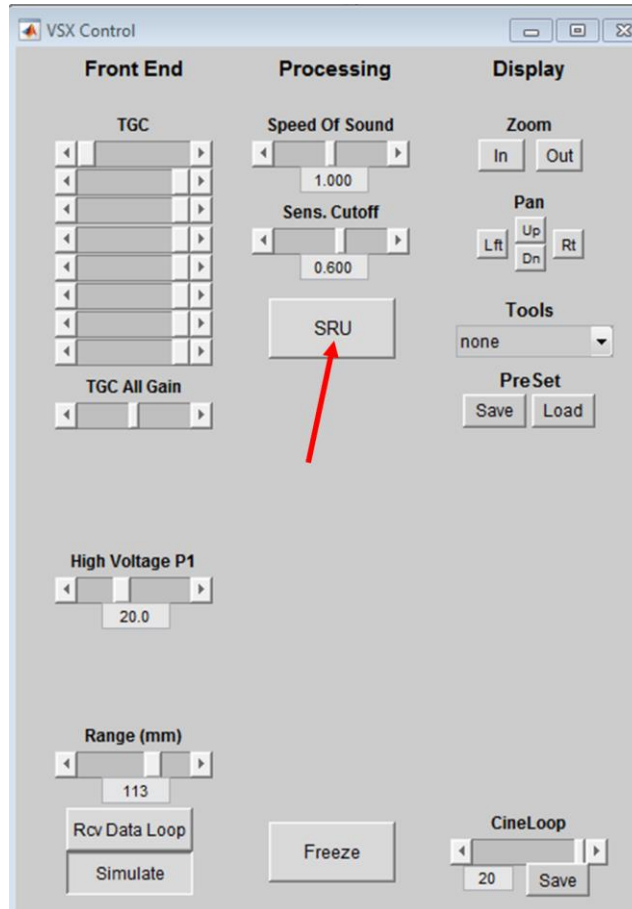


Figure 27 UI of the custom-designed sequence for human kidney imaging

### 6.2.3.2 Mechanical Index Limit for Safety

The mechanical index (MI) of the sequence was measured before the implementation on human subjects to ensure the safety. The MI is calculated as  $MI = \frac{P_{NP}}{\sqrt{f_c}}$ , in which  $P_{NP}$  is the negative peak pressure of the transmitted ultrasound wave, and  $f_c$  is the center frequency. The  $P_{NP}$  of the imaging sequence at 40 mm, which is about the average depth of the kidney, is measured to be 0.438 MPa by hydrophone (HNC, Onda Corp., Sunnyvale, CA). Thus, the MI is estimated to be 0.25, which is much lower than the limit of 1.9 that is suggested by the Food and Drug Administration. Considering the microbubble cavitation by ultrasound insonification, the measured number is also far lower than the MI of 1.8 that was reported to cause hemorrhage in kidney [118], [119].

### 6.2.3.3 PSF Measurement and Coordinate Transform

The raw data were processed with delay-and-sum beamforming, spatio-temporal eigen-based decomposition clutter filter (SVD filter) [51], and RL deconvolution algorithm [64]–[66] that was adapted and optimized to the curved array acquisition. The signal processing pipeline with the representative images for each step was shown in Figure 28. The final SRU image was reconstructed by summation of 300 consecutive frames (corresponding to 0.6 s) with minimized physiologic motion artifact.

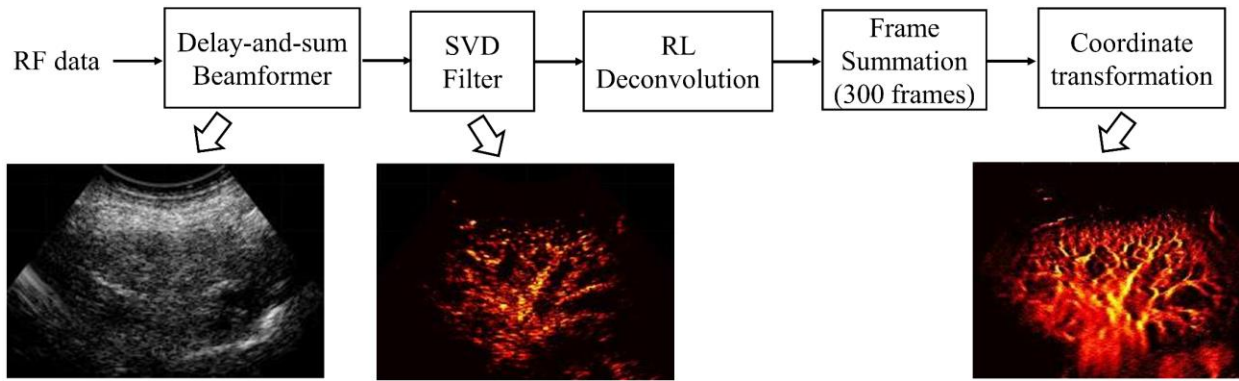


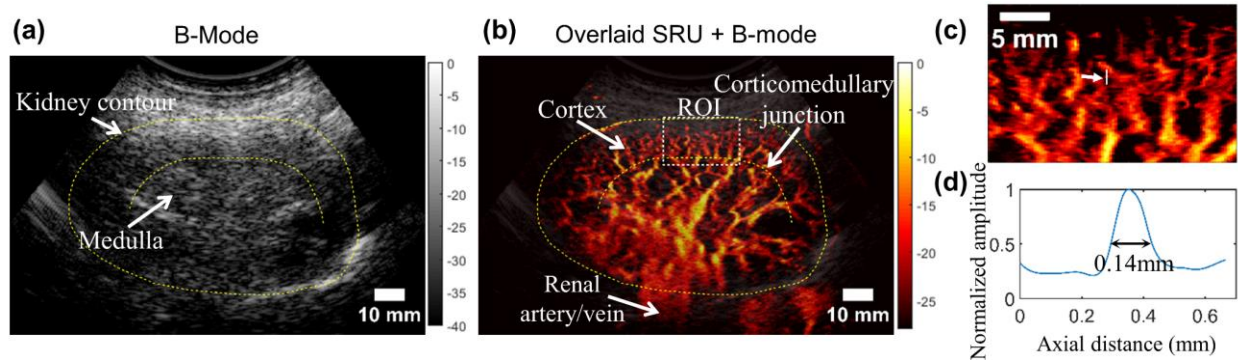
**Figure 28 SRU signal processing pipeline for human kidney imaging with representative images for each step.**

In the RL deconvolution part, the PSF is determined by the simulation packages provided by the ultrasound system (Vantage 128, Verasonics, Remond, WI). For the curved array transducer, the diverging beam was transmitted through the tissues. Thus, the size and shape of the PSF varies a lot along the lateral directions. Since the data acquisition is line by line by each piezoceramic element, the received RF data structure was stored in a matrix, the same as when using a linear array. In this study, we first estimated the PSF and ran the deconvolution as if imaging using a linear array transducer. The PSF was measured from the B-mode image reconstructed by the simulated RF data with a target at the depth of 60 mm, which is around the center of the kidney. After deconvolution and frame summation in the manner of linear array acquisition, the resulting line by line signals were transferred into polar coordinate for the final SRU image.

#### 6.2.4 Results

In this study, we scanned a total of 2 healthy human subjects and 5 patients with CKD. The analysis on the size, including longitudinal dimension, cortex thickness and cross-sectional area, and the vessel density in different areas, including the entire kidney and cortex, were performed based on the reconstructed SRU imaging. The results were compared between kidneys from healthy subjects and patients with CKD.

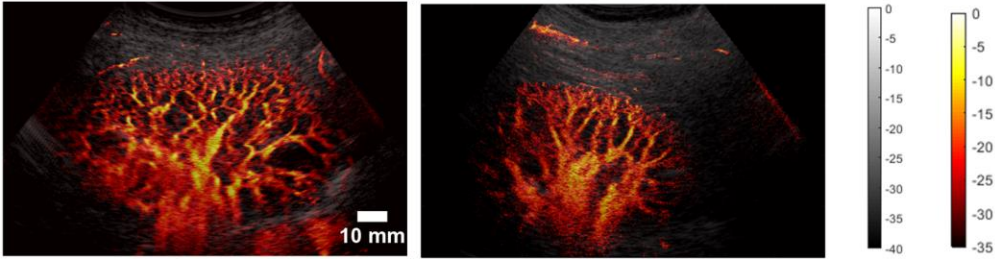
Figure 29 shows the representative B-mode image (a) and overlaid B-SRU image (b) of the kidney from a healthy subject. The SRU image of the human kidney vasculature network (Figure 29b) in the maximum long axis view was successfully reconstructed with a relatively high spatial resolution. Combining the B-mode (Figure 29a) and SRU images (Figure 29b), the overall vascular network and individual microvessels in different regions of the kidney, such as corticomedullary junction and cortex were identified with high resolution. Figure 29 (c) shows the zoomed-in image of the area marked by the yellow dotted rectangles in Figure 29 (b). The smallest renal microvessel identified, which is marked by the white solid line in Figure 29(c), was measured to be 0.14mm ( $<\lambda/3$ ), as shown by the short-axis cross-section signal profile (Figure 29d).



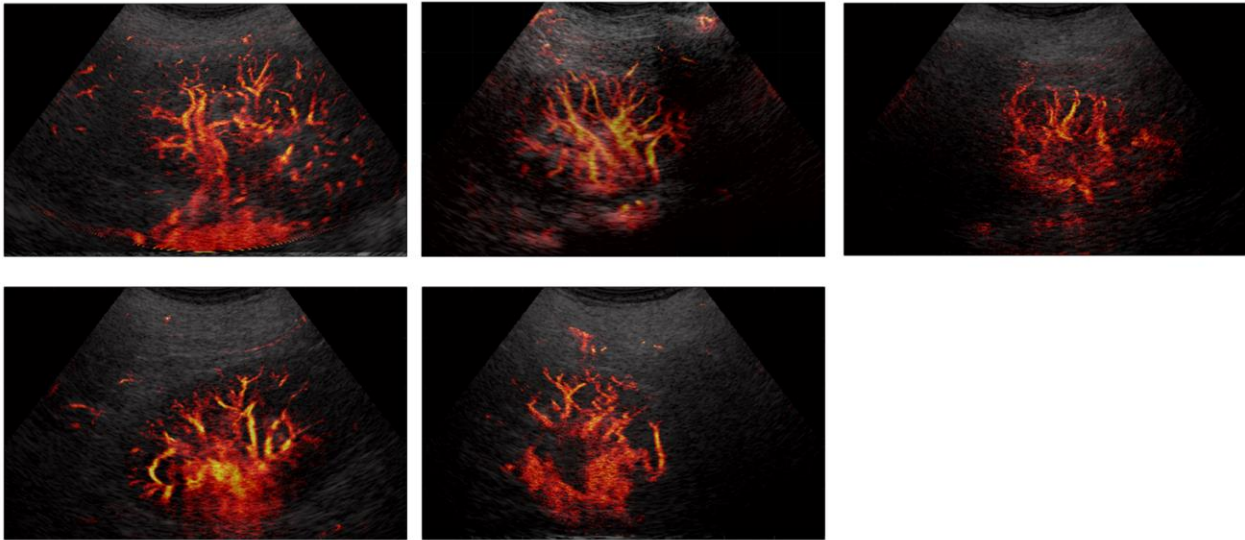
**Figure 29** (a) B-mode image of the human kidney. (b) Overlaid SRU and B-mode images of the kidney. (c) Zoomed in SRU image of the ROI indicated by white dashed rectangle in (b), with detectable smallest vessel marked by white arrow. (d) Spatial profile of the selected vessel. FWHM is estimated at 0.14 mm ( $< \lambda/3$ ).

Figure 30 presents the overlaid B-SRU images of the kidneys from all seven participants. The size reduction of the entire kidney can be found in the CKD kidneys compared to the healthy kidneys. Obvious overall vascular rarefaction was observed in the CKD kidneys. The loss of smaller vessel at the end of the branches of the major vessels was also identified. The quantitative analysis is shown in Table 1, which reveals the reduction in longitudinal dimension, cortex thickness and cross-sectional area of CKD kidneys compared to healthy kidneys. Thanks to the reconstructed vascular network at high spatial resolution by SRU, quantitative measurement of the rBV and vessel density in the cortex can be performed as shown in Table 2. The vascular rarefaction of the entire kidney, as well as in the cortex, was evidenced. Overall, the size reduction and vascular rarefaction could be found in CKD kidneys by SRU imaging, which agrees with the findings in previous studies [77]–[81], although the statistical significance was not performed due to the limited sample size of the healthy kidney in this study.

(a) Healthy kidneys



(b) Kidneys with CKD



**Figure 30 Overlaid B-SRU images of the kidneys from the total of two healthy human subjects and five CKD patients.**

**Table 1 Quantitative measurement of the sizes of the healthy and CKD kidneys**

	<b>Longitudinal dimension (mm)</b>					<b>Average (mm)</b>
<b>Healthy</b>	99.1	92.58				95.84
<b>CKD</b>	77.8	86.69	92.73	73.87	61.9	78.598
	<b>cortex thickness (mm)</b>					<b>Average (mm)</b>
<b>Healthy</b>	12.53	12.93				12.73
<b>CKD</b>	11.07	12.62	11.21	12.06	9.26	11.244
	<b>Cross-sectional area (mm<sup>2</sup>)</b>					<b>Average (mm<sup>2</sup>)</b>
<b>Healthy</b>	4546	4078				4312
<b>CKD</b>	3745	3654	3942	3600	2849	3558

**Table 2 Quantitative measurement of the vessel densities of the healthy and CKD kidneys**

	<b>Relative blood volume</b>					<b>Average</b>
<b>Healthy</b>	40.26%	39.63%				39.95%
<b>CKD</b>	31.17%	34.07%	35.97%	33.31%	35.30%	33.96%
	<b>Vessel density in the cortex</b>					<b>Average</b>
<b>Healthy</b>	53.21%	45.61%				49.41%
<b>CKD</b>	39.73%	36.25%	38.71%	35.50%	27.95%	35.63%

### **6.2.5 Discussion**

In this study, the SRU imaging technology was adapted to the clinical curved linear array probe and tested on both healthy human subjects and CDK patients, for which few studies have been done before. A good performance was demonstrated for imaging the human renal vascular network with a spatial resolution of 0.14 mm, which is smaller than one third of the ultrasound wavelength at 3.125 MHz. Through the first in human use study, we demonstrated for the first

time the capability of SRU for quantifying differences in microvascular structure between healthy and CKD human kidneys, with limited number of subjects. The developed technology and the imaging protocol would build a scheme for future extended study with a larger group of subjects.

CKD is a common problem significantly associated with morbidity and increasing prevalence. It is commonly diagnosed and monitored via serum creatinine. However, the staging and prognostication precision is limited due to the significant variability with age, race and muscle mass [120]. Therefore, the developed SRU imaging that can identify the microvascular changes could be a promising alternative for quantification of CKD. The SRU might provide one more piece of information that will allow us to determine the severity of CKD in a patient, and whether the patient will get worse over time. SRU technology has many other potential applications outside of CKD as well. One subject is to identify and monitor the microvascular changes during AKI-to-CKD progression, an example of which we have already presented in the encouraging results of the animal study in Chapter 4. Another area of interest is the renal transplant. Currently the gold standard for diagnosing transplant rejection is biopsy of the transplanted kidney. There have been several studies showing CEU imaging has promise detecting allograft rejection [121], [122]. With the superior spatial resolution compared to the conventional CEU, SRU could be a more appropriate tool to avoid invasive biopsies and could lead to safer and more rapid diagnosis of transplant rejection.

This study also has several limitations. Firstly, due to the limited number of subjects, especially healthy human subjects, the statistical analysis of the quantitative measurements was not performed. The extended and more systematic study with a larger sample size is required to determine the SRU capability of the quantitative assessment of human kidney. Concerning the imaging technology, the PSF used in the deconvolution process also varies in the axial direction,

especially in human kidney imaging since the imaging range in the axial direction is quite substantial. An adaptive deconvolution algorithm based on depth dependent PSF is suggested to achieve a better accuracy in locating the microbubbles, therefore resulting in a more robust reconstruction of the vascular network. It should be noted that all the scans were performed on subjects with moderate BMI, by which the kidney is located at a relatively shallower depth. For imaging the kidney at deeper locations, the attenuation from the tissue could be a problem that reduces the imaging sensitivity. The coded excitation technique, which enhances the penetration and SNR without sacrificing much of the spatial resolution and raising the MI by transmitting longer coded signals through the tissues and compressing the receiving signals, could be sought as a potential solution [123]–[126].

### **6.2.6 Conclusions**

In this study, we successfully adapted the SRU technology to a clinical curve linear array that provides larger field of view and imaging depth for human kidney imaging and performed the pilot test on both healthy human subjects and CKD patients. The fine vascular network was reconstructed by SRU at the spatial resolution of 0.14 mm, which is smaller than one third of wavelength at 3.125 MHz. The overall kidney size reduction and vascular rarefaction was identified qualitatively and quantitatively in CKD kidneys compared to the healthy kidney with limited number of subjects. The efforts in this study initiated the translation of SRU technology into clinics, for which not many studies have been previously reported.

## 7.0 SRU Imaging of Vasa Vasorum in Rabbit Atherosclerotic Plaques

*The work presented in this chapter was reprinted from Q. Chen et al., “Validation of Ultrasound Super-Resolution Imaging of Vasa Vasorum in Rabbit Atherosclerotic Plaques,” IEEE Trans. Ultrason. Ferroelectr. Freq. Control, vol. 67, no. 8, pp. 1725–1729, Aug. 2020, doi: 10.1109/TUFFC.2020.2974747, with the permission of IEEE Publishing. © 2020 IEEE.*

### 7.1 Introduction

Acute coronary syndromes and strokes are mainly caused by the atherosclerotic plaque (AP) rupture [127]–[132]. It has been reported that the dense neovasculature of vasa vasorum (VV), infiltrating into the AP core and resulting in excessive micro-vasculatures, may lead to intraplaque hemorrhage, which plays a critical role in AP rupture [131], [133]–[135]. Thus, adventitial VV and their infiltration into the AP core is together a key evidence of AP progression and vulnerability [131], [135]–[140]. Therefore, a noninvasive imaging tool for detecting and monitoring the VV development near major vessels is of great importance for preclinical and clinical studies.

However, due to its tiny size, it is challenging to identify VV in vivo. Contrast-enhanced magnetic resonance imaging [141]–[143], microcomputed tomography [144], [145], and optical coherence tomography [146], [147], have successfully imaged VV with high spatial resolution in preclinical studies; however they exhibited limitations such as hazardous contrast agents, radiation, or poor imaging depth, respectively. Ultrasound (US) imaging has also been explored as a potential

modality for imaging micro-vessels. High-frequency intravascular US provides a high spatial resolution [148]–[151], but it is invasive. As a transcutaneous imaging approach, low-frequency CEU [152]–[154] does not provide sufficient spatial resolution within the acoustic diffraction limit (ADL). Until now, there is no well-established imaging technology that can visualize VV in a noninvasive, safe and high-resolution manner.

As introduced in the above chapters, the emerging in vivo SRU imaging technology [37], [38], [155], [39]–[46] can provide unprecedented spatial resolution of microvasculature and has been successfully tested on different animal models. Therefore, SRU imaging can also be a promising transcutaneous imaging tool for VV detection. In the previous studies, our group has already performed a pilot test for imaging the VV in the rabbit AP using the developed deconvolution-based SRU technology with spatio-temporal-interframe-correlation (STIC) algorithm that significantly improves the temporal resolution and mitigates the cardiac motion artifacts [42]. Despite successful in vivo demonstration of the technical capability of SRU in identifying VV in rabbit AP, a further systematic validation study comparing with both histopathological and anatomical evidence, is still required for future verification of the repeatability and reproducibility in VV identification. An established experiment protocol for such validation is needed for the extensive studies and would also benefit the research in other disease models using SRU.

In this work, we introduce a protocol of SRU imaging for VV detection along with the systematic validations. The deconvolution-based SRU imaging technology was first performed in vivo on two rabbits of a well-established AP model [153] for identifying the VV in both injured and uninjured femoral arteries. The identification of VV by SRU was then histopathologically and morphologically verified by hematoxylin and eosin (H&E) and CD31 stain, and ex-vivo micro-computed tomography ( $\mu$ CT) scan, respectively.

## **7.2 Material and Methods**

### **7.2.1 Rabbit Atherosclerotic Plaque Model**

As shown in Figure 31(a), two New Zealand white male rabbits were fed a high-fat-high-cholesterol diet (HFHC) (cholesterol 1%, peanut oil 2.5%, and fat 10%) for six weeks [153]. One week after the diet started, the balloon injury was performed in the right superficial femoral arteries of the two rabbits under anesthesia (ketamine 150 mg IM, xylazine 8 mg IM and 2.5% inhaled isoflurane) by using a 2F Fogarty balloon catheter (Edwards Life Sciences, USA) to induce the plaque development. The balloon catheter was introduced to the bifurcation area of the femoral artery, inflated to 2 atm, and moved back and forth several times to induce the injury to the vessel wall with the guidance of high-frequency ultrasound scan (Vevo2100, FUJIFILM Visualsonics, ON, Canada).

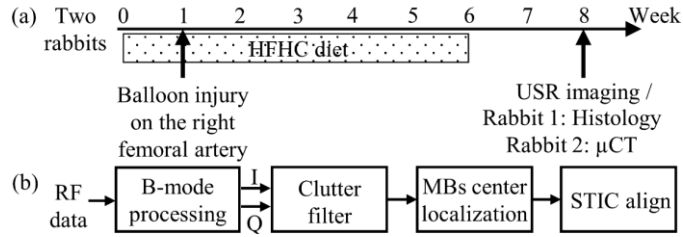


**Figure 31 (a) Study timeline. (b) Signal processing procedure of SRU imaging.**

### 7.2.2 SRU Imaging and Validation Protocol

At week 8, in vivo ultrasound imaging was performed on both injured and uninjured rabbit femoral arteries, followed with histology and  $\mu$ CT on the excised artery samples. The SRU imaging sequence was operated by a programmable ultrasound system (Vantage 128, Verasonics, Kirkland, WI) equipped with a 15.6 MHz linear array ultrasound probe (L22-14v, Verasonics, Kirkland, WI). The rabbit was prepared with femoral fur shaved, ear vein catheter placed, and kept anesthetized during the imaging process. Regular B-mode ultrasound imaging was used to locate the bifurcation area of the femoral artery. Then the probe was fixed to a probe holder to ensure the stability during the following data acquisition process. A bolus of 0.2 mL MBs (Definity, diameter 1- 4  $\mu$ m, Lantheus Medical Imaging, MA) was intravenously administrated through the ear vein. About 30 seconds after injection, RF data of 3000 effective frames were acquired using multi-angle ( $-3^\circ$ ,  $-1.5^\circ$ ,  $0^\circ$ ,  $1.5^\circ$ ,  $3^\circ$ ) plane wave imaging using two cycles per pulse at an effective frame rate of 500Hz. The ultrasound scan was repeated on another imaging plane separated by image slice thickness of about 0.5 mm for both injured and contralateral uninjured side.

Upon completing SRU scan, a relatively large block of femoral tissues ( $\sim$ 4 cm) containing femoral arteries from both injured and uninjured sides of the first rabbit were excised after euthanasia and formalin fixed. Then, the bifurcation area in the tissue was located with the

guidance of 3D ultrasound scan (Vevo2100). The tissue around the bifurcation was further trimmed out into a small block of 0.5 mm for paraffin embedding and sectioning. The slices were processed with H&E stain for plaque identification and Immunohistochemistry of CD31 (ab199012, Abcam, Cambridge, MA, USA) stain for identification of neovessels surrounding the plaque.

Upon completion of SRU scan of the second rabbit, the animal was euthanized and perfused with 50 mL rubber-based radiopaque contrast agent (Microfil, Flow Tech, Carver, MA) through the access to femoral artery at a constant flow rate of 5 mL/min using a syringe pump (KD Scientific, Holliston, MA). Twenty minutes later when the contrast agent was fully cured, the femoral arteries were excised along with a block of the surrounding (~30 mm in diameter and 65 mm in length) connective tissues and fixed in formalin solution. With the help of CT scan with a relatively large field of view (40×40mm) and a medium spatial resolution (25  $\mu$ m) (Inveon, Siemens, Tarrytown, NY), the tissue block was trimmed to the appropriate size (~12 mm in diameter), enabling a higher resolution scan by Scanco  $\mu$ CT 50 (ScCANCO Medical, Switzerland) system with 10  $\mu$ m voxel size, 55 kVp, 800 ms exposure time, in 70% alcohol as a medium. The study was approved by the Institutional Animal Care and Use Committee (IACUC) at the University of Pittsburgh.

### **7.2.3 SRU Signal Processing Procedure**

The general signal processing procedure (Figure 31b) is similar to that describe in Chapter 4. As shown in Figure 31(b), the acquired RF channel data were first reconstructed to IQ-data using the delay-and-sum beamforming. Then the echo signals only from MBs were extracted by applying the singular value decomposition (SVD) based spatio-temporal clutter filter [51] on the

IQ-data. The tissue component over IQ data in 500 ensembles were suppressed by the clutter filter. After envelope detection and thresholding, the images containing only MB signals were interpolated to achieve sub-wavelength precision and deconvolved using RL deconvolution algorithm with pre-estimated PSF to localize the center of each MB [64]–[66]. All 3000 frames over the 6 seconds of the localized MBs in blood flow were realigned by synchronizing to the estimated cardiac cycle according to the MB density using the STIC based data re-alignment algorithm [42]. The final SRU image in one effective cardiac cycle was reconstructed by summing up 300 frames of deconvolved signals rearranged from about 30 cardiac cycles. The entire SRU image reconstruction was processed off-line in MATLAB (Mathworks, Natick, MA).

### **7.3 Results and Discussion**

The first two columns of Figure 32 depict the B-mode, and overlaid SRU and B-mode images of the area near bifurcation, where the balloon injury was performed, of the uninjured and injured femoral arteries of the first rabbit. The femoral artery and surrounding VV, as well as some other small vessels nearby, were clearly identified by SRU. For each side, two sets of images acquired from two different imaging planes separated by image slice thickness of ~0.5 mm are shown. Note the SRU images at systole were selected for consistent comparison and better demonstration of VV. The AP formation was observed in the injured femoral artery. The vessel wall boundaries manually identified based on echogenicity from B-mode images were marked with white dashed lines. In the SRU images of the second column, white arrows indicate the identified VV in the adventitia and within the plaque. Significant abundance of VV was found in the injured side compared to the uninjured side. The VV density inside the vessel wall was

estimated to be 3.75% for the injured side and 1.04% for the uninjured side. The plaque formation was confirmed by histology with H&E stain (A5, B5). In B5, plaque was identified inside the endothelium in the tunica intima of the lumen drawn with yellow solid line. The last two columns display the immunohistochemistry with CD31 stain identifying the vessel in the corresponding section. VV was enriched abnormally in the injured side and penetrating into the plaque characterized in H&E stain. The population of VV around adventitia and plaque measured in CD31 stain in the injured side was approximately 3-fold higher than the uninjured side, which closely matched with the estimation by SRU.

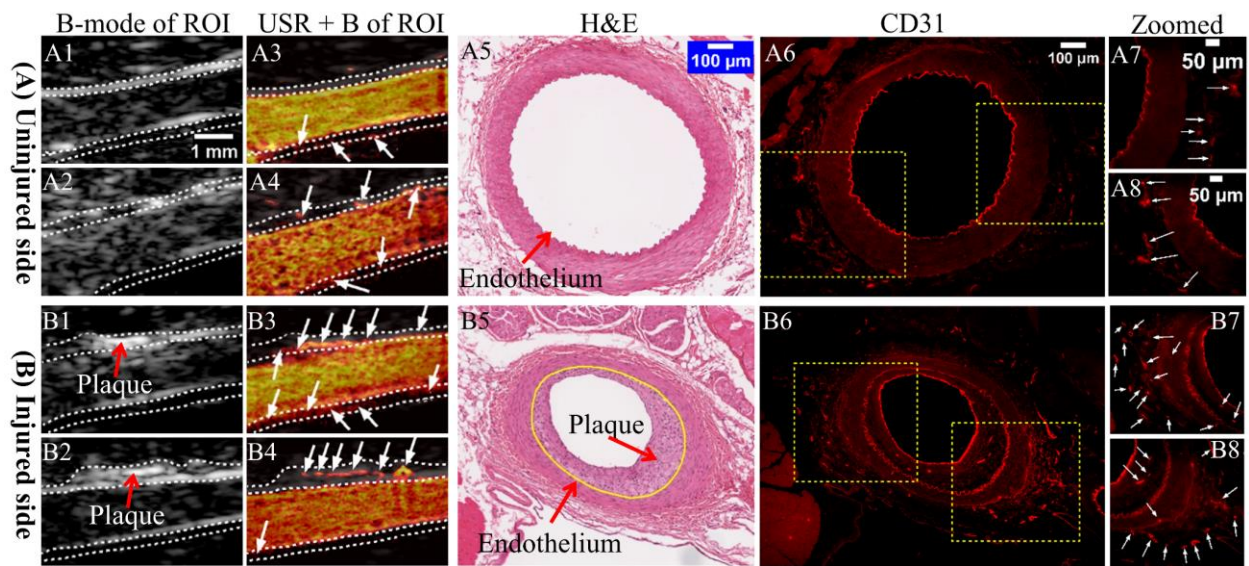


**Figure 32** B-mode, SRU overlaid on B-mode images, H&E, and CD31 stain of the contralateral uninjured side (A) and injured side (B) of the femoral arteries from rabbit #1. Two image slices separated by ~ 0.5mm were taken by ultrasound on each side. Column 1 and 2 depict the B-mode and SRU images of area that were suspected for plaque and VV development. The white dotted lines represent vessel wall and white arrows indicate VV. Significant plaque development was evidenced in the injured side (B5) and verified by H&E stain (column 3). A significantly increased VV population in the adventitia area and VV infiltrated into the plaque were identified from SRU images (column 2) and validated by CD31 stain (column 4, 5).

In Figure 33, the SRU images on the injured side of the second rabbit were compared with the contralateral uninjured side along with the  $\mu$ CT images for anatomical validation. AP formation and increased VV population on the injured side were shown in SRU images. The VV density inside the vessel wall was estimated to be 6.30% on the injured side and 1.94% on the uninjured side. Column 3 shows a general view of the corresponding  $\mu$ CT images around the bifurcation. Column 4 provides magnified views at  $0^\circ$  and  $270^\circ$  of the ROI, denoted in yellow dashed rectangle in column 3. In the  $\mu$ CT images of the injured side (B), much crowded small vessels were identified in the area near the bifurcation, where the balloon injury was performed, marked by a white arrow (B5, B6, B7), while no such feature was found in the corresponding area (A5, A6, A7) on the uninjured side (A). Thus, the abnormally populated VV network was directly evidenced by  $\mu$ CT. Figure 34(a) shows the SRU image with a larger field of view in the imaging plane of B4. The typical VV structure inside the white dashed rectangle at about 6 mm away from bifurcation was also identified at the same location in the  $\mu$ CT image (B6 in Figure 33). Figure 34(b) and (c) show the zoomed-in SRU and  $\mu$ CT image of the area. The estimated size of the vessel by  $\mu$ CT ( $\sim 121 \mu\text{m}$ ) supports the estimation by SRU ( $\sim 134 \mu\text{m}$ ).

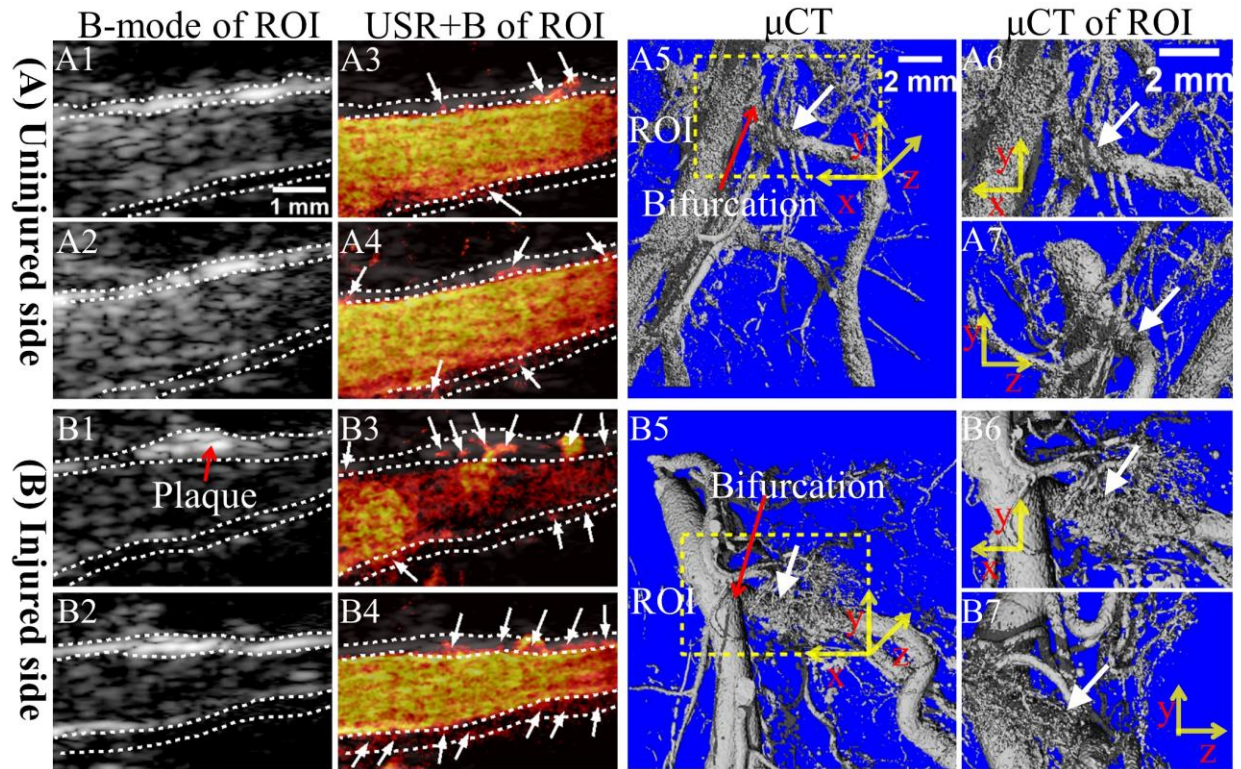
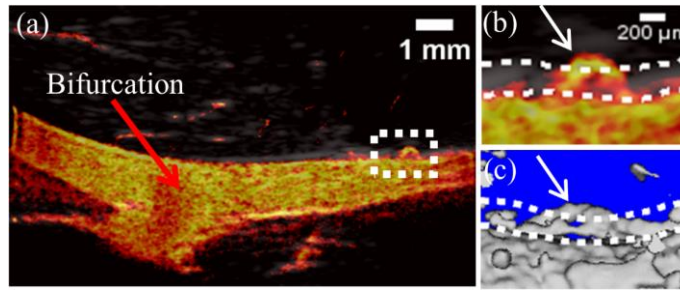


Figure 33 B-mode, SRU overlaid on B-mode, and  $\mu$ CT images of the uninjured side (A) and injured side (B) of the femoral arteries from rabbit #2. Column 3 shows the 3D  $\mu$ CT images of the harvested arteries. Column 4 displays ROI marked in yellow box in column 3, with higher magnification at  $0^\circ$  and  $270^\circ$  view. Increase of VV population was observed in injured side compared to uninjured side by SRU, and evidenced by corresponding  $\mu$ CT images.



**Figure 34 (a) Full view of femoral artery in the imaging plane of B4 in Figure 33. White dashed rectangle marks the area where excessive VV development around the plaque is identified. (b) Zoomed-in SRU image of the area. (c) The matching  $\mu$ CT image of the same area.**

It should be noted that although overall VV proliferation and some specific VV in SRU images were evidenced by  $\mu$ CT, the complete comparison in 3-D with ex-vivo  $\mu$ CT was hindered due to the limited imaging slices of SRU. Therefore, 3-D ultrasound scan would be encouraged to provide volumetric information and more robust correlation with  $\mu$ CT. There are also limitations in our SRU imaging technology. Although the VV detected by our SRU approach compare reasonably well with histology in vessel density and mCT in morphology, it should be noted that there could have been very tiny VV with very slow blood flow undetected by applying a SVD filter with a fixed parameter that is optimal only for a nominal VV blood flow speed range. In the future, we would explore a method to adaptively extract the vessels at different blood flow speed, for example by temporally adjusting data arrangements or applying 3-D SVD filtering technique that can differentiate slow-speed from fast-speed flow [156]. The RL deconvolution algorithm we applied in image reconstruction was shown to be able to resolve crowded microbubbles individually and thus allowed for a greatly increased temporal resolution [42]. However, it should be noted that since the RL deconvolution algorithm is an iterative maximum likelihood method,

the performance can be affected in some area where microbubbles are too close to each other. Moreover, the RL deconvolution algorithm depends on the accuracy of the pre-defined PSF. A fixed PSF was applied in the deconvolution process, while the actual PSF varies in different imaging depth although the difference might remain small. To improve the accuracy of the microbubble center localization, a deconvolution algorithm using adaptive PSF needs to be investigated.

Overall, the abnormal proliferation of adventitia VV around rabbit femoral arteries and their infiltration into AP along with plaque development can be detected by SRU imaging. The SRU scan was validated by histology stains as a gold standard for histopathology changes and by  $\mu$ CT as a directly visualized characterization with high resolution. While the overall VV density and distribution vary in different vascular beds in normal conditions, the roles of VVs in the formation and progression of atherosclerosis are considered to be similar in their proliferation and infiltration [157]. Thus, the validation in femoral artery can also promote the investigation in other vessel beds such as carotid and coronary arteries. Since the systematic validation procedures for SRU in identifying VV in AP were established in this study, further extended studies using a larger group of animals including a longitudinal monitoring can be designed. As a long-term goal, translation of the SRU technology for predict the AP rupture by imaging VV in human atherosclerotic disease can be envisioned. These established logistics and experiment protocols with histology and  $\mu$ CT validation would also be a guidance for the applications of SRU on other disease models.

## **7.4 Conclusions**

In the study, SRU imaging was successfully applied for identifying the VV in the rabbit AP. The robustness of the imaging performance was validated histopathologically by H&E and CD31 stain, and morphologically by  $\mu$ CT scan. The imaging and validation protocols of VV imaging using SRU were established. These protocols may pave the way for future extended experiments on a larger group of animals for investigating SRU as a noninvasive transcutaneous imaging tool for VV identification and characterization, as well as other biomedical applications.

## 8.0 Conclusions and Future Directions

In this dissertation, we demonstrate the development of two novel ultrasound technologies based on the idea of tracking and locating small particles.

In Chapter 2 and Chapter 3, we focus on the development of ultrasound tracking technology for the artificial acoustically actuated microswimmers. The proof-of-concept of the proposed ultrasound tracking approach, which has never been suggested before, was first validated in a 2-D setup *in vitro* by comparing with the synchronized camera tracking. Subsequently, for the practical application of the microswimmer that navigates in the biomedical environment *in situ*, a 3-D ultrasound tracking system using two clinical probes that were translated by the step motors to track the arbitrary 3-D motion of the lab-made 3-D microswimmer was designed. The system provides a relatively high tracking accuracy by comparing with the camera as demonstrated in the *in vitro* experiment. Overall, this work proposed a promising approach for tracking the motion of the microswimmers in biomedical applications and built a solid foundation for future efforts for the clinical translation of the microswimmer technology. As the next step, the *ex vivo* validation using an excised animal organ is sought before *in vivo* preclinical study. The eventual goal of the research program is the development of the microswimmer technology combining the propulsion, tracking and feedback control strategies together, which will allow tasks such as drug delivery in real clinical applications.

In Chapter 4 through Chapter 7, we aimed at the development of the SRU imaging technology. The developed deconvolution-based SRU imaging achieved a spatial resolution smaller than one third of wavelength, which is beyond the acoustic diffraction limit, as validated firstly *in vitro* using vessel mimicking microfluidic channels, and demonstrated subsequently in the animal and human subject studies. The validation using custom-designed microfluidic chip as the ground truth on the scale of under tens of microns was performed for the first time to the best of our knowledge for SRU imaging. This proposed test method could be a practical scheme for the future studies in which the imaging capability of SRU imaging can be systematically tested. Through the *in vivo* preclinical animal studies, fine microvascular network in high spatial resolution was reconstructed, which allowed for the quantitative assessment of vascular changes due to the disease progression. In the application on the mouse AKI model, the capability for noninvasive and quantitative assessment of the changes in kidney morphology and vasculature, including size, rBV, vessel density and tortuosity, was demonstrated. The vessel density measurement by SRU correlated well with the histological measurement, which evidenced the potential of SRU as a noninvasive diagnostic tool for the progressive kidney disease. Subsequently, the SRU algorithm was configured to the clinical curved array probe and successfully applied on human subjects by identifying the size and vascular changes between healthy and CKD kidneys. These results show a great potential of SRU imaging as a diagnostic tool for kidney diseases. In the VV study, the capability of SRU imaging for identifying the VV in the rabbit AP was shown, which was validated with histology and  $\mu$ CT. The established imaging and validation protocol would facilitate future similar studies for imaging the VV. As the future direction of the SRU project, the further extended experiments on larger groups of subjects or animals are required to promote the clinical translation of this technology. In parallel with the translational efforts, SRU

algorithm using deep learning approach, which has the potential to achieve a higher spatial and temporal resolution under the conditions that the microbubbles are not uniformly distributed, will be investigated. A systematic validation of further advanced SRU algorithms and different operating frequencies using a well-designed microfluidic chip with various sizes of the channels that separated in various distances is planned.

We envision that a unique tool for various biomedical applications of the novel microdrones for diagnosis and drug delivery can be developed by integrating novel SRU technology with a reliable tracking capability of microparticles. For the long-term goal of the research program, we seek to combine the microswimmer tracking and SRU imaging technology to perform in situ tasks inside the human body, such as providing enhanced contrast of the very tiny vessels aided by the microswimmers propelling through or providing the detailed structure by SRU for better tracking and controlling of the microswimmers.

## Bibliography

- [1] S. Sengupta, M. E. Ibele, and A. Sen, “Fantastic Voyage: Designing Self-Powered Nanorobots,” *Angew. Chemie Int. Ed.*, vol. 51, no. 34, pp. 8434–8445, Aug. 2012, doi: 10.1002/anie.201202044.
- [2] JianFeng and S. Cho, “Mini and Micro Propulsion for Medical Swimmers,” *Micromachines 2014, Vol. 5, Pages 97-113*, vol. 5, no. 1, pp. 97–113, Feb. 2014, doi: 10.3390/MI5010097.
- [3] B. J. Nelson, I. K. Kaliakatsos, and J. J. Abbott, “Microrobots for Minimally Invasive Medicine,” *Annu. Rev. Biomed. Eng.*, vol. 12, no. 1, pp. 55–85, Jul. 2010, doi: 10.1146/annurev-bioeng-010510-103409.
- [4] M. Sitti, “Miniature devices: Voyage of the microrobots,” *Nature*, vol. 458, no. 7242, pp. 1121–1122, Apr. 2009, doi: 10.1038/4581121a.
- [5] D. Patra, S. Sengupta, W. Duan, H. Zhang, R. Pavlick, and A. Sen, “Intelligent, self-powered, drug delivery systems,” *Nanoscale*, vol. 5, no. 4, pp. 1273–1283, Jan. 2013, doi: 10.1039/C2NR32600K.
- [6] A. Vikram Singh and M. Sitti, “Targeted Drug Delivery and Imaging Using Mobile Milli/Microrobots: A Promising Future Towards Theranostic Pharmaceutical Design,” *Curr. Pharm. Des.*, vol. 22, no. 11, pp. 1418–1428, 2016, doi: 10.2174/1381612822666151210124326.
- [7] D. Gourevich *et al.*, “Ultrasound-mediated targeted drug delivery with a novel cyclodextrin-based drug carrier by mechanical and thermal mechanisms,” *J. Control. Release*, vol. 170, no. 3, pp. 316–324, Sep. 2013, doi: 10.1016/J.JCONREL.2013.05.038.
- [8] L. K. E. A. Abdelmohsen, F. Peng, Y. Tu, and D. A. Wilson, “Micro- and nano-motors for biomedical applications,” *J. Mater. Chem. B*, vol. 2, no. 17, pp. 2395–2408, Apr. 2014, doi: 10.1039/C3TB21451F.
- [9] S. C. Lenaghan *et al.*, “Grand Challenges in Bioengineered Nanorobotics for Cancer Therapy,” *IEEE Trans. Biomed. Eng.*, vol. 60, no. 3, pp. 667–673, Mar. 2013, doi: 10.1109/TBME.2013.2244599.
- [10] T. Mirkovic, N. S. Zacharia, G. D. Scholes, and G. A. Ozin, “Fuel for Thought: Chemically Powered Nanomotors Out-Swim Nature’s Flagellated Bacteria,” *ACS Nano*, vol. 4, no. 4, pp. 1782–1789, Apr. 2010, doi: 10.1021/nm100669h.
- [11] C. Bergeles and Guang-Zhong Yang, “From Passive Tool Holders to Microsurgeons: Safer, Smaller, Smarter Surgical Robots,” *IEEE Trans. Biomed. Eng.*, vol. 61, no. 5, pp. 1565–1576, May 2014, doi: 10.1109/TBME.2013.2293815.

- [12] W. Yang, V. R. Misko, K. Nelissen, M. Kong, and F. M. Peeters, "Using self-driven microswimmers for particle separation," *Soft Matter*, vol. 8, no. 19, p. 5175, 2012, doi: 10.1039/c2sm07382j.
- [13] N. Chronis and L. P. Lee, "Electrothermally activated SU-8 microgripper for single cell manipulation in solution," *J. Microelectromechanical Syst.*, vol. 14, no. 4, pp. 857–863, Aug. 2005, doi: 10.1109/JMEMS.2005.845445.
- [14] S. Sacanna *et al.*, "Shaping colloids for self-assembly," *Nat. Commun.*, vol. 4, no. 1, p. 1688, Dec. 2013, doi: 10.1038/ncomms2694.
- [15] G. Vince and C. Wilson, "The rise of the miniature medical robots," *New Sci.*, vol. 204, no. 2735, pp. 50–53, Nov. 2009, doi: 10.1016/S0262-4079(09)63077-3.
- [16] J. Wang, "Can Man-Made Nanomachines Compete with Nature Biomotors?," *ACS Nano*, vol. 3, no. 1, pp. 4–9, Jan. 2009, doi: 10.1021/nn800829k.
- [17] J. Feng, J. Yuan, and S. K. Cho, "Micropropulsion by an Acoustic Bubble for navigating microfluidic spaces," *Lab Chip*, vol. 15, pp. 1554–1562, 2015, doi: 10.1039/C4LC01266F.
- [18] S. Martel, C. C. Tremblay, S. Ngakeng, and G. Langlois, "Controlled manipulation and actuation of micro-objects with magnetotactic bacteria," *Appl. Phys. Lett.*, vol. 89, no. 23, p. 233904, Dec. 2006, doi: 10.1063/1.2402221.
- [19] B. Behkam and M. Sitti, "Bacterial flagella-based propulsion and on/off motion control of microscale objects," *Appl. Phys. Lett.*, vol. 90, no. 2, p. 023902, Jan. 2007, doi: 10.1063/1.2431454.
- [20] J. Simmchen, J. Katuri, W. E. Uspal, M. N. Popescu, M. Tasinkevych, and S. Sánchez, "Topographical pathways guide chemical microswimmers," *Nat. Commun.*, vol. 7, p. 10598, Feb. 2016, doi: 10.1038/ncomms10598.
- [21] W. F. Paxton *et al.*, "Catalytic Nanomotors: Autonomous Movement of Striped Nanorods," *J. Am. Chem. Soc.*, vol. 126, no. 41, pp. 13424–13431, Oct. 2004, doi: 10.1021/ja047697z.
- [22] S. Ramakrishnan and C. Shannon, "Display of Solid-State Materials Using Bipolar Electrochemistry," *Langmuir*, vol. 26, no. 7, pp. 4602–4606, Apr. 2010, doi: 10.1021/la100292u.
- [23] G. Zhao, M. Viehrig, and M. Pumera, "Challenges of the movement of catalytic micromotors in blood," *Lab Chip*, vol. 13, no. 10, p. 1930, May 2013, doi: 10.1039/c3lc41423j.
- [24] L. Restrepo-Pérez, L. Soler, C. Martínez-Cisneros, S. Sánchez, and O. G. Schmidt, "Biofunctionalized self-propelled micromotors as an alternative on-chip concentrating system," *Lab Chip*, vol. 14, no. 16, pp. 2914–2917, Jul. 2014, doi: 10.1039/C4LC00439F.

- [25] R. Dreyfus, J. Baudry, M. L. Roper, M. Fermigier, H. A. Stone, and J. Bibette, “Microscopic artificial swimmers,” *Nature*, vol. 437, no. 7060, pp. 862–865, Oct. 2005, doi: 10.1038/nature04090.
- [26] A. Snezhko, M. Belkin, I. S. Aranson, and W.-K. Kwok, “Self-Assembled Magnetic Surface Swimmers,” *Phys. Rev. Lett.*, vol. 102, no. 11, p. 118103, Mar. 2009, doi: 10.1103/PhysRevLett.102.118103.
- [27] L. Zhang *et al.*, “Characterizing the Swimming Properties of Artificial Bacterial Flagella,” *Nano Lett.*, vol. 9, no. 10, pp. 3663–3667, Oct. 2009, doi: 10.1021/nl901869j.
- [28] A. Ghosh and P. Fischer, “Controlled Propulsion of Artificial Magnetic Nanostructured Propellers,” *Nano Lett.*, vol. 9, no. 6, pp. 2243–2245, Jun. 2009, doi: 10.1021/nl900186w.
- [29] R. S. M. Rikken, R. J. M. Nolte, J. C. Maan, J. C. M. van Hest, D. A. Wilson, and P. C. M. Christianen, “Manipulation of micro- and nanostructure motion with magnetic fields,” *Soft Matter*, vol. 10, no. 9, pp. 1295–1308, Feb. 2014, doi: 10.1039/C3SM52294F.
- [30] N. Bertin *et al.*, “Propulsion of bubble-based acoustic microswimmers,” *Phys. Rev. Appl.*, vol. 4, no. 6, pp. 1–5, 2015, doi: 10.1103/PhysRevApplied.4.064012.
- [31] M. Kaynak, A. Ozcelik, A. Nourhani, P. E. Lammert, V. H. Crespi, and T. J. Huang, “Acoustic actuation of bioinspired microswimmers,” *Lab Chip*, vol. 17, no. 3, pp. 395–400, 2017, doi: 10.1039/C6LC01272H.
- [32] K. J. Rao, F. Li, L. Meng, H. Zheng, F. Cai, and W. Wang, “A Force to Be Reckoned With: A Review of Synthetic Microswimmers Powered by Ultrasound,” *Small*, vol. 11, no. 24, pp. 2836–2846, Jun. 2015, doi: 10.1002/smll.201403621.
- [33] R. J. Dijkink, J. P. van der Dennen, C. D. Ohl, and A. Prosperetti, “The ‘acoustic scallop’: a bubble-powered actuator,” *J. Micromechanics Microengineering*, vol. 16, no. 8, pp. 1653–1659, 2006, doi: 10.1088/0960-1317/16/8/029.
- [34] D. Ahmed, X. Mao, J. Shi, B. K. Juluri, and T. J. Huang, “A millisecond micromixer via single-bubble-based acoustic streaming †,” 2009, doi: 10.1039/b903687c.
- [35] D. Ahmed *et al.*, “Selectively manipulable acoustic-powered microswimmers,” *Sci. Rep.*, vol. 5, no. 1, p. 9744, Sep. 2015, doi: 10.1038/srep09744.
- [36] J. Feng, J. Yuan, and S. K. Cho, “2-D steering and propelling of acoustic bubble-powered microswimmers,” *Lab Chip*, vol. 16, no. 12, pp. 2317–2325, 2016, doi: 10.1039/C6LC00431H.
- [37] O. Couture, V. Hingot, B. Heiles, P. Muleki-Seya, and M. Tanter, “Ultrasound Localization Microscopy and Super-Resolution: A State of the Art,” *IEEE Trans. Ultrason. Ferroelectr. Freq. Control*, vol. 65, no. 8, pp. 1304–1320, Aug. 2018, doi: 10.1109/TUFFC.2018.2850811.

- [38] C. Errico *et al.*, “Ultrafast ultrasound localization microscopy for deep super-resolution vascular imaging,” *Nature*, vol. 527, no. 7579, pp. 499–502, 2015, doi: 10.1038/nature16066.
- [39] Y. Desailly, O. Couture, M. Fink, and M. Tanter, “Sono-activated ultrasound localization microscopy,” *Appl. Phys. Lett.*, vol. 103, no. 17, p. 174107, Oct. 2013, doi: 10.1063/1.4826597.
- [40] O. M. Viessmann, R. J. Eckersley, K. Christensen-Jeffries, M. X. Tang, and C. Dunsby, “Acoustic super-resolution with ultrasound and microbubbles,” *Phys. Med. Biol.*, vol. 58, no. 18, pp. 6447–6458, Sep. 2013, doi: 10.1088/0031-9155/58/18/6447.
- [41] K. Christensen-Jeffries, R. J. Browning, M.-X. Tang, C. Dunsby, and R. J. Eckersley, “In vivo acoustic super-resolution and super-resolved velocity mapping using microbubbles,” *IEEE Trans. Med. Imaging*, vol. 34, no. 2, pp. 433–440, Feb. 2015, doi: 10.1109/TMI.2014.2359650.
- [42] J. Yu, L. Lavery, and K. Kim, “Super-resolution ultrasound imaging method for microvasculature in vivo with a high temporal accuracy,” *Sci. Rep.*, vol. 8, no. 1, p. 13918, 2018, doi: 10.1038/s41598-018-32235-2.
- [43] P. Song *et al.*, “Improved Super-Resolution Ultrasound Microvessel Imaging With Spatiotemporal Nonlocal Means Filtering and Bipartite Graph-Based Microbubble Tracking,” *IEEE Trans. Ultrason. Ferroelectr. Freq. Control*, vol. 65, no. 2, pp. 149–167, Feb. 2018, doi: 10.1109/TUFFC.2017.2778941.
- [44] A. Bar-zion, C. Tremblay-darveau, O. Solomon, D. Adam, and Y. C. Eldar, “Fast Vascular Ultrasound Imaging With Enhanced Spatial Resolution and Background Rejection,” *IEEE Trans. Med. Imaging*, vol. 36, no. 1, pp. 169–180, 2017.
- [45] T. Opacic *et al.*, “Motion model ultrasound localization microscopy for preclinical and clinical multiparametric tumor characterization,” *Nat. Commun.*, vol. 9, no. 1, p. 1527, Dec. 2018, doi: 10.1038/s41467-018-03973-8.
- [46] F. Lin, S. E. Shelton, D. Espindola, J. D. Rojas, G. Pinton, and P. A. Dayton, “3-D ultrasound localization microscopy for identifying microvascular morphology features of tumor angiogenesis at a resolution beyond the diffraction limit of conventional ultrasound,” *Theranostics*, vol. 7, no. 1, pp. 196–204, 2017, doi: 10.7150/thno.16899.
- [47] S. T. Hess, T. P. K. Girirajan, and M. D. Mason, “Ultra-high resolution imaging by fluorescence photoactivation localization microscopy,” *Biophys. J.*, vol. 91, no. 11, pp. 4258–4272, 2006, doi: 10.1529/biophysj.106.091116.
- [48] E. Betzig *et al.*, “Imaging intracellular fluorescent proteins at nanometer resolution,” *Science*, vol. 313, no. 5793, pp. 1642–5, Sep. 2006, doi: 10.1126/science.1127344.

- [49] M. J. Rust, M. Bates, and X. Zhuang, “Sub-diffraction-limit imaging by stochastic optical reconstruction microscopy (STORM),” *Nat. Methods*, vol. 3, no. 10, pp. 793–796, Oct. 2006, doi: 10.1038/nmeth929.
- [50] M. Tanter and M. Fink, “Ultrafast imaging in biomedical ultrasound,” *IEEE Trans. Ultrason. Ferroelectr. Freq. Control*, vol. 61, no. 1, pp. 102–119, Jan. 2014, Accessed: Sep. 12, 2018. [Online]. Available: <http://ieeexplore.ieee.org/document/6689779/>.
- [51] C. Demené *et al.*, “Spatiotemporal Clutter Filtering of Ultrafast Ultrasound Data Highly Increases Doppler and fUltrasound Sensitivity,” *IEEE Trans. Med. Imaging*, vol. 34, no. 11, pp. 2271–2285, 2015, doi: 10.1109/TMI.2015.2428634.
- [52] Y. Yang *et al.*, “Assessment of Diabetic Kidney Disease Using Ultrasound Localization Microscopy: An In Vivo Feasibility Study in Rats,” *2018 IEEE Int. Ultrason. Symp.*, no. November, pp. 1–4, Oct. 2018, doi: 10.1109/ULTSYM.2018.8579963.
- [53] J. Zhu *et al.*, “3D Super-Resolution US Imaging of Rabbit Lymph Node Vasculature in Vivo by Using Microbubbles,” *Radiology*, vol. 291, pp. 642–650, Apr. 2019, doi: 10.1148/radiol.2019182593.
- [54] T. Qiu *et al.*, “Wireless Acoustic-Surface Actuators for Miniaturized Endoscopes,” *ACS Appl. Mater. Interfaces*, vol. 9, no. 49, pp. 42536–42543, Dec. 2017, doi: 10.1021/acsami.7b12755.
- [55] A. Goldstein and B. L., “Slice-Thickness Artifacts,” *J. Clin. Ultrasound*, no. September, pp. 365–375, 1981.
- [56] M. L. Skolnick, “Estimation of ultrasound beam width in the elevation (section thickness) plane,” *Radiology*, vol. 180, no. 1, pp. 286–288, Jul. 1991, doi: 10.1148/radiology.180.1.2052713.
- [57] B. Richard, “Test Object for Measurement of Section Thickness at US,” *Radiology*, vol. 211, pp. 279–282, 1999, Accessed: Jul. 13, 2018. [Online]. Available: <https://pubs.rsna.org/doi/pdf/10.1148/radiology.211.1.r99ap04279>.
- [58] M. Peikari, T. K. Chen, A. Lasso, T. Heffter, and G. Fichtinger, “Effects of Ultrasound Section-Thickness on Brachytherapy Needle Tip Localization Error,” Springer, Berlin, Heidelberg, 2011, pp. 299–306.
- [59] N. Sharma and A. Dani, “Nonlinear estimation of gait kinematics during functional electrical stimulation and orthosis-based walking,” in *2014 American Control Conference*, Jun. 2014, pp. 4778–4783, doi: 10.1109/ACC.2014.6859342.
- [60] F. W. Liu and S. K. Cho, “3-D Micro Swimming Drone with Maneuverability,” in *Proceedings of the IEEE International Conference on Micro Electro Mechanical Systems (MEMS)*, Jan. 2019, vol. 2019-January, pp. 10–13, doi: 10.1109/MEMSYS.2019.8870890.

- [61] D. Mozaffarian *et al.*, “Executive Summary: Heart Disease and Stroke Statistics—2016 Update,” *Circulation*, vol. 133, no. 4, pp. 447–454, Jan. 2016, doi: 10.1161/CIR.0000000000000366.
- [62] M. A. O’Reilly and K. Hynynen, “A super-resolution ultrasound method for brain vascular mapping,” *Med. Phys.*, vol. 40, no. 11, 2013, doi: 10.1118/1.4823762.
- [63] B. Cox and P. Beard, “Super-resolution ultrasound,” *Nature*, vol. 527, no. 7579, pp. 451–452, Nov. 2015, doi: 10.1038/527451a.
- [64] W. H. Richardson, “Bayesian-Based Iterative Method of Image Restoration,” *J. Opt. Soc. Am.*, vol. 62, no. 1, p. 55, Jan. 1972, doi: 10.1364/josa.62.000055.
- [65] L. B. Lucy and L. B., “An iterative technique for the rectification of observed distributions,” *Astron. J.*, vol. 79, pp. 745–749, Jun. 1974, doi: 10.1086/111605.
- [66] D. S. C. Biggs and M. Andrews, “Acceleration of iterative image restoration algorithms,” *Appl. Opt.*, vol. 36, no. 8, pp. 1766–1775, Mar. 1997, doi: 10.1364/AO.36.001766.
- [67] E. A. Mukamel, H. Babcock, and X. Zhuang, “Statistical deconvolution for superresolution fluorescence microscopy,” *Biophys. J.*, vol. 102, no. 10, pp. 2391–2400, 2012, doi: 10.1016/j.bpj.2012.03.070.
- [68] G. E. R. Weller, F. S. Villanueva, A. L. Klibanov, and W. R. Wagner, “Modulating targeted adhesion of an ultrasound contrast agent to dysfunctional endothelium,” *Ann. Biomed. Eng.*, vol. 30, no. 8, pp. 1012–1019, 2002, doi: 10.1114/1.1513565.
- [69] J. Chomas, P. Dayton, D. May, and K. Ferrara, “Nondestructive subharmonic imaging,” *IEEE Trans. Ultrason. Ferroelectr. Freq. Control*, vol. 49, no. 7, pp. 883–892, Jul. 2002, doi: 10.1109/TUFFC.2002.1020158.
- [70] J. E. Leeman *et al.*, “Effect of Acoustic Conditions on Microbubble-Mediated Microvascular Sonothrombolysis,” *Ultrasound Med. Biol.*, vol. 38, no. 9, pp. 1589–1598, Sep. 2012, doi: 10.1016/j.ultrasmedbio.2012.05.020.
- [71] D. P. Basile *et al.*, “Progression after AKI: Understanding Maladaptive Repair Processes to Predict and Identify Therapeutic Treatments,” *J. Am. Soc. Nephrol.*, vol. 27, no. 3, pp. 687–697, Mar. 2016, doi: 10.1681/ASN.2015030309.
- [72] M. Heung and L. S. Chawla, “Acute Kidney Injury: Gateway to Chronic Kidney Disease,” *Nephron Clin. Pract.*, vol. 127, no. 1–4, pp. 30–34, Sep. 2014, doi: 10.1159/000363675.
- [73] K. C. W. Leung, M. Tonelli, and M. T. James, “Chronic kidney disease following acute kidney injury—risk and outcomes,” *Nat. Rev. Nephrol.*, vol. 9, no. 2, pp. 77–85, Feb. 2013, doi: 10.1038/nrneph.2012.280.

- [74] L. S. Chawla and P. L. Kimmel, “Acute kidney injury and chronic kidney disease: an integrated clinical syndrome,” *Kidney Int.*, vol. 82, no. 5, pp. 516–524, Sep. 2012, doi: 10.1038/ki.2012.208.
- [75] L. S. Chawla, R. L. Amdur, S. Amodeo, P. L. Kimmel, and C. E. Palant, “The severity of acute kidney injury predicts progression to chronic kidney disease,” *Kidney Int.*, vol. 79, no. 12, pp. 1361–1369, Jun. 2011, doi: 10.1038/ki.2011.42.
- [76] L. S. Chawla, P. W. Eggers, R. A. Star, and P. L. Kimmel, “Acute Kidney Injury and Chronic Kidney Disease as Interconnected Syndromes,” *N. Engl. J. Med.*, vol. 371, no. 1, pp. 58–66, Jul. 2014, doi: 10.1056/NEJMra1214243.
- [77] D. P. Basile, D. Donohoe, K. Roethe, and J. L. Osborn, “Renal ischemic injury results in permanent damage to peritubular capillaries and influences long-term function,” *Am. J. Physiol. Physiol.*, vol. 281, no. 5, pp. F887–F899, Nov. 2001, doi: 10.1152/ajprenal.2001.281.5.F887.
- [78] D. P. Basile and M. C. Yoder, “Renal endothelial dysfunction in acute kidney ischemia reperfusion injury,” *Cardiovasc. Hematol. Disord. Drug Targets*, vol. 14, no. 1, pp. 3–14, 2014, Accessed: Mar. 17, 2019. [Online]. Available: <http://www.ncbi.nlm.nih.gov/pubmed/25088124>.
- [79] M. Hörbelt *et al.*, “Acute and chronic microvascular alterations in a mouse model of ischemic acute kidney injury,” *Am. J. Physiol. Physiol.*, vol. 293, no. 3, pp. F688–F695, Sep. 2007, doi: 10.1152/ajprenal.00452.2006.
- [80] B. A. Molitoris, “Therapeutic translation in acute kidney injury: the epithelial/endothelial axis,” *J. Clin. Invest.*, vol. 124, no. 6, pp. 2355–63, Jun. 2014, doi: 10.1172/JCI72269.
- [81] R. Kramann, M. Tanaka, and B. D. Humphreys, “Fluorescence Microangiography for Quantitative Assessment of Peritubular Capillary Changes after AKI in Mice,” *J. Am. Soc. Nephrol.*, vol. 25, no. 9, pp. 1924–1931, Sep. 2014, doi: 10.1681/ASN.2013101121.
- [82] F. M. E. G. Steegh *et al.*, “Early Loss of Peritubular Capillaries after Kidney Transplantation,” *J. Am. Soc. Nephrol.*, vol. 22, no. 6, pp. 1024–1029, Jun. 2011, doi: 10.1681/ASN.2010050531.
- [83] A. Bohle, G. Kressel, C. A. Müller, and G. A. Müller, “The Pathogenesis of Chronic Renal Failure,” *Pathol. - Res. Pract.*, vol. 185, no. 4, pp. 421–440, Oct. 1989, doi: 10.1016/S0344-0338(89)80058-5.
- [84] K. S. Eardley *et al.*, “The role of capillary density, macrophage infiltration and interstitial scarring in the pathogenesis of human chronic kidney disease,” *Kidney Int.*, vol. 74, no. 4, pp. 495–504, Aug. 2008, doi: 10.1038/ki.2008.183.

- [85] M. Matsumoto *et al.*, “Hypoperfusion of peritubular capillaries induces chronic hypoxia before progression of tubulointerstitial injury in a progressive model of rat glomerulonephritis,” *J. Am. Soc. Nephrol.*, vol. 15, no. 6, pp. 1574–81, Jun. 2004, Accessed: Feb. 25, 2019. [Online]. Available: <http://www.ncbi.nlm.nih.gov/pubmed/15153568>.
- [86] J. R. Prowle, M. P. Molan, E. Hornsey, and R. Bellomo, “Measurement of renal blood flow by phase-contrast magnetic resonance imaging during septic acute kidney injury,” *Crit. Care Med.*, vol. 40, no. 6, pp. 1768–1776, Jun. 2012, doi: 10.1097/CCM.0b013e318246bd85.
- [87] T. Inoue *et al.*, “Noninvasive evaluation of kidney hypoxia and fibrosis using magnetic resonance imaging,” *J. Am. Soc. Nephrol.*, vol. 22, no. 8, pp. 1429–34, Aug. 2011, doi: 10.1681/ASN.2010111143.
- [88] J. Ehling *et al.*, “Quantitative Micro-Computed Tomography Imaging of Vascular Dysfunction in Progressive Kidney Diseases,” *J. Am. Soc. Nephrol.*, vol. 27, no. 2, pp. 520–532, 2016, doi: 10.1681/ASN.2015020204.
- [89] N. M. Das *et al.*, “In Vivo Quantitative Microcomputed Tomographic Analysis of Vasculature and Organs in a Normal and Diseased Mouse Model,” *PLoS One*, vol. 11, no. 2, p. e0150085, Feb. 2016, doi: 10.1371/journal.pone.0150085.
- [90] W. Cao *et al.*, “Contrast-Enhanced Ultrasound for Assessing Renal Perfusion Impairment and Predicting Acute Kidney Injury to Chronic Kidney Disease Progression,” *Antioxid. Redox Signal.*, vol. 27, no. 17, pp. 1397–1411, 2017, doi: 10.1089/ars.2017.7006.
- [91] T. D. Hull, A. Agarwal, and K. Hoyt, “New Ultrasound Techniques Promise Further Advances in AKI and CKD,” *J. Am. Soc. Nephrol.*, vol. 28, no. 12, pp. 3452–3460, Dec. 2017, doi: 10.1681/ASN.2017060647.
- [92] S. Faubel, N. U. Patel, M. E. Lockhart, and M. A. Cadnapaphornchai, “Renal relevant radiology: use of ultrasonography in patients with AKI,” *Clin. J. Am. Soc. Nephrol.*, vol. 9, no. 2, pp. 382–94, Feb. 2014, doi: 10.2215/CJN.04840513.
- [93] N. Schieda *et al.*, “Gadolinium-Based Contrast Agents in Kidney Disease: A Comprehensive Review and Clinical Practice Guideline Issued by the Canadian Association of Radiologists,” *Can. J. Kidney Heal. Dis.*, vol. 5, pp. 1–17, Jan. 2018, doi: 10.1177/2054358118778573.
- [94] M. Andreucci, T. Faga, A. Pisani, M. Sabbatini, and A. Michael, “Acute kidney injury by radiographic contrast media: Pathogenesis and prevention,” *BioMed Research International*. Hindawi, pp. 1–21, Aug. 2014, doi: 10.1155/2014/362725.
- [95] P. Susantitaphong and S. Eiam-Ong, “Nonpharmacological Strategies to Prevent Contrast-Induced Acute Kidney Injury,” *Biomed Res. Int.*, pp. 1–12, 2014, doi: 10.1155/2014/463608.

- [96] I. M. Braverman and S. Cowper, “Nephrogenic systemic fibrosis,” *F1000 Med. Rep.*, vol. 2, no. 84, p. 84, Nov. 2010, doi: 10.3410/M2-84.
- [97] S. D. Weisbord and D. du Cheryon, “Contrast-associated acute kidney injury is a myth: No,” *Intensive Care Med.*, vol. 44, no. 1, pp. 107–109, Jan. 2018, doi: 10.1007/s00134-017-5015-6.
- [98] C. Huang *et al.*, “Short Acquisition Time Super-Resolution Ultrasound Microvessel Imaging via Microbubble Separation,” *Sci. Rep.*, vol. 10, no. 1, pp. 1–13, Dec. 2020, doi: 10.1038/s41598-020-62898-9.
- [99] J. Foiret, H. Zhang, T. Ilovitsh, L. Mahakian, S. Tam, and K. W. Ferrara, “Ultrasound localization microscopy to image and assess microvasculature in a rat kidney,” *Sci. Rep.*, vol. 7, no. 1, p. 13662, Dec. 2017, doi: 10.1038/s41598-017-13676-7.
- [100] S. Tang *et al.*, “Kalman Filter-Based Microbubble Tracking for Robust Super-Resolution Ultrasound Microvessel Imaging,” *IEEE Trans. Ultrason. Ferroelectr. Freq. Control*, vol. 67, no. 9, pp. 1738–1751, Sep. 2020, doi: 10.1109/TUFFC.2020.2984384.
- [101] S. B. Andersen *et al.*, “Super-Resolution Ultrasound Imaging of Rat Kidneys before and after Ischemia-Reperfusion,” in *IEEE International Ultrasonics Symposium, IUS*, Oct. 2019, vol. 2019-October, pp. 1169–1172, doi: 10.1109/ULTSYM.2019.8926190.
- [102] F. Lin, J. D. Rojas, and P. A. Dayton, “Super resolution contrast ultrasound imaging: Analysis of imaging resolution and application to imaging tumor angiogenesis,” in *IEEE International Ultrasonics Symposium, IUS*, Nov. 2016, vol. 2016-Novem, doi: 10.1109/ULTSYM.2016.7728735.
- [103] F. Lin, J. K. Tsuruta, J. D. Rojas, and P. A. Dayton, “Optimizing Sensitivity of Ultrasound Contrast-Enhanced Super-Resolution Imaging by Tailoring Size Distribution of Microbubble Contrast Agent,” *Ultrasound Med. Biol.*, vol. 43, no. 10, pp. 2488–2493, Oct. 2017, doi: 10.1016/j.ultrasmedbio.2017.05.014.
- [104] J. A. Jakobsen, R. Oyen, H. S. Thomsen, and S. K. Morcos, “Safety of ultrasound contrast agents,” *Eur. Radiol.*, vol. 15, no. 5, pp. 941–945, May 2005, doi: 10.1007/s00330-004-2601-0.
- [105] G. Haar, “Safety and bio-effects of ultrasound contrast agents,” *Med. Biol. Eng. Comput.*, vol. 47, no. 8, pp. 893–900, Aug. 2009, doi: 10.1007/s11517-009-0507-3.
- [106] P. R. Muskula and M. L. Main, “Safety With Echocardiographic Contrast Agents,” *Circ. Cardiovasc. Imaging*, vol. 10, p. e005459, Apr. 2017, doi: 10.1161/CIRCIMAGING.116.005459.
- [107] K. Wei *et al.*, “The Safety of Definity and Optison for Ultrasound Image Enhancement: A Retrospective Analysis of 78,383 Administered Contrast Doses,” *J. Am. Soc. Echocardiogr.*, vol. 21, no. 11, pp. 1202–1206, 2008, doi: 10.1016/j.echo.2008.07.019.

- [108] N. I. Skrypnyk, R. C. Harris, and M. P. de Caestecker, "Ischemia-reperfusion model of acute kidney injury and post injury fibrosis in mice," *J. Vis. Exp.*, vol. 78, p. 50495, Aug. 2013, doi: 10.3791/50495.
- [109] H. M. Jong, L. G. Chen, and T. D. Chiueh, "Parallel Architectures for 3-Step Hierarchical Search Block-Matching Algorithm," *IEEE Trans. Circuits Syst. Video Technol.*, vol. 4, no. 4, pp. 407–416, 1994, doi: 10.1109/76.313135.
- [110] R. Srinivasan and K. R. Rao, "Predictive Coding Based on Efficient Motion Estimation," *IEEE Trans. Commun.*, vol. 33, no. 8, pp. 888–896, 1985, doi: 10.1109/TCOM.1985.1096398.
- [111] T. C. Lee, R. L. Kashyap, and C. N. Chu, "Building Skeleton Models via 3-D Medial Surface Axis Thinning Algorithms," *CVGIP Graph. Model. Image Process.*, vol. 56, no. 6, pp. 462–478, Nov. 1994, doi: 10.1006/cgip.1994.1042.
- [112] I. Arganda-Carreras, R. Fernández-González, A. Muñoz-Barrutia, and C. Ortiz-De-Solorzano, "3D reconstruction of histological sections: Application to mammary gland tissue," *Microsc. Res. Tech.*, vol. 73, no. 11, pp. 1019–1029, Oct. 2010, doi: 10.1002/jemt.20829.
- [113] G. Polder, H. L. E. Hovens, and A. J. Zweers, "Measuring shoot length of submerged aquatic plants using graph analysis," in *Proceedings of the ImageJ User and Developer Conference 2010, Mondorf-les-Bains*, 2010, pp. 27–29.
- [114] D. P. Basile, K. Friedrich, B. Chelladurai, E. C. Leonard, and A. R. Parrish, "Renal ischemia reperfusion inhibits VEGF expression and induces ADAMTS-1, a novel VEGF inhibitor," *Am. J. Physiol. Physiol.*, vol. 294, no. 4, pp. F928–F936, Apr. 2008, doi: 10.1152/ajprenal.00596.2007.
- [115] E. C. Leonard, J. L. Friedrich, and D. P. Basile, "VEGF-121 preserves renal microvessel structure and ameliorates secondary renal disease following acute kidney injury," *Am. J. Physiol. Physiol.*, vol. 295, no. 6, pp. F1648–F1657, Dec. 2008, doi: 10.1152/ajprenal.00099.2008.
- [116] J. Ehling, T. Lammers, and F. Kiessling, "Non-invasive imaging for studying anti-angiogenic therapy effects," *Thromb. Haemost.*, vol. 109, no. 03, pp. 375–390, Nov. 2013, doi: 10.1160/TH12-10-0721.
- [117] S. Tanaka, T. Tanaka, and M. Nangaku, "Hypoxia and Dysregulated Angiogenesis in Kidney Disease.," *Kidney Dis. (Basel, Switzerland)*, vol. 1, no. 1, pp. 80–9, May 2015, doi: 10.1159/000381515.
- [118] J. H. Wible, K. P. Galen, J. K. Wojdyla, M. S. Hughes, A. L. Klibanov, and G. H. Brandenburger, "Microbubbles induce renal hemorrhage when exposed to diagnostic ultrasound in anesthetized rats," *Ultrasound Med. Biol.*, vol. 28, no. 11–12, pp. 1535–1546, 2002, doi: 10.1016/S0301-5629(02)00651-8.

- [119] D. L. Miller, C. Dou, and R. C. Wiggins, "Contrast-enhanced diagnostic ultrasound causes renal tissue damage in a porcine model," *J. Ultrasound Med.*, vol. 29, no. 10, pp. 1391–1401, Oct. 2010, doi: 10.7863/jum.2010.29.10.1391.
- [120] K. Matsushita *et al.*, "Comparison of risk prediction using the CKD-EPI equation and the MDRD study equation for estimated glomerular filtration rate," *JAMA - J. Am. Med. Assoc.*, vol. 307, no. 18, pp. 1941–1951, May 2012, doi: 10.1001/jama.2012.3954.
- [121] T. Fischer *et al.*, "The use of contrast-enhanced US in renal transplant: First results and potential clinical benefit," *Eur. Radiol. Suppl.*, vol. 15, no. 5, Dec. 2005, doi: 10.1007/s10406-005-0173-y.
- [122] K. Mueller-Peltzer, G. Negrão De Figueiredo, M. Fischereder, A. Habicht, J. Rübenthaler, and D. A. Clevert, "Vascular rejection in renal transplant: Diagnostic value of contrast-enhanced ultrasound (CEUS) compared to biopsy," *Clin. Hemorheol. Microcirc.*, vol. 69, no. 1–2, pp. 77–82, 2018, doi: 10.3233/CH-189115.
- [123] M. O'Donnell, "Coded excitation system for improving the penetration of real-time phased-array imaging systems," *IEEE Trans. Ultrason. Ferroelectr. Freq. Control*, vol. 39, no. 3, pp. 341–351, May 1992, doi: 10.1109/58.143168.
- [124] A. Nowicki, W. Secomski, I. Trots, and J. Litniewski, "Extending penetration depth using coded ultrasonography," *Bull. POLISH Acad. Sci.*, vol. 52, no. 3, pp. 215–220, 2004.
- [125] S. I. B. Principles, J. Shen, S. Member, and E. S. Ebbini, "A New Coded-Excitation Ultrasound Imaging," *Ultrason. Ferroelectr. Freq. Control IEEE Trans.*, vol. 43, no. 1, pp. 131–140, 1996.
- [126] R. Y. Chiao and Xiaohui Hao, "Coded excitation for diagnostic ultrasound: a system developer's perspective," *IEEE Trans. Ultrason. Ferroelectr. Freq. Control*, vol. 52, no. 2, pp. 160–170, Feb. 2005, doi: 10.1109/TUFFC.2005.1406543.
- [127] K. D. Kochanek, S. L. Murphy, J. Xu, and B. Tejada-Vera, "Deaths: Final Data for 2014," *Natl. Vital Stat. Reports*, vol. 65, no. 4, Jun. 2016.
- [128] E. Wilkins *et al.*, "European Cardiovascular Disease Statistics 2017," *Eur. Hear. Network, Brussels*, Feb. 2017, Accessed: Jan. 31, 2019. [Online]. Available: <https://www.herc.ox.ac.uk/publications/european-cardiovascular-disease-statistics-2017>.
- [129] F. G. Fowkes, E. Housley, E. H. Cawood, C. C. Macintyre, C. V Ruckley, and R. J. Prescott, "Edinburgh Artery Study: prevalence of asymptomatic and symptomatic peripheral arterial disease in the general population," *Int. J. Epidemiol.*, vol. 20, no. 2, pp. 384–92, Jun. 1991, Accessed: Jan. 31, 2019. [Online]. Available: <http://www.ncbi.nlm.nih.gov/pubmed/1917239>.

- [130] V. Fuster, Z. A. Fayad, P. R. Moreno, M. Poon, R. Corti, and J. J. Badimon, “Atherothrombosis and High-Risk Plaque: Part II: Approaches by Noninvasive Computed Tomographic/Magnetic Resonance Imaging,” *J. Am. Coll. Cardiol.*, vol. 46, no. 7, pp. 1209–1218, 2005, doi: 10.1016/j.jacc.2005.03.075.
- [131] P. R. Moreno *et al.*, “Plaque Neovascularization Is Increased in Ruptured Atherosclerotic Lesions of Human Aorta,” *Circulation*, vol. 110, no. 14, 2004.
- [132] M. Naghavi *et al.*, “From Vulnerable Plaque to Vulnerable Patient,” *Circulation*, vol. 108, no. 15, pp. 1772–1778, Oct. 2003, doi: 10.1161/01.CIR.0000087481.55887.C9.
- [133] F. D. Kolodgie *et al.*, “Intraplaque hemorrhage and progression of coronary atheroma,” *N. Engl. J. Med.*, vol. 349, no. 24, pp. 2316–25, Dec. 2003, doi: 10.1056/NEJMoa035655.
- [134] R. Virmani *et al.*, “Atherosclerotic Plaque Progression and Vulnerability to Rupture,” *Arterioscler. Thromb. Vasc. Biol.*, vol. 25, no. 10, pp. 2054–2061, Oct. 2005, doi: 10.1161/01.ATV.0000178991.71605.18.
- [135] M. Gössl *et al.*, “Segmental heterogeneity of vasa vasorum neovascularization in human coronary atherosclerosis,” *JACC. Cardiovasc. Imaging*, vol. 3, no. 1, pp. 32–40, Jan. 2010, doi: 10.1016/j.jcmg.2009.10.009.
- [136] E. L. Ritman and A. Lerman, “The Dynamic Vasa Vasorum,” *Cardiovasc. Res.*, vol. 75, no. 4, pp. 649–658, Sep. 2007, doi: 10.1016/j.cardiores.2007.06.020.
- [137] J. Xu, X. Lu, and G.-P. Shi, “Vasa vasorum in atherosclerosis and clinical significance,” *Int. J. Mol. Sci.*, vol. 16, no. 5, pp. 11574–608, May 2015, doi: 10.3390/ijms160511574.
- [138] M. Magnoni, E. Ammirati, and P. G. Camici, “Non-invasive molecular imaging of vulnerable atherosclerotic plaques,” *J. Cardiol.*, vol. 65, no. 4, pp. 261–9, Apr. 2015, doi: 10.1016/j.jjcc.2015.01.004.
- [139] A. Taruya *et al.*, “Vasa Vasorum Restructuring in Human Atherosclerotic Plaque Vulnerability,” *J. Am. Coll. Cardiol.*, vol. 65, no. 23, pp. 2469–2477, Jun. 2015, doi: 10.1016/j.jacc.2015.04.020.
- [140] T.-G. Kwon, L. O. Lerman, and A. Lerman, “The Vasa Vasorum in Atherosclerosis,” *J. Am. Coll. Cardiol.*, vol. 65, no. 23, 2015.
- [141] P. M. Winter *et al.*, “Molecular Imaging of Angiogenesis in Early-Stage Atherosclerosis With  $\alpha_v\beta_3$ -Integrin-Targeted Nanoparticles,” *Circulation*, vol. 108, no. 18, pp. 2270–2274, Nov. 2003, doi: 10.1161/01.CIR.0000093185.16083.95.
- [142] K. Cai *et al.*, “MR molecular imaging of aortic angiogenesis,” *JACC. Cardiovasc. Imaging*, vol. 3, no. 8, pp. 824–32, Aug. 2010, doi: 10.1016/j.jcmg.2010.03.012.

- [143] W. Kerwin *et al.*, “Quantitative Magnetic Resonance Imaging Analysis of Neovasculture Volume in Carotid Atherosclerotic Plaque,” *Circulation*, vol. 107, no. 6, pp. 851–856, Feb. 2003, doi: 10.1161/01.CIR.0000048145.52309.31.
- [144] F. Hyafil *et al.*, “Noninvasive detection of macrophages using a nanoparticulate contrast agent for computed tomography,” *Nat. Med.*, vol. 13, no. 5, pp. 636–641, May 2007, doi: 10.1038/nm1571.
- [145] M. M. Sadeghi, D. K. Glover, G. M. Lanza, Z. A. Fayad, and L. L. Johnson, “Imaging Atherosclerosis and Vulnerable Plaque,” *J. Nucl. Med.*, vol. 51, no. Supplement\_1, pp. 51S-65S, May 2010, doi: 10.2967/jnumed.109.068163.
- [146] T. Kubo *et al.*, “Assessment of Culprit Lesion Morphology in Acute Myocardial Infarction,” *J. Am. Coll. Cardiol.*, vol. 50, no. 10, pp. 933–939, Sep. 2007, doi: 10.1016/j.jacc.2007.04.082.
- [147] I.-K. Jang *et al.*, “In Vivo Characterization of Coronary Atherosclerotic Plaque by Use of Optical Coherence Tomography,” *Circulation*, vol. 111, no. 12, pp. 1551–1555, Mar. 2005, doi: 10.1161/01.CIR.0000159354.43778.69.
- [148] D. Maresca *et al.*, “Contrast-enhanced intravascular ultrasound pulse sequences for bandwidth-limited transducers,” *Ultrasound Med. Biol.*, vol. 39, no. 4, pp. 706–13, Apr. 2013, doi: 10.1016/j.ultrasmedbio.2012.10.020.
- [149] K. H. Martin, B. D. Lindsey, J. Ma, T. C. Nichols, X. Jiang, and P. A. Dayton, “Ex Vivo Porcine Arterial and Chorioallantoic Membrane Acoustic Angiography Using Dual-Frequency Intravascular Ultrasound Probes,” *Ultrasound Med. Biol.*, vol. 42, no. 9, pp. 2294–307, 2016, doi: 10.1016/j.ultrasmedbio.2016.04.008.
- [150] H. Shekhar, J. S. Rowan, and M. M. Doyley, “Combining Subharmonic and Ultraharmonic Modes for Intravascular Ultrasound Imaging: A Preliminary Evaluation,” *Ultrasound Med. Biol.*, vol. 43, no. 11, pp. 2725–2732, 2017, doi: 10.1016/j.ultrasmedbio.2017.07.012.
- [151] D. Maresca *et al.*, “Imaging microvasculature with contrast-enhanced ultraharmonic ultrasound,” *Ultrasound Med. Biol.*, vol. 40, no. 6, pp. 1318–28, Jun. 2014, doi: 10.1016/j.ultrasmedbio.2013.12.029.
- [152] D. Staub *et al.*, “Contrast-enhanced ultrasound imaging of the vasa vasorum: from early atherosclerosis to the identification of unstable plaques,” *JACC. Cardiovasc. Imaging*, vol. 3, no. 7, pp. 761–71, Jul. 2010, doi: 10.1016/j.jcmg.2010.02.007.
- [153] D. Moguillansky *et al.*, “Quantification of plaque neovascularization using contrast ultrasound: A histologic validation,” *Eur. Heart J.*, vol. 32, no. 5, pp. 646–653, Mar. 2011, doi: 10.1093/eurheartj/ehq197.
- [154] M. Magnoni *et al.*, “Contrast-enhanced ultrasound imaging of periadventitial vasa vasorum in human carotid arteries,” *Eur. J. Echocardiogr.*, vol. 10, no. 2, pp. 260–264, Aug. 2008, doi: 10.1093/ejehocardiogr/jen221.

- [155] S. Harput *et al.*, “Two-Stage Motion Correction for Super-Resolution Ultrasound Imaging in Human Lower Limb,” *IEEE Trans. Ultrason. Ferroelectr. Freq. Control*, vol. 65, no. 5, pp. 803–814, May 2018, doi: 10.1109/TUFFC.2018.2824846.
- [156] M. Kim, Y. Zhu, J. Hedhli, L. W. Dobrucki, and M. F. Insana, “Multidimensional Clutter Filter Optimization for Ultrasonic Perfusion Imaging,” *IEEE Trans. Ultrason. Ferroelectr. Freq. Control*, vol. 65, no. 11, pp. 2020–2029, Nov. 2018, doi: 10.1109/TUFFC.2018.2868441.
- [157] O. Galili, J. Herrmann, J. Woodrum, K. J. Sattler, L. O. Lerman, and A. Lerman, “Adventitial vasa vasorum heterogeneity among different vascular beds,” *J. Vasc. Surg.*, vol. 40, no. 3, pp. 529–535, 2004, doi: 10.1016/j.jvs.2004.06.032.